# A multidisciplinary approach to unravel the steam-driven eruptions in volcanic systems

**Cristian Montanaro**


München 2016

# A multidisciplinary approach to unravel the steam-driven eruptions in volcanic systems

**Cristian Montanaro**

Dissertation zur Erlangung des Doktorgrades
an der Fakultät für Geowissenschaften
der Ludwig-Maximilians-Universität
München

vorgelegt von
Cristian Montanaro
aus Isernia (Italien)

München, den 7. Juli 2016

Erstgutachter: Dr. PD Bettina Scheu
Zweitgutachter: Prof. Dr. Donald B. Dingwell
Tag der mündlichen Prüfung: 07.07.2016

***Κατά τον δαίμονα εαυτού***
*True to his own spirit…*

*If the doors of perception were*
*cleansed, everything would*
*appear to man as it is,*
***infinite****…*

# *Abstract*

*Steam-driven eruptions*, such as phreatic and hydrothermal, represent a large percentage of explosive events, perhaps the majority, in volcanic systems. These eruptions do expel only fragments of non-juvenile rocks disintegrated by the expansion of water as liquid or gas phase. The conditions that cause steam-driven eruptions arise through a rapid increase in temperature or decrease in pressure. Thus, these eruptions may occur with different degrees of explosivity, as their violence is related to the magnitude of the decompression work that can be performed by fluids expansion. Steam-driven eruption deposits, though generally hardly recognized or badly preserved, yield information on the dynamics and energy of these explosive events.

This dissertation presents the results from a multidisciplinary study of two recent eruptive events, and a further experimental study. In particular these studies investigate the role played by i) the pressure, temperature and liquid fraction within a system before an eruption, and ii) the nature of the rock hosting the hydrothermal system. These parameters control the rate at which energy is released and in turns the violence of such explosive events.

The findings of this study suggest that the pore liquid fraction and its physical conditions (pressure-temperature) control the stored explosive energy: an increasing liquid fraction within the pore space increases the explosive energy. Overall, the energy released by steam-flashing can be estimated to be one order of magnitude higher than for the solely (Argon) gas or steam expansion. Additionally the decompression of liquids at an initial pressure and temperature close to their boiling-point may result in a higher production of fine material already under partial saturation conditions.

The lithologies investigated in this work (from loose sediments, to very heterogeneous tuff breccias and agglutinates, and fine-grained tuffs) cover a large spectra of porosity, permeability and rock strength. These parameters control the energy storage, as well as its partitioning in form of fragmentation and particle ejection. Flashing of water in loose saturated sediments can produce violent explosion already for small decompression events (e.g. lake drainage). Consequently craters of tens-of-meter size can be generated and debris launched at significant distance (>100m). Interbedded low permeable and clay-rich levels may account for the over-pressurization and failure of the system, while the loose material can allow an efficient conversion of the explosive energy in other forms. In case of consolidated rock the connected porosity relates to the amount of stored energy, with higher porosities accounting for higher energies. The energy surplus in the presence of steam-flashing leads to a faster fragmentation with respect to a gas-driven process. As result higher ejection velocity may be reached by the fragmented particles. Low permeable rock's, which allows not to dissipate pressure during the fragmentation process, assures a maximum result in terms of produced fine. Additionally, at constant porosity weaker rocks generated more fine particles than firmly cemented rocks. The fragmentation of very heterogeneous rocks, including low porous clasts, can create both large amount of very fine material, together with larger fragments (in analogy to ballistics formation). Destabilization of hydrothermal system with pressurized fluids hosted in such a heterogeneous lithology, may produce extended ash plumes and (dilute) pyroclastic density currents as well as widespread ballistic events.

The multidisciplinary approach (field, laboratory, theoretical, and seismic studies) as tool to unravel the energetics of steam-driven eruptions provided many estimates on parameters controlling their explosivity. These finding should be considered for both modeling and evaluation of the associated hazard of steam-driven eruptions.

# *Kurzfassung*

Wasserdampf-getriebene Eruptionen, wie phreatische und hydrothermale Ausbrüche, stellen einen Großteil, wenn nicht sogar die Mehrheit vulkanischer Ausbrüche dar. Diese Eruptionen fördern kein frisches Magma sondern alle möglichen Formen nicht-juvenilen Gesteines, zerborsten aufgrund der schlagartigen Ausdehnung von Wasser, in flüssiger oder gasförmiger Form. Ausgelöst werden diese Ausbrüche durch entweder einen Anstieg der Temperatur oder durch einen Druckabfall im Untergrund. Die Stärke solcher Ausbrüche hängt von der Dekompressionsarbeit der sich ausdehnenden Fluide ab; die Explosivität variiert dementsprechend. Ablagerungen phreatischer Ausbrüche ermöglichen es Aussagen über die Dynamik und Energie dieser Ablagerungen zu treffen, leider sind solche Ablagerungen oft nur sehr schlecht erhalten und zudem sehr schwer zu identifizieren.

In der vorliegenden Dissertation werden die Ergebnisse zweier multidisziplinärer Studien rezenter wasserdampf-getriebener Eruptionen vorgestellt, sowie die Ergebnisse einer weiteren experimentellen Studie. Im Besonderen werden dabei i) der Flüssigkeitsanteil der Fluide sowie deren Druck und Temperatur vor einem Ausbruch und ii) die Gesteinseigenschaften des hydrothermalen Reservoirs untersucht. Diese Parameter bestimmen, wie schnell Energie freigesetzt wird, und kontrollieren somit die Stärke der explosiven Ereignisse.

Diese Studie zeigt auf, wie der Flüssigkeitsanteil im Porenraum und deren Druck und Temperatur die gespeicherte Energie beeinflussen, die in der Explosion freigesetzt werden kann. Generell gilt: Je höher der Flüssigkeitsanteil, desto höher die Explosionsenergie. Die Energie, welche beim explosionsartigem Verdampfen von überhitztem Wasser freigesetzt wird, ist in etwa eine Größenordnung höher als die Energie durch die Ausdehnung von Argon, Gas oder Dampf. Außerdem erzeugt das schlagartige Verdampfen von Flüssigkeiten in der Nähe des Siedepunktes (aufgrund der Temperatur- und Druckbedingungen) einen höheren Anteil an Feinmaterial. Dieser Effekt tritt bereits bei Teilsättigung des Porenraumes auf.

Die Gesteine (von losem Sediment bis hin zu stark unterschiedlichen Tuff-Breckzien, „Agglutinationen“ und feinkörnigen Tuffen), welche im Rahmen dieser Studie untersucht wurden, zeigen eine große Bandbreite an Porosität, Permeabilität und Festigkeit. Diese Eigenschaften bestimmen die Höhe der gespeicherten Energie, die sich während der Dekomprimierung in Fragmentierungs- und Auswurfsenergie aufteilt. Explosionsartiges Verdampfen von Wasser in losem Sediment kann selbst bei kleinen Dekompressionsereignissen (wie dem plötzlichem Entwässern von Seen) zu heftigen Ausbrüchen führen. Dabei können Krater mit mehreren Zehnermetern Durchmesser entstehen und Gesteinstrümmer über 100 m weit ausgeworfen werden. Zwischengelagerte geringdurchlässige tonreiche Sedimentschichten können zu einem Überdruck im Untergrund führen, welcher sich in einem Ausbruch entlädt. Loses Material hingegen ermöglicht eine effiziente Umwandlung der Energie in kinetische Energie. Bei Festgestein bestimmt die Porosität die Höhe der gespeicherten Energie. Höhere Porosität resultiert in höherer gespeicherter Energie. Der Energieüberschuss beim schlagartigem Verdampfen von überhitzten Wasser führt zu einer schnelleren Fragmentierung im Vergleich zu Ausbrüchen, die von Gasausdehnung getrieben sind. Damit werden höhere Auswurfgeschwindigkeiten der Partikel erreicht. Gering durchlässige Gesteine, die während der Fragmentierung keinen Druck ableiten können, erzeugen dadurch einen höheren Anteil an Feinmaterial. Zusätzlich erzeugen schwächere Gesteine bei gleicher Porosität mehr Feinmaterial als feste Gesteine. Die Fragmentierung von sehr stark heterogenen Gesteinen mit niedrigporösen Klasten kann sowohl zu einem hohen Feinanteil,

als auch zur Bildung größerer Bruchstücke führen (analog zu der Bildung von Ballistika). Wenn ein hydrothermales System mit unter Druck stehenden Fluiden in solch einem heterogenen Medium soweit destabilisiert wird, dass es zu einem Ausbruch kommt, kann dies zu mächtigen Aschesäulen, verdünnten pyroklastischen Dichteströmen (nuées ardentes), sowie ausgedehnten ballistischen Auswürfen führen.

Der multidisziplinäre Ansatz (Geländearbeit, Laboruntersuchung, theoretische und seismische Studien) diente dazu, die Energetik phreatischer Ausbrüche aufzudecken, und ermöglichte eine Abschätzung der Parameter, die deren Explosivität kontrollieren. Die Erkenntnisse dieser Studie sollten sowohl für Modellierungen, als auch für Gefährdungsabschätzungen phreatischer Ausbrüche berücksichtigt werden.

.

# *Preamble*

Most of the content of this doctoral dissertation has been published in scientific journals, is in the state of a submitted manuscript in review, or in preparation for submission to a scientific journal. Detailed references are listed below. Modifications have only slightly been made, mainly in terms of formatting and style for incorporation into a consistent overall thesis design.

*Montanaro, C., Scheu, B., Gudmundsson, M.T., Vogfjörd, K., Reynolds, H.I., Dürig, T., Strehlow, K., Rott, S., Reuschlé, T., Dingwell, D.B., 2016. Multidisciplinary constraints of hydrothermal explosions based on the 2013 Gengissig lake events, Kverkfjöll volcano, Iceland. Earth Planet. Sci. Lett. 434, 308–319. doi:10.1016/j.epsl.2015.11.043*

*Montanaro, C., Scheu, B., Cronin S.J., Breard, E.C.P., Lube, G., Dingwell, D.B., Experimental estimates of the energy budget of hydrothermal eruptions; application to 2012 Upper Te Maari eruption, New Zealand. Earth and Planetary Science Letters (Submitted)*

*Montanaro, C., Scheu, B., Mayer, K., Orsi, G. Moretti, R., Isaia, R., Dingwell, D.B., Experimental investigation of the explosivity of steam-driven eruptions: case study from Solfatara volcano, Campi Flegrei. Journal of Volcanology and Geothermal Research (manuscript in preparation).*

# *Acknowledgements*

**Thanks to…**

*my family, which supported me from a far distance, but which I always keep close in my heart…*

*my friends, the old and the new, the good, the bad and the ugly… to Gabriele, Antonio, Antonino which are always been pillars in my life…to my long-time volcano-buddy Antonio…no matter what we gonna cross our path forever… to my crazy frenchy friend Oryaelle, and my German instructor of "life" aka Scheiße Klausi, to my beloved Veronica and Giulio (and to the night spent in the Excess!)...To Gigio and Ale (and the great moments spent at the Harlekin)…to Jenny who always bring around her happiness!..*

*to the man who contain multitudes … the unique Danilo!*

*to Rike… may our friendship endure as long as our lives..*

*to Eleonora, who brought colors and joy in my life and always will…*

*to Betty.. thanks for all the lessons in life and work, the patience and the trust you gave me!*

*to all my beloved NEMOH family… thanks for their friendship, madness and "proactivity"*

*thanks to all the LMU people with which I shared part of my great experience here in Muenchen…*

*and also to many people which I am probably forgetting in this moment…you'll probably be there in the final version of this thesis! :)*

*not to be forget.. thanks to the Corleone.. to Gun's and Roses… to the Queen and the Doors.. to Daddy, to Lola and the Registratur…to the Netzer and the Isar…to the Longbow and the Lebowsky…to the Rennbahn and the white Russian….to the Tongariro… to San Francisco and Queenstown…to Kverkfjöll and Solfatara… to the Lord of the Rings…to Freddie Mercury…and Jim Morrison…*

*a special thanks to Manuela…who sailed together with me in seas of love, passion, friendship and more…you always been my guide, my friend … for you have been, and always will be a safe haven where to shelter from the storm…*

# *Table of Contents*


Abstract ..... ii
Zusammenfassung ..... iii
Preamble ..... v
Acknowledgements ..... vi
Table of Contents ..... vii
List of Figures ..... ix
List of Tables ..... x
List of Equations ..... xi
Chapter 1 Introduction ..... 1
1.1 Steam-driven eruptions in volcanic systems ..... 1
1.2 Scope and objectives ..... 5
1.3 Overview of dissertation ..... 6
Chapter 2 Explosivity of steam-driven eruptions ..... 9
2.1 Introduction ..... 9
2.2 Factors controlling the explosivity of steam-driven eruptions ..... 9
2.3 Previous methods and models used ..... 10
2.4 Explosivity of water in hydrothermal system: theoretical background ..... 11
2.5 Experimental investigation of steam-driven eruptions ..... 14
Chapter 3 Multidisciplinary constraints of hydrothermal explosions ..... 19
3.1 Introduction ..... 19
3.2 Geological setting of Gengissig lake ..... 19
3.3 August 16th hydrothermal explosions ..... 20
3.4 Field-based studies ..... 21
3.4.1 Sedimentary succession-hydrothermal explosions deposits-crater features ..... 22
3.4.2 Grain-size distribution and particle shape characterization ..... 26
3.4.3 Deposit volume and mass ..... 28
3.5 Seismic studies ..... 28
3.6 Laboratory studies ..... 30
3.6.1 Permeability measurements ..... 31
3.6.2 Decompression experiments ..... 32
3.6.2.1 Methods ..... 32
*3.6.2.2* Results ..... 33
3.7 Energy considerations ..... 35
3.8 Discussion ..... 37
3.8.1 Explosion mechanism and dynamic ..... 37
3.8.2 Energy budget and partitioning ..... 40
3.8.3 Broader implications ..... 40
3.9 Conclusions ..... 41
Chapter 4 Experimental estimates of the energy budget of hydrothermal eruptions ..... 43
4.1 Introduction ..... 43
4.1.1 The 6th August 2012 Upper Te Maari crater eruption ..... 44
4.1.2 Upper Te Maari hydrothermal system ..... 45
4.2 Field-based studies ..... 46

4.3 Laboratory studies ..... 47
4.3.1 Material investigated ..... 47
4.3.2 Decompression experiments ..... 48
4.3.2.1 Methods ..... 48
4.3.3 Results ..... 49
4.3.3.1 Grain-size distribution ..... 49
4.3.3.2 Ejection velocities ..... 50
4.4 Energetic considerations ..... 52
4.4.1 Theoretical background ..... 52
4.4.2 Explosive energy during decompression experiments ..... 52
4.5 Discussion ..... 55
4.5.1 Pressure-temperature effect: steam-flashing versus steam expansion ..... 55
4.5.2 Porosity and rock texture effects ..... 56
4.5.3 Ejection behavior of heterogeneous breccias ..... 56
4.5.4 Energy partitioning ..... 58
4.5.5 Eruption dynamics of the westward directed plume ..... 59
4.6 Conclusions ..... 62
Chapter 5 Experimental investigation of the explosivity of steam-driven eruptions ..... 65
5.1 Introduction ..... 65
5.2 Explosivity of water in hydrothermal system ..... 66
5.3 Geological setting of the case study: Solfatara and Pisciarelli ..... 66
5.3.1 Material investigated ..... 68
5.4 Experimental studies ..... 69
5.4.1 Methods ..... 69
5.4.1.1 Petrophysical characterization ..... 69
5.4.1.2 Decompression experiments ..... 70
5.5 Results ..... 72
5.5.1 Petrophysical properties ..... 72
5.5.2 Fragmentation threshold ..... 74
5.5.3 Explosive energy at experimental conditions ..... 74
5.5.4 Grain size distribution ..... 75
5.5.5 Fragmentation speed ..... 78
5.5.6 Ejection velocities ..... 78
5.6 Discussion ..... 80
5.6.1 Effect of liquid fraction ..... 81
5.6.2 Effect of rock porosity and permeability ..... 81
5.6.3 Fragmentation behavior ..... 82
5.6.4 Fragmentation speed and ejection behavior ..... 82
5.7 Conclusions ..... 83
Chapter 6 Conclusions and outlook ..... 85
Outlook ..... 88
References ..... 91

# *List of Figures*

Figure 1.1 Example of phreatic eruption at Poas Volcano and at White Island. 2
Figure 1.2 Schematic model of steam-driven eruptions within volcanic systems. 2
Figure 1.3 Eruption at Mount Ontake (video source BBC News). 3
Figure 1.4 Eruption of Upper Te Maari crater (video source TMT News). 4
Figure 1.5 Aerial photo of Gengissig ice dammed on the 16th of August 2013 4
Figure 2.1 The mass liquid fraction produced by the depressurization of a saturated liquid 13
Figure 2.2 Mechanical work released by the irreversible expansion of steam. 13
Figure 2.3 P-H diagram showing the energy source for for different volcanic environments. 14
Figure 2.4 Fragmentation bomb setup 15
Figure 3.1 Hydrothermal explosions at Gengissig lake (Kverkfjöll caldera). 21
Figure 3.2 Stratigraphic sequence at crater 2 22
Figure 3.3 Stratigraphic sequence at crater 2 and grain size distribution at different levels 23
Figure 3.4 Stratigraphic sequence at crater 3 and grain size distribution at different levels. 24
Figure 3.5 Isopach map, grain size distributions and deposit thickness Vs. isopach area. 25
Figure 3.6 Grain size distribution of proximal, mid and distal deposits. 27
Figure 3.7 SEM images of of particles from the hydrothermal explosion deposit 27
Figure 3.8 Seismogram and amplitude spectrogram of the explosions 30
Figure 3.9 Fragmentation apparatus, and experimental path during the experiments 32
Figure 3.10 Variation in grain size of pre-sieved material, and FESEM of experimnetally-produced particles 34
Figure 3.11 Ejection velocities of particles. 35
Figure 3.12 Energy Vs. crater size, and energy convertion ratio 37
Figure 3.13 Coneptual model of the Gengissig hydrothermal explosions. 39
Figure 4.1 Upper Te Maari locaion, and morphology before and after the eruption. 45
Figure 4.2 Upper Te Maari crater hydrothermal system prior to the eruption 46
Figure 4.3 Field picture of different debris avalanche block type and comparison with ballistics 47
Figure 4.4 Photographs of investigated samples 48
Figure 4.5 Fragmentation apparatus, and experimental path during the experiments. 49
Figure 4.6 Cumulative grain size distribution of experimentally-produced fragments 51
Figure 4.7 Open porosity, ejection velocity, and weight % fines as a function of the energy 53
Figure 4.8 From cored to fragments: differences in ejection and fragmentation behavior 57
Figure 4.9 Conceptual model of the west-direct blast of the Upper Te Maari eruption. 61
Figure 5.1 Campi Flegrei location and conceptual model of Solfatara hydrothermal system 67
Figure 5.2 Photographs of investigated samples 69
Figure 5.3 Fragmentation apparatus, and experimental path during the experiments 71
Figure 5.4 Petrophysical properties of investigated samples 73
Figure 5.5 Explosive energy as function of sample porosity. 75
Figure 5.6 Cumulative grain size distribution of experimentally-produced fragments 76
Figure 5.7 Median, sorting, and weight % of fines as function of the explosive energy 77
Figure 5.8 Fragmentation speed and ejection velocity as function of the explosive energy 80

# *List of Tables*

Table 3.1 Deposit volume, craters size data, and energy estimations ..... 28
Table 3.2 Permeability measurements ..... 31
Table 3.3 Experimental samples description..... 32
Table4.1 Sample properties and experimental results at the different investigated conditions ..... 54
Table 5.1 Main petrophysical features of the investigated tuffs ..... 72
Table 5.2 Sample properties and experimental results for dry, partial- and fully saturated conditions ..... 79

# *List of Equations*


General formulation for the explosive energy [2.1] ..... 11
Explosive energy as a modified form of Bernoulli's equation [2.2] ..... 12
Expansion work as function of internal energy variation [2.3] ..... 12
Flashed steam fraction under irreversible conditions [2.4] ..... 12
Explosive energy under irreversible conditions [2.5] ..... 13
Volume calculated by exponential decay of deposit thickness [3.1] ..... 28
Empirical relationship between crater diameter and ejecta volume [3.2] ..... 28
Thermal energy available for craterization and debris ejection [3.3] ..... 36
Empirical relationship between crater diameter and craterization energy [3.4] ..... 36
General formulation for the kinetic energy [4.1] ..... 52
General formulation for the explosive energy [4.2] ..... 52
Explosive energy as a modified form of Bernoulli's equation [4.3] ..... 58
Fragmentation threshold criterion for crack propagation through elastic media [4.4] ..... 58
General formulation for the kinetic energy [4.5] ..... 59
Connected porosity from matrix geometric and measured volume [5.1] ..... 69

This page was intentionally left blank.

# *Chapter 1*

# *Introduction*

*Amidst the other horrors, the mighty mountain*

*now cast up columns of boiling water.*

*The Last Days of Pompeii (1850)*
*George Bulwer-Lytton*

## 1.1 Steam-driven eruptions in volcanic systems

Eruptions in magmatic and hydrothermal systems are violent phenomena, which result in an explosive release of energy generated by the mechanical work of expanding fluids (Mastin, 1995; Zhang, 2000; Thiéry and Mercury, 2008, 2009; Thiéry et al., 2010). The best known and studied eruptions are consequent to the expulsion of magma and magmatic gases from a vent up to the earth surface (Gilbert and Sparks, 1998, Sigurdsson et al., 2015 and references therein). Yet a large percentage of eruptions, perhaps the majority, do expel only fragments of non-juvenile rocks disintegrated by the expansion of flashed steam, gas or super critical fluids (Mastin 1995; Browne and Lawless 2001; Morgan et al. 2009). Many partially exotic names have been introduced for these type of events, and referred to specific eruption mechanisms (Barberi et al. 1992; Mastin 1995; Browne and Lawless 2001), such as "hydro-explosions", "hydrothermal eruption", "steam-blast eruptions", "phreatic eruption", "boiling-point eruptions", "gas-driven eruptions" and "mixing eruptions", often creating ambiguity. Nevertheless the main cause of all of these explosive events is the presence of water at near surface, and its expansion as liquid or gas phase is driving them. Thus this eruption type is defined by the term *"steam-driven* eruption" throughout this study.

The most common steam-driven eruptive events are represented by both phreatic and hydrothermal eruptions (following the terminology presented in Browne and Lawless, 2001). Heated ground or surficial water is the driving fluid behind phreatic eruptions (Stearns and McDonald 1949), but the input of mass (fluids) and energy deriving from magma is thought to be the trigger (Figure 1.1; Browne and Lawless, 2001). Hydrothermal eruptions instead specifically involve water close to its boiling temperature ("boiling-point" eruption of Mastin, 1995). These type of eruptions are generated in the near-surface, and result from the (rapid) formation of steam following a (sudden) pressure decrease (Browne and Lawless 2001; McKibbin et al. 2009). Generally hydrothermal eruptions do not result from any input of mass or energy directly derived from magma (Figure 1.2, Figure 1.4).

Steam-driven eruptions can last from seconds to hours (Browne and Lawless 2001; Jolly et al. 2014), and produce craters spanning from a few meters up to more than 2 km in diameter (Muffler et al. 1971; Browne and Lawless 2001). Typical ejection velocities vary

between few tens of m/s up to more than 200 m/s (Mastin 1995; Kilgour et al. 2010; Breard et al. 2014). Deposits are generally of low volume ($<10^5$ $m^3$); they are typically very-poorly sorted, matrix-supported, and may contain hydrothermally altered clasts if they occur in geothermal reservoirs (Nelson and Giles 1985; Browne and Lawless 2001; Morgan et al. 2009). The deposits, though generally hardly recognized or badly preserved, provide important insights to quantify the dynamics and energy of these explosive events. The rock properties of the groundwater and hydrothermal systems reservoir, in particular, control the efficiency in the energy release during an eruption, directly affecting the craterization and ejection behavior (Browne and Lawless 2001; Thiéry et al. 2010; Breard et al. 2014; Lube et al. 2014; Mayer et al. 2015; Montanaro et al. 2016).

Figure 1.1 Phreatic eruption at Laguna Caliente on Poas Volcano, February 25, 2014 (on the left; source OVSICORI), and at White Island in New Zealand, on the August 19, 2013 (on the right; GeoNet webcam). Both the areas touristic site.

Steam-driven eruptions are common in many volcanic terrains as well as other areas of high heat flow, where abundant hydrothermal or magmatic activity favors conditions for (rapid) generation of steam and pressure build-up (Figure 1.2). Active crater lakes also represent an increased potential for such events as they favor condensing of rising fluids from below. This condition turns these lakes to be very sensitive to sudden pressure changes (fluid injections), increasing the likelihood of a steam-driven eruptions (Manville et al. 2015).

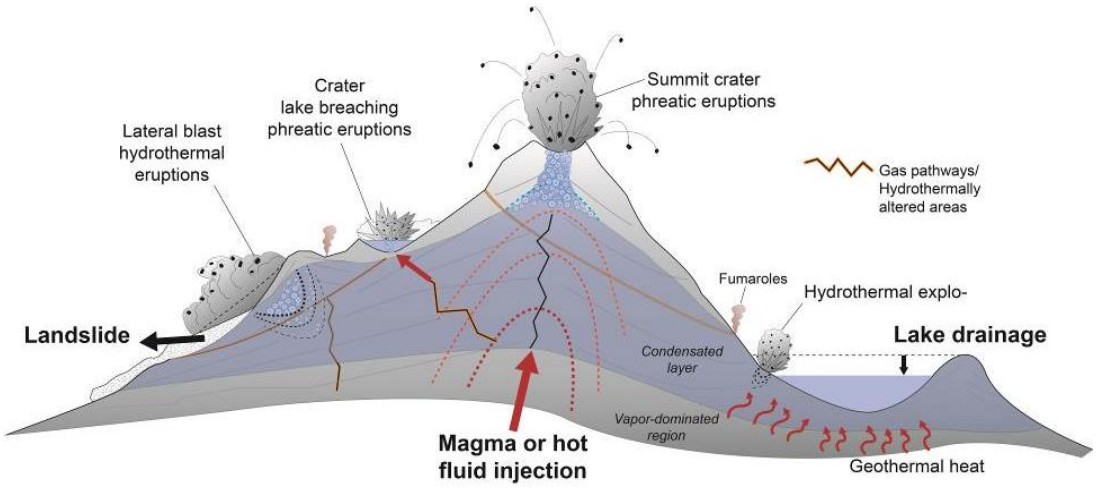


Figure 1.2 Schematic model of the main type of steam-driven eruptions and triggering mechanisms within a volcanic system.

Steam-driven eruptions produce effects in a limited area surrounding the explosive vent(s). Still, in densely populated zones, or in geothermal areas which often host power plants as well as visitor parks, they can represent highly dangerous events. For similar eruptions major hazards are produced by:

1) ejected ballistic blocks (Etna in Italy, 1979 and 1987: 9 and 2 deaths; Agua Shuca in El Salvador, 1990: 26 deaths; Mayon in Philippines, 2013: 5 deaths);

2) discharge of clouds of toxic or paralyzing gases (Larderello in Italy, 1282: uncertain number of deaths; Dieng in Indonesia, 1979: 149 casualties; Nyos in Cameroon, 1986: over 1700 casualties; Asa in Japan, 1997, 2 casualties);

3) production of base surges, lahars and directional blasts, sometimes accompanied by debris avalanches (Bandai in Japan, 1888: 461 victims; Karkar in Papua New Guinea, 1979: 2 victims; Ontake in Japan, 2014: 57 victims).

The recent hydrothermal eruptions at Mt. Ontake in Japan (Figure 1.3; Yamamoto, 2014; Kato et al., 2015), as well as Ruapehu and Te Maari, in New Zealand (Figure 1.4; Kilgour et al., 2010; Breard et al., 2014), further highlighted the major proximal hazards of these events. Moreover they occurred with little or no pre-eruptive monitoring signals (Hurst et al. 2014). Indeed a part of their hazard potential is due to the fact that such eruptions are difficult to predict in terms of timing and magnitude as they have manifold triggers (variances in groundwater and heat systems, earthquakes, material fatigue, water level failure, etc.; Barberi et al., 1992; Browne and Lawless, 2001). Consequently there are many problems concerning their detection in volcano monitoring systems; even though steam-driven eruptions have precursor phenomena, it is very difficult to single out the specific precursors (Barberi et al. 1992; Browne and Lawless 2001).


Figure 1.3 Eruption at Mount Ontake, Japan on the 27 September 2014 (video source BBC News). In the BBC frame video a pyroclastic flows is roaring down the valleys on the side of the volcano. Hundreds of hikers were on the volcano at the time of the eruption, which killed 57 people and left six others missing.


Figure 1.4 21 November eruption of Upper Te Maari crater, on the northern slope of Mount Tongariro (video source TMT News). The Te Maari erupted again after having rumbled back to life on the 6th August, after more than a century of quiet.

The conditions that cause steam-driven eruptions arise through a (rapid) increase in temperature or decrease in pressure. The contained fluids may flash to steam, resulting in significant volume increase and fragmentation of the enclosing rocks (McKibbin et al. 2009). The heating is the result of an increase in reservoir energy, (e.g. by injection of magma or magmatic gases), as in the recent Mt. Ontake eruption (Kato et al. 2015). Pressure reduction can arise due to removal of fluid from a geothermal area, for instance by exploitation, or a reduction in confining pressure by a landslide (e.g. Te Maari eruption; Breard et al., 2014), erosion processes, lowering of groundwater, or rapid draining of an overlying lake (e.g. Gengissig lake in Figure 1.5; Montanaro et al., 2016; Morgan et al., 2009; Muffler et al., 1971).

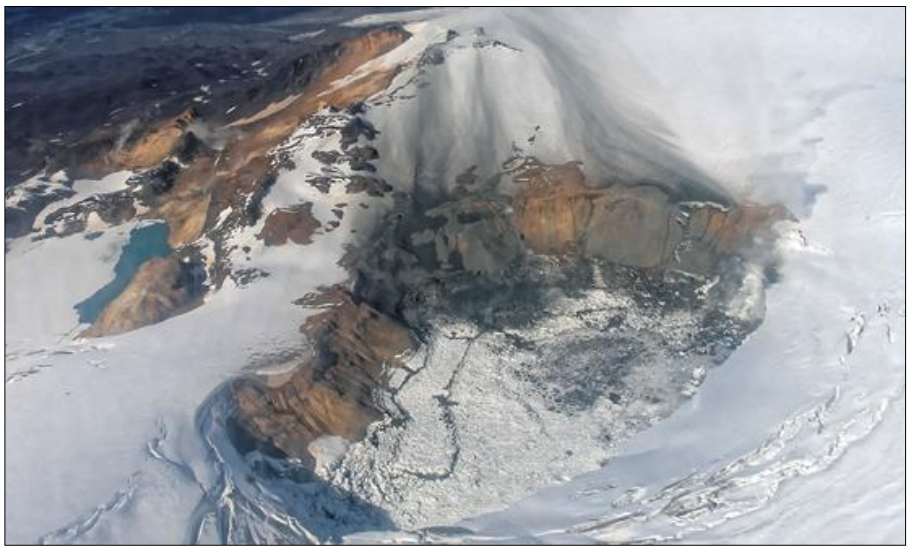

Figure 1.5 Aerial photo of Gengissig ice dammed on the 16th of August 2013; several small fans of ejecta are visible north of the lake to a distance of about 1 km. Hydrothermal explosions were triggered by the sudden lake drainage (photo of Hannah I. Reynolds).

The response of a groundwater or geothermal system either to (rapid) increase in temperature or (sudden) decompression depends mostly on its permeability. Highly permeable rock systems are likely to efficiently release any steam generated, thus largely preventing pressure build-up and eruption. However, if such a system is capped by low-permeable layers, steam generated may not escape and pressurization of the groundwater or geothermal system is likely; sufficient pressurization may cause rupture of the capping layers and thus initiate rapid depressurization and thus eruptions (Browne and Lawless 2001; Seki et al. 2015; Montanaro et al. 2016).

## 1.2 Scope and objectives

The scope of this thesis is to find answers to some open questions concerning the very poorly-understood and constrained phenomena of steam-driven eruptions.

Amongst all the considerations listed above, one of the fundamental question remains: what is controlling their explosive power? The present thesis aims at addressing this question by means of a multidisciplinary study which includes detailed field surveys of specific volcanic areas, laboratory studies, and thermodynamic models.

Specifically this study investigates the role played by 1) the pressure, temperature and liquid fraction within a system before an eruption, and 2) the nature of the rock hosting the hydrothermal system. These parameters control the rate at which energy is released and in turns the violence of such explosive events.

To this end two steam-driven eruptions which occurred at the time of this PhD were taken as case studies and investigated through a multidisciplinary approach. The first were a series of small hydrothermal explosions that occurred at Gengissig lake, within the Kverkfjöll caldera in Iceland; the second was an hydrothermal eruption involving the Upper Te Maari crater located on Tongariro volcano in New Zealand. A combination of different methodology (field, laboratory, theoretical, and seismic studies - if available) was used to analyze the mechanisms and characteristics of these steam-driven explosive events, together with their energetics. These two case studies represent two end-member conditions of steam-driven eruptions in terms of size, energy and eruptive mechanism. They show well how different physical condition of the involved hydrothermal systems, and diverse lithologies led to very different fragmentation and ejection behavior of the enclosing rocks. In addition to these two natural cases, a third study has been performed. This was focused on the influence of the liquid fraction and rock lithology in controlling the explosive energy, as well as the fragmentation and ejection behavior. Rapid decompression experiments on tuff rocks from Campi Flegrei, supported by analytical modelling, were used for this purpose.

Field studies were carried out firstly to collect samples used for the laboratory-based investigations, and secondly aimed to define the geology of the source area, thus giving estimates on the experimental conditions. Throughout this PhD a large part of the studies is partially, or totally supported by the experimental results. These are based on rapid decompression experiments, performed to reproduce diverse scenarios likely for steam-driven eruptions in the different volcanic setting investigated.

## 1.3 Overview of dissertation

**Chapter 2** shows an overview of the explosivity of steam-driven eruptions in magmatic and hydrothermal systems. The factors controlling the explosivity are briefly discussed together with previous methods and models used to estimate the steam-driven eruption energetics. A theoretical background on the thermodynamic irreversible approach is presented, which was used here to estimate the explosive energy of water, fueling this type of eruptions. Finally a detailed description of the experimental methods used throughout this study is reported.

**Chapter 3** and **4** present the results of multidisciplinary case studies used to unravel the energetic aspect, and other important parameters, of two steam-driven explosive events. **Chapter 3** includes a complete characterization of a series of small hydrothermal explosions that occurred at Gengissig lake (Kverkfjöll volcano, Iceland). Field data, laboratory studies, and analytical models with seismic data are used to provide robust estimates on energy release and partitioning for such small-size yet hazardous, steam-explosion events. The characterization of the stratigraphic sequence involved in the explosions provided an opportunity to understand the effect of the host rock lithology, as well as the presence of very low permeable layers, in controlling the explosion dynamics and energy partitioning. **Chapter 4** describes a study focusing on the energy budget and the ejection of ballistics during the hydrothermal eruption of Upper Te Maari crater (Mt. Tongariro, New Zealand). In this case the field data included a characterization of ballistic lithology, and in turn of the nature of the explosion-source locations in the vent region. These information were used in combination with decompression experiments and analytical modelling to estimates the effect of initial pressure and temperature condition, as well as of the rock lithology, on 1) the fragmentation behavior, 2) mechanism of ballistic ejection, and 3) the eruption energy and partitioning.

**Chapter 5** illustrates the study on the effect of liquid fraction and rock properties on the steam-driven eruption explosive power. Experimental and thermodynamic modelling have been used to investigate the fragmentation and ejection behavior of different tuffs at high temperature and pressure, and under partial (50%) and fully saturated conditions. This study highlights how increased amount of liquid fraction, together with the different properties (porosity, permeability and strength) of the used tuffs play a primary role in controlling the explosivity of steam-driven events.

**Chapter 6** includes a synthesis of the obtained results as well as the conclusions from this doctoral work. Finally key findings are discussed and future perspectives presented.

This page was intentionally left blank.

This page was intentionally left blank.

# *Chapter 2*

## *Explosivity of steam-driven eruptions*

*And the volcano…the volcano! The first time I had to try to climb it, we slogged for four hours upward. After I climbed for two hours, I just sat down, gasped and said, 'I'm sorry, I can't make it.' But after a rest I did make it, and at the top I could have just lain down and died…*

*Ingrid Bergman about Stromboli (1980)*

### 2.1 Introduction

An explosion is the violent response of a system to a physico-chemical perturbation, and the resulting energetic metastable state. Fast thermodynamic processes, such as the heating of water by magma, or rapid depressurization of a liquid produce highly transient metastable states, which tend to reach equilibrium in a very rapid and explosive way (Thiéry and Mercury 2009). Thus, rapid physical transformations of water are the causes of strong instabilities, which lead to explosive manifestations such as steam-driven eruptions. Particularly for hydrothermal systems, the (sudden) decompression of hot pressurized water is the main cause producing such events (Browne and Lawless 2001). The (rapid) release of water stored at a temperature above its atmospheric-pressure boiling-point results in instantaneous vaporization (steam flashing). Steam-driven eruptions thus occur with different degrees of explosivity, as their violence is related to the magnitude of the decompression work that can be performed by the steam flashing (Mastin, 1995; Thiéry and Mercury, 2008, 2009; Thiéry et al., 2010).

In this chapter the factors controlling the explosive power of this type of eruption, together with a description of the classical models used to estimate the associated energy and eruptive dynamics are discussed. The irreversible thermodynamic approach, used in this study to calculate the explosive energy is presented, together with a brief description of the different types of hydrothermal and volcanic environments as a function of their explosion energy. Finally the experimental method utilized to investigate the steam-driven explosivity involved in the different case studies, is explained.

### 2.2 Factors controlling the explosivity of steam-driven eruptions

The violence (or explosive power) of these eruptions depends largely on the different explosivity of fluids (liquid or gas) driving them, as well as on the rate of mechanical energy release. Both these factors are in turn controlled by 1) the pore liquid fraction and

its physical condition (pressure-temperature) before the eruption (Mastin, 1995); and 2) the mechanical properties (e.g. lithology-texture, permeability, strength) of the rock hosting the hydrothermal system (Muffler et al. 1971; Thiéry et al. 2010; Haug et al. 2013; Galland et al. 2014). More specifically the pressure-temperature conditions together with the porosity control the phase of the fluid and the stored explosive energy, respectively. Instead the energy partitioning in terms of fragmentation energy and kinetic energy mostly depends on the rock porosity, permeability, and strength (Montanaro et al., 2016; Thiéry and Mercury, 2009). A wide range of initial temperature, pressure and liquid fraction, as well as a variety of rock types characterizes the volcanic environments affected by steam-driven eruptions (Browne and Lawless 2001). Consequently this eruption type is very versatile, exhibiting a wide spectrum of eruptive styles.

## 2.3 Previous methods and models used

The conversion of thermal energy stored in water into mechanical energy is powering the steam-driven eruptions. This results in the fragmentation, acceleration and lifting of debris, as well as in the generation of seismicity and shock waves. Nevertheless the energetics and dynamics of this type of eruptions are still not well understood. For many of the known steam-driven eruptions, since the early 1950s (White 1955), the estimation of the mechanical energy release, final temperatures and the produced steam fractions has been done by using basic principles of thermodynamics. Over time, different models have been proposed to estimate the energy budget of steam-driven eruptions, mostly based on two groups of proxies: 1) crater size and ejecta volume, and 2) physical-thermodynamic properties of rock and fluid phases. Both empirical methods, based on the relationship between craters formed and explosive energy of artificial explosions (Murphey and Vortman 1961; Goto et al. 2001; Valentine et al. 2012), and ballistic-based approach by using the distance of large ejected clasts (Sherwood 1967; Wilson 1972; Steinberg 1976), can be included in the first category. The second category included the analyses of thermal energy available in hydrothermal systems and the thermodynamics of the resulting eruptions (Muffler et al. 1971; Mastin 1995; Montanaro et al. 2016).

All of these methods have been applied to assessing the energy involved in steam-driven eruptions, yet all of them yield very different results. Moreover estimations of the energy partitioning into fragmentation and ejection of produced debris have been rarely explored. The reason for this can be explained as follows:

1) the field-based explosion experiments approach were developed for magmatic and phreatomagmatic eruption, therefore the difference in scale, temperature, mechanisms and fluid properties in the steam-driven eruptions needs to be taken in account. New experiments have been recently carried out (Valentine et al. 2015 and reference therein), with the aim to cover a wider range of eruption type, and thus to fill this gap;

2) methods based on ballistics of large ejecta are not applicable where most of the ejected material are mainly fine-grained clast or mud, as in many steam-driven eruptions.

Thus a good constraint on grain size distribution, together with the maximum distances of ejecta is needed to apply such a method (Montanaro et al. 2016);

3) thermodynamic estimates of the energy required to transport ejecta represent an upper limit because the conversion of this heat to mechanical energy is inefficient and neglects many dissipative processes as, for example, the production of new surface area by brittle processes (Mastin 1995; Büttner et al. 1999);

4) the energy partitioning into fragmentation and viscoelastic deformation depends strongly on media properties (Murphey and Vortman 1961; Goto et al. 2001; Ohba et al. 2002; Valentine et al. 2012; Montanaro et al. 2016), which then play roles of first, secondary, or higher orders for methods based on the length-energy scale. Thus the energy related to the crater size varies according with the cube root or the "quarter root" of the explosive energy, or somewhere in between (Holsapple and Schmidt 1980; Ohba et al. 2002).

Combinations of such methods have been used to interpret field data (Kilgour et al. 2010; Breard et al. 2014; Lube et al. 2014); in particular if applied together with laboratory studies and seismic data they yield good estimate on energy budget and partitioning, especially for small scale events (Montanaro et al. 2016). Still, these methods must be generally used with caution (Browne and Lawless 2001), and in particular their application must take care of specified validity conditions (explosive type, site geometry, confinement, explosion depth, etc.). In addition to the energetic aspect, few studies have attempted to model the dynamics of these eruptions, both theoretically (Mckibbin, 1989; Mckibbin et al., 2009; Fullard and Lynch, 2012a, 2012b) and experimentally (Foote et al. 2011; Haug et al. 2013; Mayer et al. 2015). More insight on their dynamics have been inferred from studies of the deposits of recent events occurred at Gengissig lake in Iceland (Montanaro et al. 2016), and at Ruapehu and Tongariro volcanoes, in New Zealand (Kilgour et al., 2010; Breard et al., 2014).

## 2.4 Explosivity of water in hydrothermal system: theoretical background

The explosive energy released by the expansion work of the fluids (gas or liquid) in the rock pore space (from the breaking pressure in the pore up to the atmospheric pressure) is:

$$E_{Expl} = m \times \Delta U \qquad [2.1]$$

where $E_{Expl}$ is the available explosive energy which can be released in the expansion of the fluids (J), m is the mass of fluid already existing in the pores at the moment of the failure (g), $\Delta U$ is the difference in internal energy of the fluid under the conditions before and immediately after the expansion up to atmospheric pressure (J/g).

The estimated $E_{Expl}$ gives the amount of energy which can be converted into fragmentation ($\Delta E_f$), gravitational potential ($\Delta E_p$), kinetic ($\Delta E_k$) and all other forms of mechanical energies (noted as $\Delta E_d$) such as elastic deformation, shock waves, etc.. Thus, the energetics of fluid flows can be assessed by using a modified form of Bernoulli's equation (Wohletz 1986; Mastin 1995; Thiéry and Mercury 2009) as:

$$E_{Expl} = \Delta E_f + \Delta E_p + \Delta E_k + \Delta E_d + \textit{“frictional terms”} \qquad [2.2]$$

the last term accounting for the energy consumption due to rock-fluid internal friction. Depending upon the importance of this frictional term, isenthalpic (irreversible) or isentropic (reversible) conditions can be used to assess the maximum amount of work that can be extracted from an expansion, and the associated explosive energy (Mastin 1995; Thiéry and Mercury 2009). For the isenthalpic hypothesis all mechanical forms of energy (gravitational, kinetic, etc.) are converted to thermal energy, thus resulting as a more appropriate assumption to characterize the fluid state after complete relaxation. In the case of isentropic assumption the final state is fixed at ambient condition ($P_{atm}$ = 0.1013 MPa), where the system is charged with energy still to be consumed. Here fluids expansion and acceleration are not dissipated as frictional heating. The isentropic assumption has been mostly used to assess the expansion work in volcanological models (Wohletz 1986; Mastin 1995).

For the energy calculations in the case of steam flashing during rapid decompression an irreversible approach (Prugh, 1991) can be used. This approach gives more realistic values for the explosive energy, compared to the reversible case (Mastin 1995). Assuming that the expansion is adiabatic, but irreversible means that the only work performed is the change in volume ($\Delta V$) that occurs when the fluid-water in the rock pores changes from the P-T conditions at explosion to the final state ($P_{atm}$). Thus the expansion work must be equal to the variation in internal energy of the fluid $\Delta U$:

$$\Delta U = -P_{atm} \times \Delta V \qquad [2.3]$$

The analytical solution of equation [2.3] applied to a mass of liquid which vaporizes adiabatically enables calculation of the flashed steam fraction (Planas-Cuchi et al. 2004; Thiéry and Mercury 2009) as:

$$x = 1\text{-}f = 1 - ([P_{atm} \times (v_{initial} - v_{vap}) - U_{vap} + U_{initial}]/[U_{liq} - U_{vap} + P_{atm} \times (v_{liq} - v_{vap})]) \quad [2.4]$$

where $x$ and $f$ represent the steam and liquid fraction respectively, and $v$ is the molar volume. $U_{initial}$ (J/mol) and $v_{iniital}$ ($m^3$/mol) are calculated at the initial condition of the system. $U_{liq}$ (J/mol), $v_{liq}$ ($m^3$/mol), $U_{vap}$ (J/mol) and $v_{vap}$ ($m^3$/mol) are all calculated at 100°C and 1 bar (atmospheric-pressure boiling-point). Thiéry and Mercury (2009) compared the amount of steam fraction generated for the three possible assumption, i.e. isentropic, isenthalpic and irreversible. Their results show how the isenthalpic and irreversible depressurization yield the driest mixtures as the result of the internal friction producing an increase of entropy (Figure 2.1).

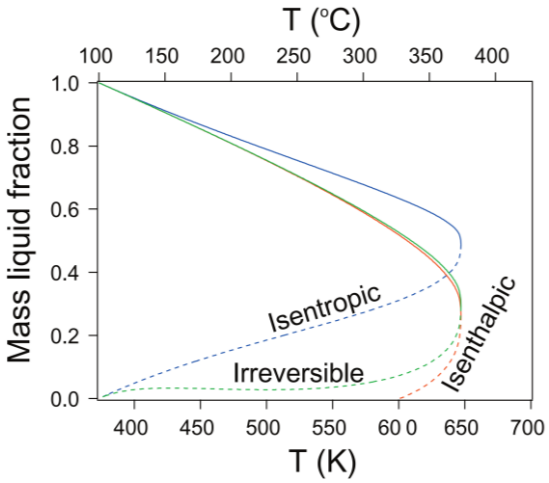


Figure 2.1 The mass liquid fraction of the liquid-gas mixture at 100°C and 1 bar produced by the depressurization of a saturated liquid (full curve) or saturated steam (dashed curve), as calculated by three types of decompression processes, i.e., isentropic, isenthalpic, and irreversible expansions.

Thiéry and Mercury (2009) also demonstrated that isenthalpic hypothesis yields a good approximation of the irreversible case, especially for liquid expansion (Figure 2.1). Under this assumption the irreversible energy of an expanding saturated liquid can be calculated as:

$$E_{Expl\text{-}I} = m_w \times (P_{atm} \times [(1\text{-}f) \times v_{vap} + f \times v_{liq}\text{-}v_{initial})]) \qquad [2.5]$$

where $E_{Expl\text{-}I}$ is the irreversible explosive energy released (in J), and $m_w$ is the mass of water (g) in the pore space (Figure 2.2).

In the case studies discussed in Chapter 3 to 5 I applied the irreversible conditions, and the equations [2.4] and [2.5] to evaluate the mechanical energy associated to the experimentally-produced steam-driven explosions.

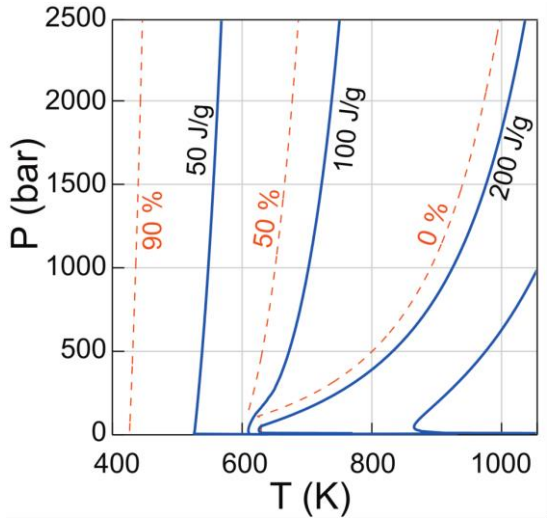


Figure 2.2 P-T diagram showing the mechanical work (full solid lines, in J/g of water) released by the irreversible adiabatic expansion of hot and pressurized steam as a function of the initial P-T conditions. Dashed lines indicate the liquid fraction (in mass percentage) of the gas-liquid mixture at a final state of 1 bar and 100°C. Modified from Thiéry and Mercury (2009).

In hydrothermal and volcanic systems different energetic contributions (i.e., fluid expansion accompanied or not by vaporization/condensation processes, isobaric boiling) can be associated to steam-driven eruptions.A synthesis of their relative contributions can be done in a pressure-enthalpy diagram (Figure 2.3; Thiéry and Mercury, 2009). The different cases are produced by the interactions in various proportions of meteoric and superficial waters, whose P-T conditions are close to the mean geothermal gradient. The main systems and their energetic source are represented by:

1) liquid-dominated geothermal systems (A), where the boiling must be triggered by a depressurization of the geothermal reservoir (Browne and Lawless 2001). Thus, the energy source comes mainly from the liquid boiling and steam expansion, well below 100 J/g of $H_2O$ (Figure 2.2).

2) supercritical or slightly subcritical fluids (B), typically found in the lithocaps of magmatic chambers (Norton and Dutrow 2001), or in deep geothermal systems (black smokers of oceanic ridges). Sudden pressure drops on such systems up to atmospheric conditions are expected to produce explosions of high power and would involve a mechanical energy of 150–200 J/g of $H_2O$ (Figure 2.2).

3) vapor-dominated geothermal systems (C) where the mechanical energy is produced by expansion of gaseous fluids, below 150 J/g of $H_2O$ (Figure 2.2).

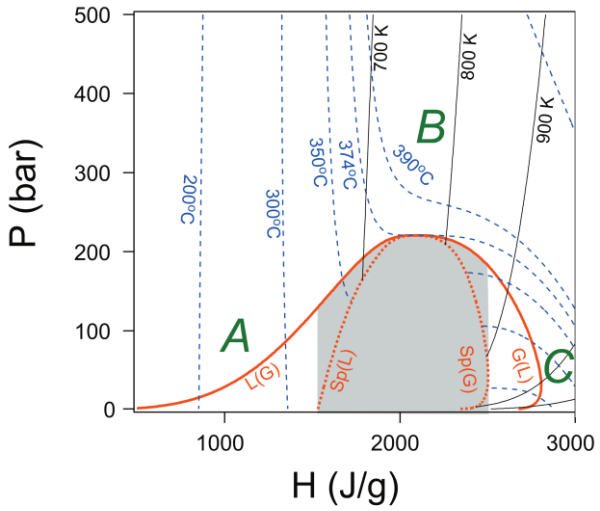


Figure 2.3 P-H diagram. Thick solid curves, binodal L(G) and G(L) curves; thick dotted curves, spinodal Sp(L) and Sp(G) curves; thin dashed curves, isotherms calculated at T = 200, 300, 350, 374 (critical isotherm), 390, 500°C; thin solid lines, isentropic expansion curves labelled by the initial fluid temperatures (K) at 1000 bars. A, liquid-dominated geothermal systems of low enthalpy; B, high-pressure hydrothermal systems of medium enthalpy; C, vapor-dominated geothermal systems of high enthalpy. Modified from Thiéry and Mercury (2009).

## 2.5 Experimental investigation of steam-driven eruptions

In this study an experimental approach, based on a rapid decompression experiments, is used to investigate diverse scenarios likely for steam-driven eruptions in various type of volcanic setting. The decompression experiments were performed in the fragmentation

bomb at LMU, described in detail by Alidibirov and Dingwell (1996) and developed further by e.g. Alatorre-Ibargüengoitia et al., (2010), Rager et al. (2014), and Mayer et al. (2015).

In these experiments fragmentation can be triggered by decompression of 1) argon gas, 2) steam, or 3) water flashing to steam within the connected pore space of the samples. The device permits the accurate control of temperature, gas overpressure and decompression rate in order to best represent variable magmatic and hydrothermal conditions. It consists of a large upper a stainless steel low-pressure tank (l =3.0 m; d =0.4 m) at ambient pressure and temperature conditions, and a lower high-pressure chamber (autoclave) containing the sample and which is heated and pressurized by either argon gas or steam. The autoclave is separated from the upper chamber by a series of diaphragms (Figure 2.4).

In this study two autoclave types have been used. The first one, developed by Scheu et al. (2006) and Spieler et al.(2004b), allowed for samples with 26 mm diameter and 60 mm length, and was utilized for the experiments involving tuffs rocks which contain small enclaves in a ashy matrix (see Chapter 5). The second type has been designed to reduce the influence of large lithic enclaves (up to 30 mm in size) found within the sample material used for the Te Maari case study (see Chapter 4). In this case the set-up was changed to allow samples of up to 34 mm diameter and 70 mm length (Montanaro et al. 2016). This second setup-type was further use to perform decompression experiments involving large grain size range of loose material for the Gengissig case study (see Chapter 3).

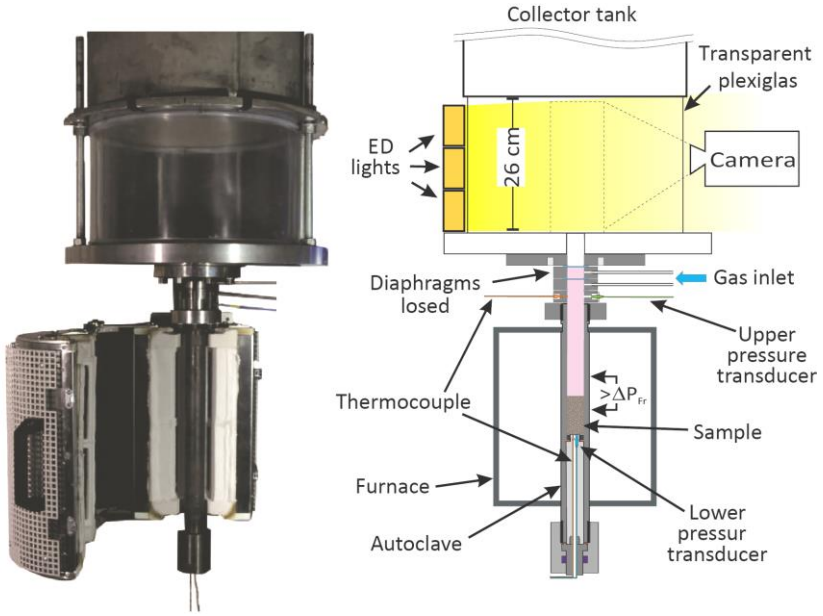


Figure 2.4 Fragmentation bomb setup: frontal (camera) view of experimental setup (left) and schematic drawing (right) of the fragmentation bomb used during this study (Mayer et al. 2015). More information in the text.

The controlled rupturing of the diaphragms initiates the rapid decompression of the autoclave. Following the diaphragm failure, a shock wave travels upwards into the low-pressure collector tank, and a rarefaction wave propagates downwards into the autoclave, traveling through the sample. Under argon and steam expansion a brittle fragmentation of

the sample is expected to occurs in a layer-by-layer way (Alidibirov and Dingwell 2000; Fowler et al. 2010; McGuinness et al. 2012), and the particles are ejected into the upper chamber. In case of water flashing to steam the fracturing may be less dependent on the decompression front, but more on the orientation of pore space and eventually pre-existing fractures (Rager et al. 2014). For each sample the fragmentation speed (Spieler et al. 2004a) is calculated by using the time delay $\Delta t$ of the pressure drop over the entire sample, as recorded by the transducers above and below the sample, and the sample length Scheu et al. (2006).

Prior to the experiment, each rock sample is mounted into a cylindrical steel crucible. For the argon-dry decompression experiments samples were mounted into the crucible and directly placed inside the autoclave ready for fragmentation experiments. For the experiments with steam condition the mounted sample is placed within the autoclave together with a specific amount of distilled water. This amount of water is calculated by means of steam tables, and allowed to achieve the desired pressurization within the connected pore space of the sample, and in the remaining autoclave chamber above the sample, solely by steam pressure. Temperature rise up to the boiling point, and gases generated upon vaporization increase the pressure in the autoclave until the targeted dwell conditions are reached. Before triggering the fragmentation an equilibration time of 10 minutes is generally complied. For experiments in the presence of steam-flashing, mounted samples are submerged in water and placed under a vacuum for at least 72 h to facilitate the water absorption within the connected porosity assuring maximum water saturation. During the decompression of the system, the phase transition from liquid water to water vapor is crossed. During the experiments the ejection of the sample is filmed by a high-speed camera (Phantom V710®347, Vision Research, USA). The entire ejection is monitored at 10.000 frames per second through a transparent Plexiglas inlet at the bottom of the large chamber. This allows the tracking of fragmented particles and an estimation of their ejection velocities.

The fragmented material is collected from the large chamber and its grain size distribution is analyzed using dry sieving at half-$\phi$ steps of particles >63 μm in size. Due to the sealing between the Plexiglas cylinder and the collector tank, as well as the adhesion of very fine particles on the lid and along the rim of the tank, a complete recovery of the very finest fraction is not possible; however, a minimum weight yield of 90-95% is generally achieved.

This page was intentionally left blank.

This page was intentionally left blank.

# *Chapter 3*

## *Multidisciplinary constraints of hydrothermal explosions based on the 2013 Gengissig lake events, Kverkfjöll volcano, Iceland*

*I move around a lot, wherever there is*
*a volcano with an attitude.*

*Harry Dalton in Dante's Peak (1997)*

### 3.1 Introduction

Unrest in geothermal areas can be manifested in jetting or eruption of hydrothermal fluids (steam, water) and substantial amounts of solid material (mud and rock fragments). Such events are commonly referred to as hydrothermal explosions, a type of non-juvenile eruption, or "boiling-point eruption" (Mastin, 1995). The term "explosion" is here used as opposed to "eruption" following the terminology presented in Muffler et al. (1971).

Here a multidisciplinary approach was chosen to study the mechanisms and the energetics of small-sized hydrothermal explosions occurring on August 16th, 2013 at Kverkfjöll, Iceland. These explosions were associated with a sudden drainage of an ice-dammed lake and represent a low-energy end-member case compared with the recent hydrothermal eruptions at Mt. Ontake in Japan (Yamamoto 2014) and Te Maari, in New Zealand (Lube et al. 2014). The latter involved different mechanisms and also larger volumes, durations, products and types of confining rock. The Kverkfjöll event presents a unique opportunity to shed light on this low-energy hydrothermal explosion type. A detailed field surveys, sampling of deposits, laboratory studies, and analytical models with seismic data to define their characteristics, and understand the role of host-rock involved in the explosions.

### 3.2 Geological setting of Gengissig lake

The Kverkfjöll central volcano is a mountain massif with a relief of 1200 m, located in central Iceland, at the northern margin of Vatnajökull glacier. The southern part is mostly ice covered, including two calderas (Figure 3.1). Generally Kverkfjöll eruptive products are basaltic with lithologies dominated by pillow lava, hyaloclastite, and fine-grained tuffs (Óladóttir et al. 2011). No volcanic eruptions are known to have occurred in the last 1100 years but several moderate-sized explosive basaltic eruptions have occurred in the

Holocene (Óladóttir et al. 2011), which have been the source of catastrophic pre-historic floods (Carrivick et al. 2004). The geothermal activity is mostly concentrated along a SSW-NNE trending lineament, cutting through the volcano (Thorarinsson 1953; Olafsson et al. 2000). A 500-600 m wide and 100 m deep depression is located in the center of the active area, about 500-1000 m east of the main lineation. This depression exhibit vigorous thermal activity and the ice-dammed lake Gengissig. The lake is characterized on the northern shore by a geothermal field enclosed by ice (Figure 3.1). Here a number of (near-) boiling hydrothermal pools, sulphurous fumaroles, hot springs, and geothermal sediments are present.

## 3.3 August 16th hydrothermal explosions

On August 15th 2013, a small jökulhlaup occurred when the Gengissig ice-dammed meltwater lake drained at Kverkfjöll (Gudmundsson and Einarsson 2013). The lake level dropped 30 m to 1607 m a.s.l. in 10-15 hrs (estimated from the discharge at a gauging station in river Jökulsá, 40 km downstream from the glacier margin, and eyewitness observations of the jökulhlaup: B.Einarsson pers.communication). Wardens at a nearby hut noted that the water level in the short tributary river Volga issuing from the glacier margin about 7 km north of Gengissig was rising on August 15th between 20:30 and 23:00. On August 16th at 07:30 the river discharge was still relatively high but had subsided considerably, indicating that the draining event had waned by that time. This was confirmed by a Coast Guard helicopter inspection flight in the afternoon of the 16$^{th}$ of August. The decompression beneath the lake bed, calculated to be 4-8 Pa/s (head loss of 20-30 m over 10-15 hours), likely triggered the rapid boiling in the surficial geothermal reservoir. Subsequent to this event hydrothermal explosions occurred, producing several fans of ejecta dispersed over 1 km from the lake by southerly winds. Craters, up to 30-40 m in diameter and partially-coalesced, were formed on the northern corner of the Gengissig depression along the pre-drainage shore line. Smaller, isolated craters were generated closer to the deeper part of the lake depression (Figure 3.1a). These explosions occurred in areas where the presence of fumarole systems and boiling pools suggest a high local heat flow.

Similar hydrothermal explosions occurred in Gengissig after a draining event in 1959 (Jóhannsson 1959), in May 1968 a steam eruption occurred on the top of a hill 500 m west of Gengissig lake (Figure 3.1). Gengissig lake has drained catastrophically in jökulhlaups at least five times in the 30 years prior to 2013: in 1985, 1987, 1993, 1997 and 2002. However, it is not known whether explosions were associated with these drainage events (Gudmundsson and Högnadóttir 2009).

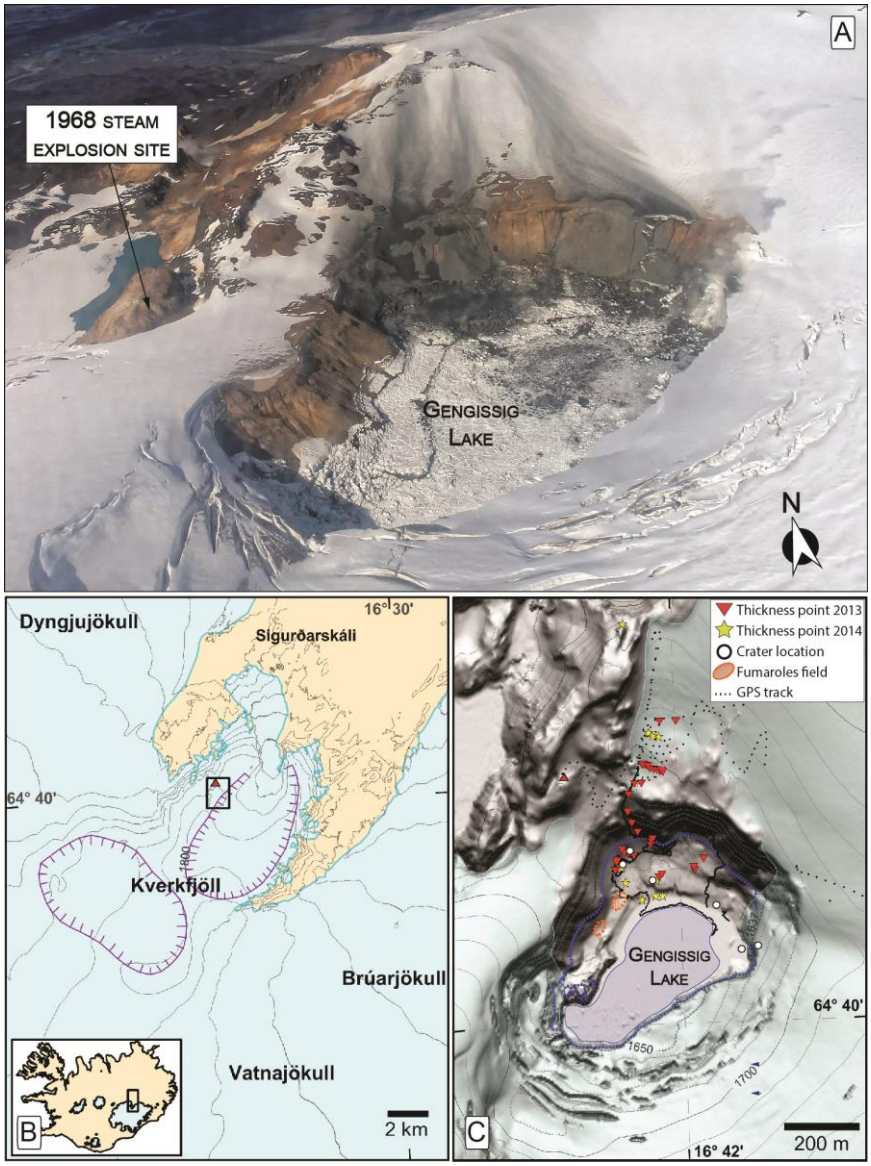


Figure 3.1 Hydrothermal explosions at Gengissig lake. Aerial photo of Gengissig lake on the 16th of August 2013; several small fans of ejecta are visible north of the lake to a distance of about 1 km. A debris blanket characterizes the area in proximity of the craters. Steaming activity is also visible at the crater sites, especially on the north-eastern side of the lake area **(**A). Map of Kverkfjöll caldera (b). Lidar map of Gengissig lake area, marked by a black rectangle in (B). Dashed and continuous blue lines represent the lake level before (1637 m) and after (1607 m) the drainage (C).

## 3.4 Field-based studies

A preliminary study of the eruptive products of the 16th August explosions was carried out by an aerial reconnaissance survey on the following day (Figure 3.1C). On 28th, an initial field campaign was conducted to sample and measure the deposit thicknesses before burial by snowfall. Additionally, boundaries of ejecta fans and the crater area were mapped with kinematic GPS. Nine months later, when a few meters of snow had largely buried the fresh deposits, I participated to a second campaign conducted to re-examine the proximal deposits and the stratigraphic sequence involved in the explosions.

In both campaigns samples were collected for component and grain-size analyses, particle shape characterization and density measurements. Field observations were then used to reconstruct the explosion scenario, estimate the volume of ejected material, and evaluate the energy partitioning in these small-size events.

### 3.4.1 Sedimentary succession-hydrothermal explosions deposits-crater features

A sedimentary succession of hydrothermally altered glacio-lacustrine unconsolidated deposit covered the depression occupied by Gengissig lake (Olafsson et al. 2000). Alteration minerals are dominantly heulandite (Ca/Na zeolite) and smectite (Fe/Mg phyllosilicates), with lesser amounts of gypsum, quartz, sulphur, jarosite, and pyrite (Cousins et al. 2013). Investigation of erosional features and the study of the exposed outcrops at the crater walls enabled a more detailed overview of the succession involved in the explosions. However, there is still a lack of detailed studies (drilling, stratigraphy etc.) concerning the subsurface structure of the Gengissig area.

Two representative outcrops from the larger coalescent craters and a smaller crater (craters 2-3) were analysed in detail. Both successions comprise poorly sorted, matrix-supported sand to gravel in layers of sub-angular to sub-rounded clasts. These coarser layers, are interbedded with clay-rich levels (Figure 3.2, Figure 3.3, Figure 3.4).

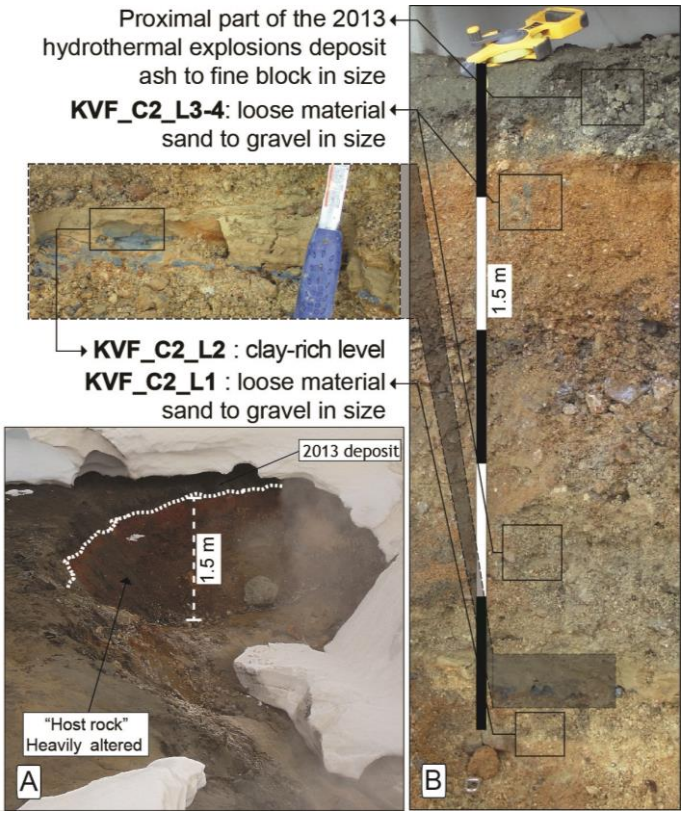


Figure 3.2 The rim of crater 2; the white dotted line marks the pre-explosion surface (A). The 1.5 m thick section studied: the black-grey layer at the top of the section is the proximal part of the 2013 deposit. Areas highlighted by square boxes indicate the portions where samples of the Gengissig sedimentary succession were taken for analyses (B).

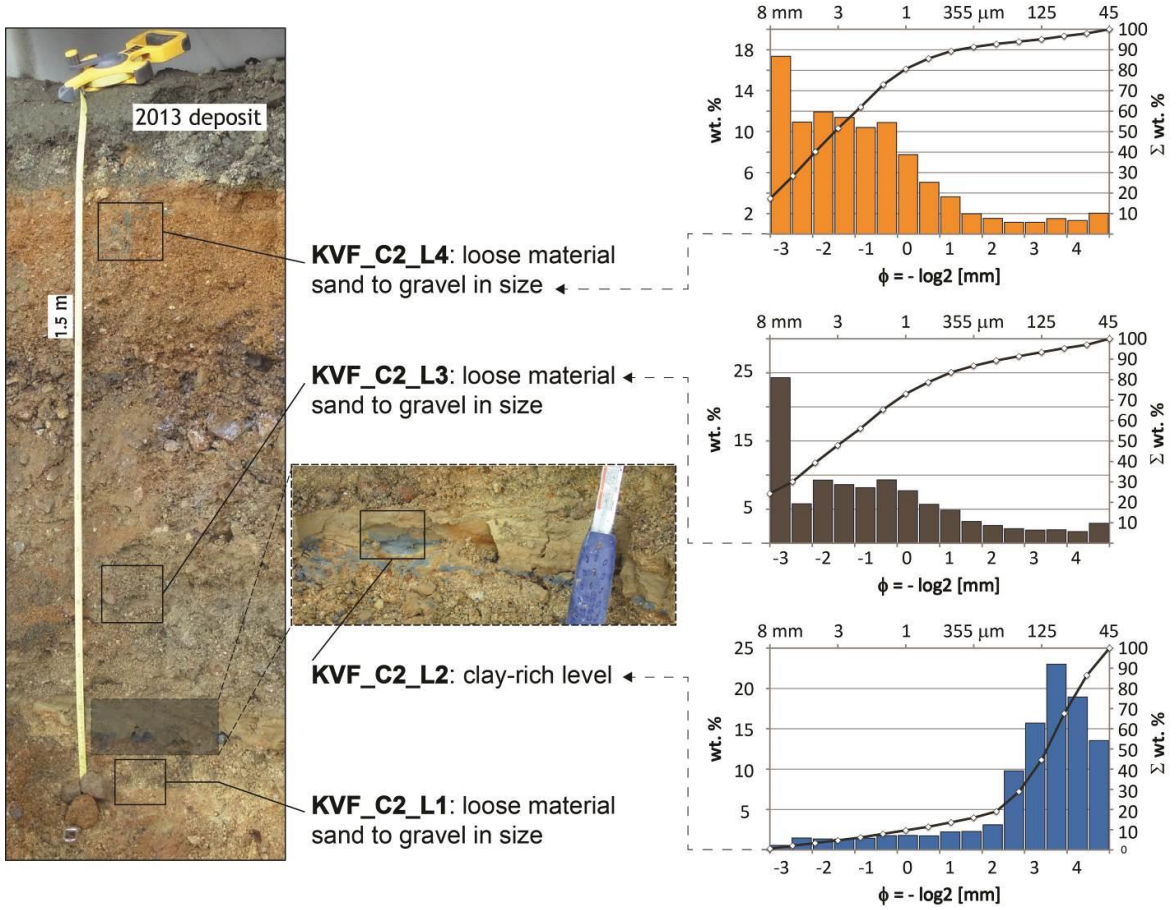


Figure 3.3 Stratigraphic sequence at crater 2 (2 A in Figure 3.5). In the inlets details of the bluish clay-rich level intercalated to coarser layers is shown. Areas highlighted by the continuous-line square indicate the portions where samples were taken for analyses (grain size distribution on the right).

The main components of the coarse fraction have basaltic lithologies varying from lavas to scoriaceous fragments, and fine-grained welded or loosely consolidated aggregates, composed of fine glass fragments and alteration minerals. The clay-rich levels (10 to 15 cm thick) vary in color from bluish to yellowish when altered and locally show relative enrichments in sand and gravel.

The north-western part of the studied area, together with an isolated area in the central part of the lake depression, exhibits varying grades of hydrothermal alteration. These areas correspond with fumarolic activity implying its role in the alteration process. In some areas alteration is limited to below a certain depth, where clay-rich levels appear to act as barriers.

Deposits of the hydrothermal explosions covered an area of approximately 0,3 $km^2$ and were dispersed towards the north forming three elongated fans. The westernmost and central fans were accessible and investigated in detail. The extent of the inaccessible proximal part of the eastern fan was mapped on the plateau (Figure 3.5 A).

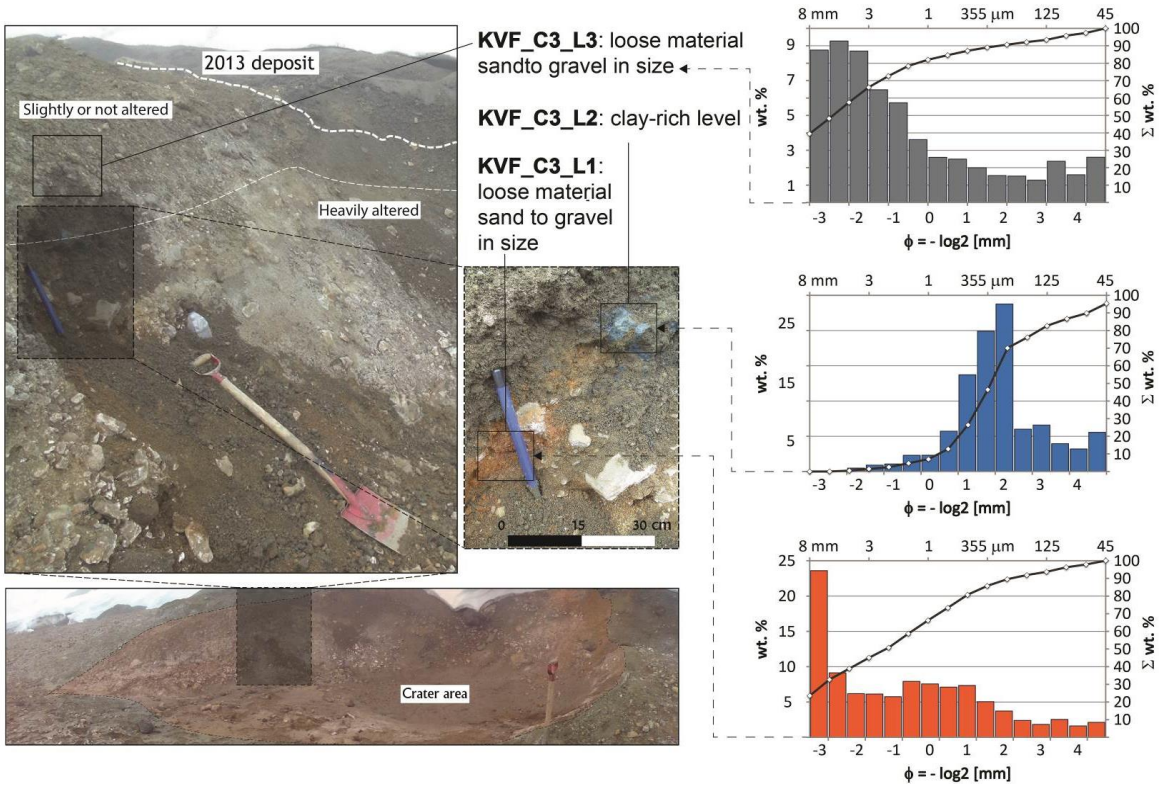


Figure 3.4 Stratigraphic sequence at crater 3 (3 A in Figure 3.5). In the inlets details of the bluish clay level intercalated to coarser layers are shown; note the change in alteration degree from above (not altered) to below (heavily altered) the clay level. Areas highlighted by the continuous-line square indicate the portions where samples were taken for analyses (grain size distribution on the right).

The two studied fans covered approximately 0.15 km2 with a maximum deposit thickness of 40 cm at the crater wall. Deposits thinned rapidly, to approximately a tenth, within 50-100 m from the crater rim (Figure 3.5 A). Most of the massively-bedded debris blanket consists of lapilli- and fine block- sized clasts ballistically emplaced around the crater areas. A minor amount of ash and lapilli was dispersed by winds to form elongated fans. The deposit reflects the composition of the underlying sequence including variably hydrothermally-altered lava lithics, intensely altered rock fragments, and recycled scoria and pumiceous clasts.

Several craters were formed following the explosions (Figure 3.1, Figure 3.5). Crater diameters on the north western side (no 1-3) range from 9 to 24 m (Table 3.1). Sizes of the craters (no 4-6) on the eastern side could not be determined. The craters exhibit two main morphologies: (1) larger craters on the north-western side characterized by irregular shapes, and (2) smaller isolated craters in the deeper part of the lake depression associated with a more circular form. The investigated craters were located at ca.1617 m a.s.l. (ca.20 m below the initial lake level).

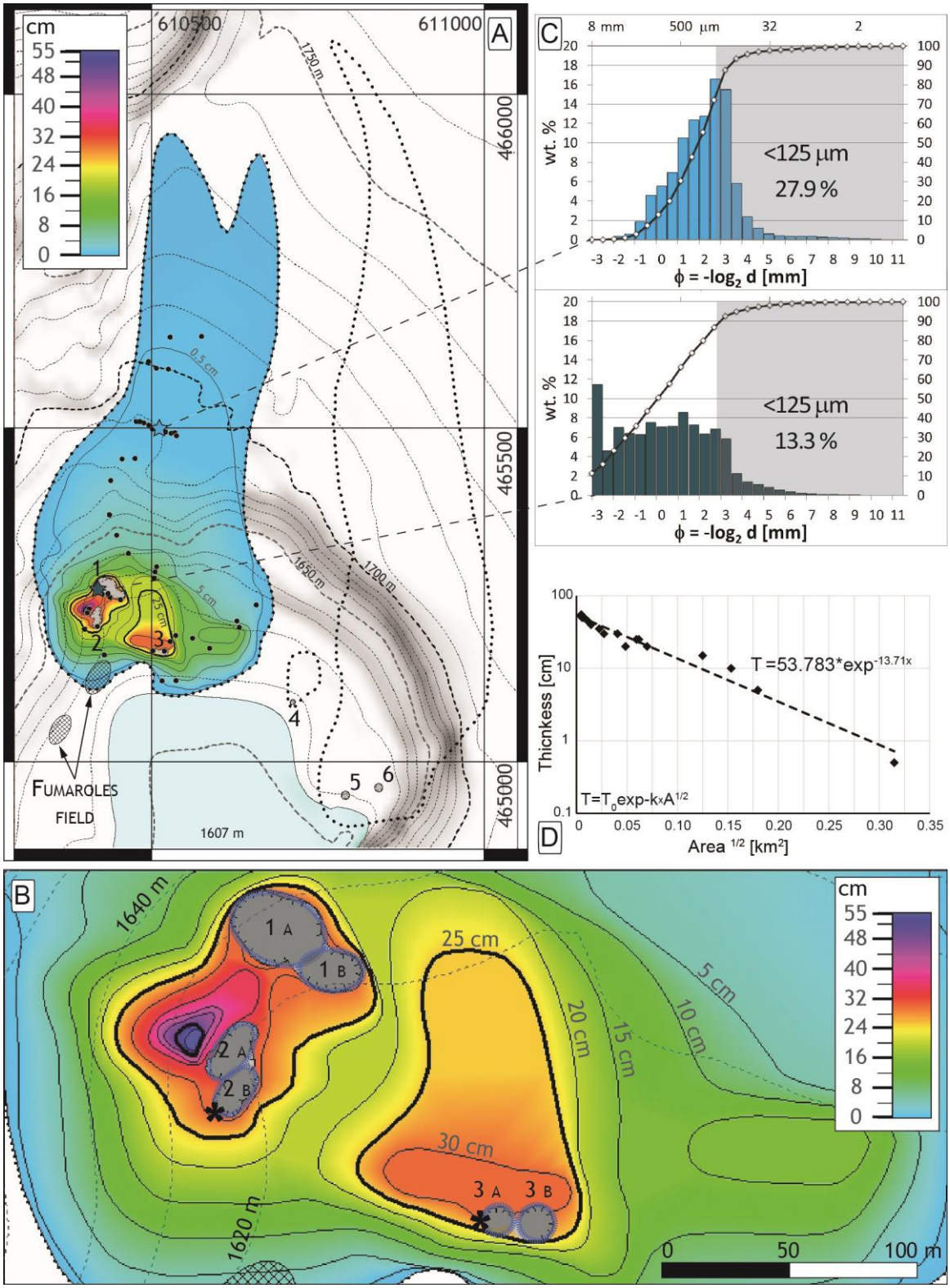


Figure 3.5 Isopach map of the 2013 hydrothermal explosions; crater locations labelled 1 to 6. Black dots denote thickness measurement points (A). Close-up of area with craters 1-3. Hashed lines indicate crater margins, used for volume and energy calculations. Asterisks indicate the position of the outcrops at craters 2 and 3 described in the text (B). Grain size distribution for proximal and mid-distal deposits (C). Stars in (A) show sampling site locations. Semi-log plot showing deposit thickness as a function of square root of isopach area (D).

### 3.4.2 Grain-size distribution and particle shape characterization

Grain-size distributions of the sedimentary succession and the hydrothermal explosion deposits were determined using dry sieving for the coarse fraction (>250 μm), and laser refraction technique using a Coulter LS230 (measuring range 0.375-2000 μm), for the fine fractions (<250 μm).

The coarser component of the sedimentary succession includes poorly sorted material with a polymodal distribution and maximum peaks around 4 and 8 mm; larger clasts in the succession represented a negligible percentage and were not considered. The clay-rich levels are better sorted with a modal peak between 250 and 100 μm (Figure 3.3, Figure 3.4).

Samples from proximal and distal deposits of the hydrothermal explosions exhibit different grain-size distributions reflecting two different inferred emplacement mechanisms (Figure 3.5). The very-poorly sorted proximal deposits show a polymodal distribution with the highest peak in the very coarse component (Figure 3.5C and Figure 3.6). Most of the material is in the ash to fine block range (<10 cm) and their distribution is used for the energy calculation. Several decimeter-sized lava blocks (up to 40 cm) are also present, but not included in the grain-size distribution as they represent a minor to negligible percentage of the overall deposit. In contrast, the mid-distal deposits are characterized by a more unimodal distribution with a peak around 180 mm (Figure 3.6).

A qualitative estimation of the amount of freshly-fragmented clasts in the ejected material was performed by using Scanning Electron Microscopy (SEM). SEM analysis shows the presence of non-juvenile particles only, characterized by a variety of surface morphologies and particle shapes. Four subgroups were identified, the first of which is composed of blocky lithic grains, with more or less equant shapes showing a variable proportion of vesicles, small microlites, signs of chemical pitting and strong hydrothermal alteration (Figure 3.7). Hydrothermal minerals clustered in a highly variant shape, from spherical to “agglutinate” in profile, form a second and predominant subgroup defined as aggregates (Figure 3.7C, E). SEM images that show particles in different stages of hydrothermal alterations indicate that the two further sub-populations exist: spherical amygdule vesicle-infillings and pure crystals (Figure 3.7 A,D,E). A minor but significant amount of fresh fracture surfaces were found on both, lithics and agglutinates. While it was beyond the scope of this study, a quantitative approach could be used to determine the proportion of different grain types.

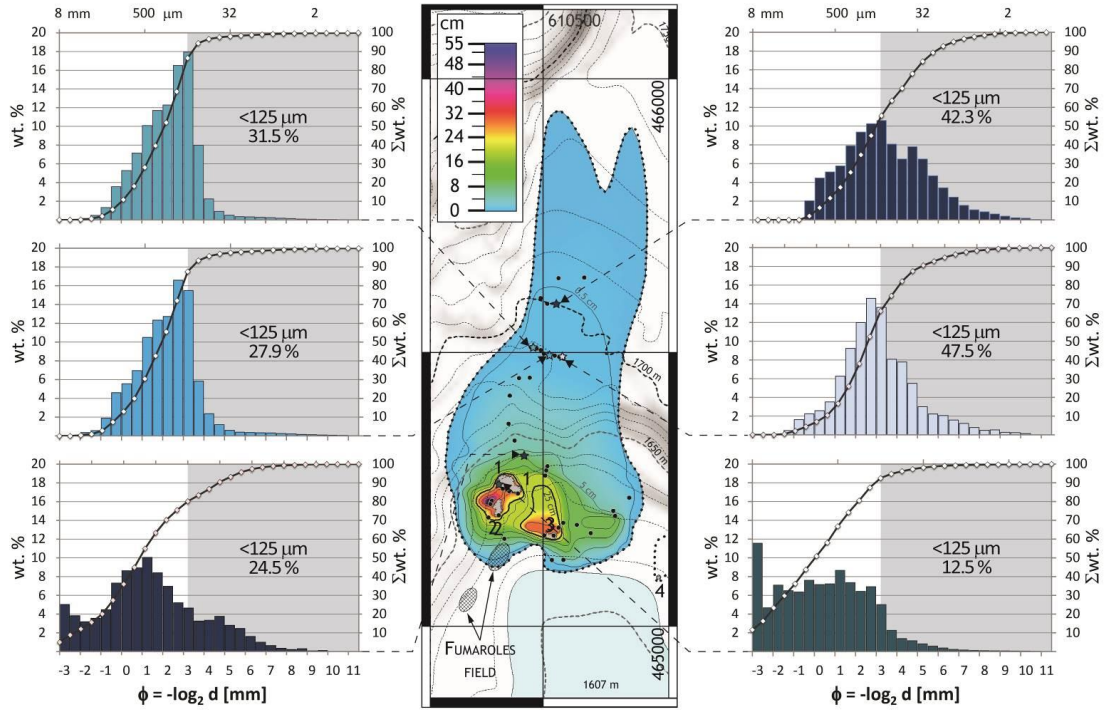


Figure 3.6 Grain size distribution of proximal, mid and distal deposit of the Gengissig hydrothermal explosions. Stars on the isopach map indicate samples location, where black dots indicate data points where thickness measurements were taken.

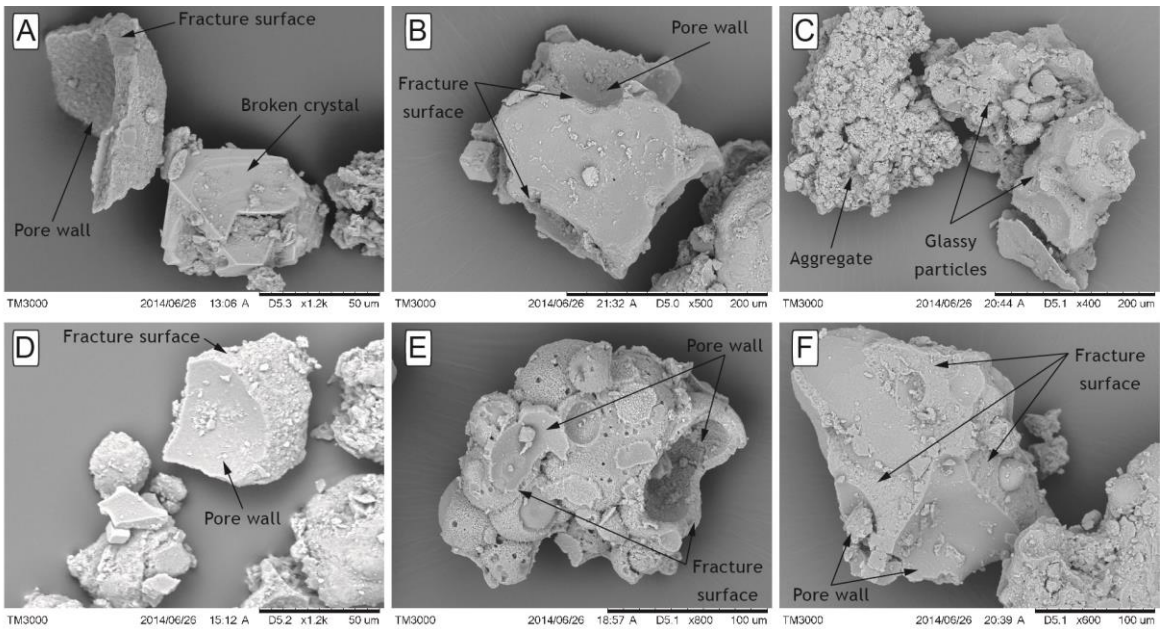


Figure 3.7 SEM images showing: crystal and glassy particle showing fresh fractures (A); glassy particle with fresh fractures (B); aggregate and glassy particle showing old fracture around pore wall (C); glassy particle showing fresh fractures around pore wall and secondary alteration minerals (D); alteration minerals aggregate with fractures around some of the pore walls (E); glassy particle with fresh showing fresh fracture around pore walls (F).

### 3.4.3 Deposit volume and mass

The volume of ejecta produced by the 16th August event was calculated using three different approaches. Firstly, the volume was determined by measuring the deposit thickness at various locations across and down the main northward-directed dispersal axis. Based on the direct integration of the isopach map (Figure 3.5 A, D), the minimum volume of the deposits is estimated to be approximately $6\times10^3$ m$^3$.

The second method; exponential decay of deposit thickness away from the craters (Pyle 1989) is approximated by a straight line on the semi-log plot of thickness vs. the square root of the area (Figure 3.5 D). The extrapolated $T_0$ (maximum thickness at area equal 0) and the rate of thinning measured by $b_t=\ln2/(k\times\pi^{1/2})$, where k is the line slope (Pyle 1989), were then used to calculate the volume:

$$V = T_0 \times 13.08 \times b_t^2 \qquad [3.1]$$

to yield a volume of $7\times10^3$ m$^3$.

A third estimation of the deposit volume was obtained according to the method of Sato and Taniguchi (1997), which is based on the relationship between crater diameter (R) and ejecta volume (V):

$$R = 0.97 \times V^{0.36} \qquad [3.2]$$

This relationship was used to estimate the volume for each recognized crater and yields $8\times10^3$ m$^3$ (Table 3.1).

That all three volume estimates are quite consistent, probably reflects the fact that 1) most of the ejected material was deposited ballistically around the craters with little effect of wind dispersion (Pyle 1989), and 2) the models yield better results with shallow events (Sato and Taniguchi 1997; Goto et al. 2001). Assuming a field-measured bulk density of the ejected material of 1.1 g/cm$^3$, the calculated mass is thus c.$7.3\pm1\times10^6$ kg.

Table 3.1 Deposit volume, craters size data, and energy estimations

| Crater | $D_{mean}$ [m] | Vol [m$^3$] | Err [m$^3$] | Foc. Depth [m] | Err [m] | $E_{Th}$ [J] | Err [J] | $E_{Crat}$* [J] | Err [J] | $E_{Kin}$# [J] | Err [J] |
|---|---|---|---|---|---|---|---|---|---|---|---|
| 1 A | 20,2 | 4600 | 684 | 21,5 | 3 | $1\times10^{11}$ | $1.5\times10^{10}$ | $3\times10^{10}$ | $5\times10^9$ | $9\times10^9$ | $2\times10^9$ |
| 1 B | 13,3 | 1430 | -195 | 15,5 | -2 | $3\times10^{10}$ | $4\times10^9$ | $9\times10^9$ | $1\times10^9$ | $3\times10^9$ | $7\times10^8$ |
| 2 A | 12,4 | 1180 | -199 | 14,7 | -2,5 | $2.4\times10^{10}$ | $4.5\times10^9$ | $7\times10^9$ | $1\times10^9$ | $2.4\times10^9$ | $5\times10^8$ |
| 2 B | 10,6 | 765 | -70 | 11,2 | -1 | $1.6\times10^{10}$ | $1.6\times10^9$ | $4\times10^9$ | $4\times10^8$ | $1.9\times10^9$ | $4\times10^8$ |
| 3 A | 8 | 350 | / | 20,9 | / | $8\times10^9$ | / | $2\times10^9$ | / | $7\times10^8$ | $1\times10^8$ |
| 3 B | 9 | 485 | / | 23 | / | $9.9\times10^9$ | / | $3\times10^9$ | / | $9\times10^8$ | $2\times10^8$ |

* The $E_{Crat}$ has been calculated based on the method of Goto et al. (2001).

\# The $E_{kin}$ represent an average of two values measured considering an initial ejection velocity of 40 and 50 m, respectively.

## 3.5 Seismic studies

Seismic monitoring of the Kverkfjöll caldera and other volcanoes in Iceland is operated by the Icelandic Meteorological Office (IMO). The network consists of mostly short period (Lennartz 5s) stations, but in the Vatnajökull area several broad band stations are present

(TRC20 20s, Guralp 30s, 60s and 120s). Real-time events recorded at the stations are automatically located and their magnitude is estimated within minutes of their occurrence. In August 2013 the closest station was at 19 km distance from Kverkfjöll, with 10 additional stations within 64 km (Figure 3.8A). An explosion event was recorded on 16th August at 10 stations, very emergent and well above noise level (Figure 3.8B). The signal appeared as a short tremor burst and therefore difficult to locate. An approximate location of roughly 2 km northeast of the explosion craters was obtained from the first arrivals at the three closest stations (kre, dyn, mko). The onset of the event was approximately 00:46:57. A continuous seismic trace from noon on the 14th of August at the closest station (kre) shows no other event of comparable amplitude that is not a confirmed earthquake elsewhere. The timing of the seismic signals and the observations at the glacier margin mentioned earlier, suggest that most of the water had already drained from the lake in the early hours of the 16th and that maximum flow occurred at the glacier edge during the night.

Characteristics of the signal from the closest seismic station (kre) indicate a duration of 40-50 s (spectrogram in Figure 3.8C). Possibly smaller events, of shorter (10 s) duration, followed for another 1.5 minutes. Therefore most of the energy appears to be released in the first explosion. Amplitudes are too small to be seen above the micro-seismic noise, so the signals are only observed at frequencies higher than 0.5 Hz. Most of that energy is concentrated between 0.5 and 2.5 Hz, but frequencies of up to 4 Hz are observed. Tremor bursts in his frequency range are commonly observed on the seismic network during subglacial floods, reflecting the low-frequency source and the dominance of surface waves due to the shallow source depth (Vogfjörd, K.C. et al. 2013). The smaller events are poorer in lower frequencies and peak around 2.1 Hz. A faint tail of elevated tremor, possibly reflecting vigorous boiling following the explosions, is observed for several minutes following the initial energetic events.

Peak ground velocities (PGV) and their decay with distance is shown in Figure 3.8D together with the noise level for comparison. To estimate the seismic moment ($M_0$) for the event, the peak amplitudes were fitted to an attenuation relation between PGV and moment magnitude ($M_W$) derived for earthquakes in Iceland (Pétursson and Vogfjor 2009). The median of the moment magnitude estimates from each station indicates a $M_W$ =1 and seismic moment $M_0 = 4\times10^{10}$ Nm. However, considering that similar magnitude and shallow earthquake sources located at Kverkfjöll are usually only 10-15 s long at station kre, while the event is of 40-50 s duration, the cumulative seismic moment for the event is estimated to be $4 \times M_0 \sim 1.6\times10^{11}$ Nm.

Estimation of seismic energy ($E_S$) radiated by the explosion was obtained using a relation between the seismic moment and energy, $E_S = M_0 \times 10^{-4.8}$ (Choy and Boatwright 1995). The relationship holds for many orders of magnitudes, different data sets and different regions, revealing a large spread in the data around the regression fit (Choy and Boatwright 1995; Choy et al. 2006), and representing a rough estimate of the energy. By assuming $E_S/M_0 \sim 10^{-6}$-$10^{-4}$, and considering that the event is dominated by low frequencies, the radiated energy is expected to be on the lower end of the range, giving the estimate $E_S \sim 10^6$ J.

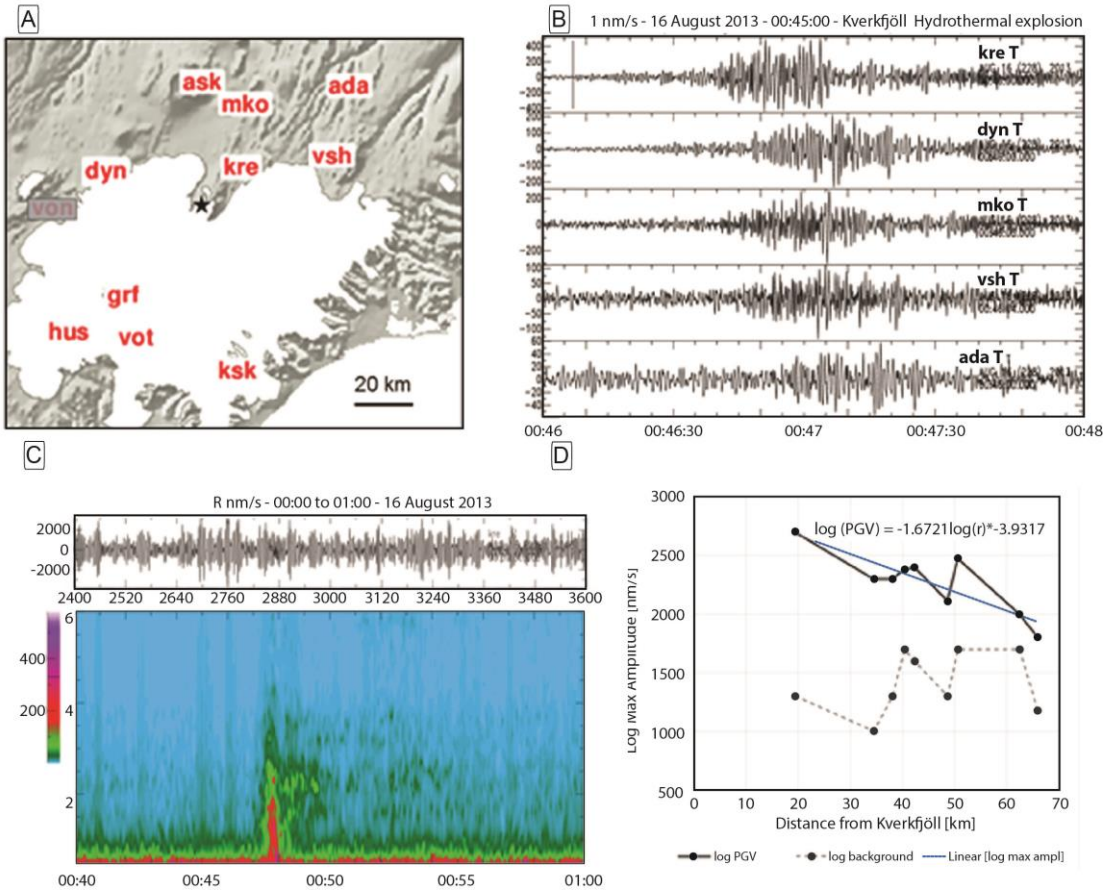


Figure 3.8 Map of Vatnajökull ice cap and Kverkfjöll (star) showing the location of seismic stations recording the Kverkfjöll hydrothermal explosion (A). Two minutes of seismic records of radial component from 5 stations located at increasing distances from Kverkfjöll (from 19 to 64 km). Amplitudes are in nm/s and the data has been band-pass filtered between 1 and 7 Hz (B). Twenty-minute-long, unfiltered tangential component seismogram from station kre, at 19 km distance from Kverkfjöll and its amplitude spectrogram, showing frequencies between 0.5 and 6 Hz. The figure shows the duration of the main explosion and the frequency content between 0.5 and 4 Hz. Below 0.5 Hz the signal is lost in the microseismic noise which dominates the seismogram (C). Decay of peak ground velocity with distance from Kverkfjöll (solid black) and noise (dashed grey). The best fitting line matches the linear part of the attenuation relation (Pétursson and Vogfjor 2009; D).

## 3.6 Laboratory studies

The permeability of samples taken during the field campaigns was analysed, with special focus towards the clay-rich levels observed in the successions (Figure 3.2Figure 3.3Figure 3.4). Additionally, a scenario considering if these clay levels are likely to act as capping layers to area below, enhancing the pressure build-up during the explosions, was explored. Further, decompression experiments mimicking the conditions created during lake drainage were conducted to investigate the ejection dynamics as well as potential changes in the grain-size of the ejected particles due to fragmentation and compared the results with field-based information.

### 3.6.1 Permeability measurements

Water permeability measurements were conducted in a steady-state permeameter. The unconsolidated samples were placed in a stiff rubber jacket, carefully saturated with water and compacted under a uniaxial pressure of 0.3 MPa, corresponding to the in-situ pressure before the lake drainage. This procedure resulted in fragile but coherent cylindrical samples with a diameter of 20 mm and lengths ranging from 30 to 40 mm. The fluid volume flux was measured during steady state flow at a confining pressure of 0.3 MPa and four different water differential pressures ranging from 0.02 to 0.1 MPa. Permeability was derived from the flux measurements by using Darcy's law (de Marsily 1986).

Two partially-altered clay-rich samples collected from 10 to 15 cm thick layers at the crater 2 and 3 (Figure 3.2, Figure 3.3, Figure 3.4, Figure 3.5), and one relatively unaltered sample close to the rim of crater 3 were investigated. The sample from crater 2 shows a bluish, clay-rich component in the lower part of the level, and a more sandy-rich portion in the upper part. The clay sample from crater 3 is less enriched in sand than the sample from crater 2. The third sample however, consists mainly of clay and is more homogeneous than the other two samples. From each of these, three sub-samples were analysed for permeability in order to check the repeatability of the obtained values (Table 3.2). Permeability values of $2.3\times10^{-14}$ $m^2$ and $3.8\times10^{-15}$ $m^2$ were obtained for the sand-enriched clay levels, sampled at crater 2 and 3, respectively. The homogeneous clay-rich sample has a lower permeability of $1.2\times10^{-17}$ $m^2$, due to its high clay content.

To explore the capability of these different clay level to act as barrier enhancing the pressure build-up, the following assumptions were consider: 1) the lake drainage caused a pressure decrease on the lake bottom sediments of approximately 2 bars (ca.20 m of water column above the crater area; see section 3.4.1); 2) the decompression triggered the boiling of the fluids within the lake sediments (see section 3.7); 3) the time needed to release the boiling vapor pressure through these clay-rich levels is controlled by their permeability and thickness, according to a simple Darcian up-flow (de Marsily 1986). Thus the calculated flowing time through the sand-enriched levels ranges between 2 and 3 hours using the first permeability value reported above, and between 11 and 16 hours using the second value. However, the permeability value for the clay-rich level equates to a drainage time ranging between 150 and 200 days. Accordingly, and considering the lake drainage duration (10-15 hours), it can be speculated that the clay-rich levels (including those slightly enriched in sand) likely acted as a barrier to fluid flow prior and/or during the hydrothermal explosions due to their significantly longer flowing time.

Table 3.2 Permeability measurements

| Sample | $k1$ [$m^2$] | $k2$ [$m^2$] | $k3$ [$m^2$] | $k_{avg}$ [$m^2$] | $\Sigma_{DEV}$ [$m^2$] |
|---|---|---|---|---|---|
| KVF_C2_L2 | $3.7 \times 10^{-14}$ | $1.54 \times 10^{-14}$ | $1.72 \times 10^{-14}$ | **$2.32 \times 10^{-14}$** | $1.2 \times 10^{-14}$ |
| KVF_C3_L2 | $3.52 \times 10^{-15}$ | $5.95 \times 10^{-15}$ | $1.89 \times 10^{-15}$ | **$3.79 \times 10^{-15}$** | $2 \times 10^{-15}$ |
| KVF_outside C3 | $8.83 \times 10^{-18}$ | $1.34 \times 10^{-17}$ | $1.3 \times 10^{-17}$ | **$1.17 \times 10^{-17}$** | $2.5 \times 10^{-18}$ |

### 3.6.2 Decompression experiments

#### 3.6.2.1 Methods

A series of rapid decompression experiments on particle–water mixtures have been carried out by using the shock-tube apparatus and the methodology described in sec. 2.5. These experiments were performed to qualitatively investigate the role of the loose nature of the material involved on the fragmentation and ejection dynamics of explosions. The aim was to investigate a possible change in grain-size distribution of pre-sieved material, and to measure the velocities of ejected particles.

The pre-sieved unconsolidated material from the Gengissig sedimentary succession that served as sample material included all the main components, from lava and scoriaceous clasts to aggregates. Different combinations of grain-sizes were used to investigate the effect on fragmentation and ejection behavior (Table 3.3 and Figure 3.10A).

Table 3.3 Experimental samples description

| Crater | Grain size used | Initial mass [g] | Water added [g] | Porosity |
|---|---|---|---|---|
| KVF_C3_L3 | ϕ= 8-2 | 63.30 | 35 | 55 |
| KVF_C2_L3 | ϕ= 2,8-1,4 | 52.09 | 39 | 60 |
| KVF_C2_L4 | ϕ= 2,8-1 | 49.78 | 36 | 57 |
| KVF_C2_L3 _(clay x2*) | ϕ= 5,6-1 | 79.725 | 21 | 33 |
| KVF_NC2_1_(clay x1*) | ϕ= 5,6-<0,5 | 62.5548 | 21 | 33 |

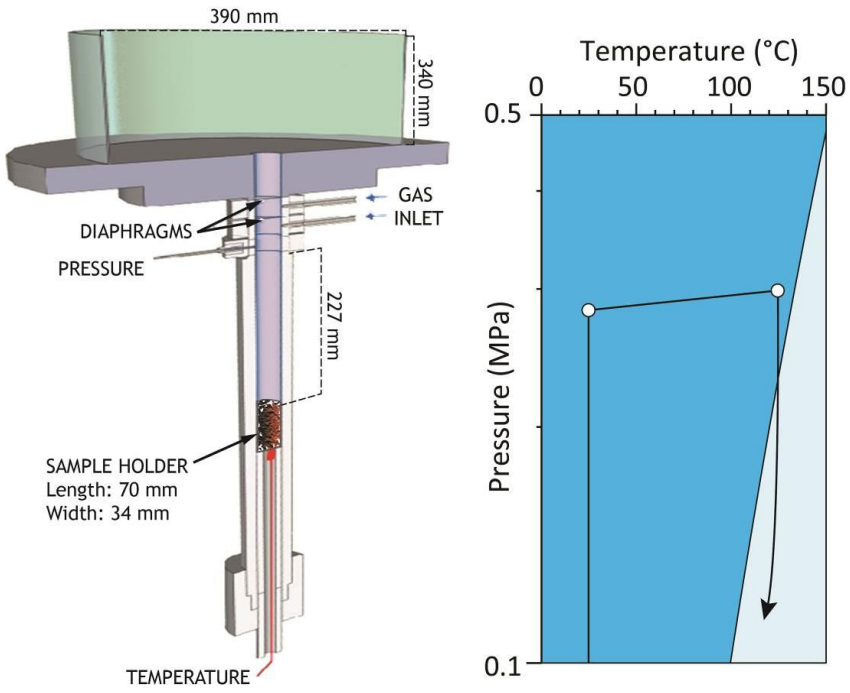


Figure 3.9 Sketch of the fragmentation apparatus, and water phase diagram showing the experimental path followed during each experiment. Sample were pressurized up to approximately 0.2 MPa, then heated at 15°C/ min. A final pressure of 0.3 MPa was obtained at the end. The overall pressurization, heating and dwelling process lasted for 20-30 minutes.

Cylindrical steel crucibles (34 mm in diameter and 70 mm long) were completely filled with particles of known grain-size. Gentle tapping of the particle-filled crucible ensured comparable conditions in terms of particles amount and porosity for different experiments. Using the weight of the particles and the volume of the crucibles, porosity could be estimated (Table 3.3). A fairly high bulk porosity was obtained due to the use of mainly coarse material, but these conditions were in line with the experiment purpose. After placement in the crucible the samples were placed in water and kept in a moderate vacuum to assure a complete saturation of the porous particles.

The pressure and temperature conditions used in this study represent those of the decompression following the Gengissig drainage. The water height at the craters area dropped ca.20 m, corresponding to a pressure drop of approximately 0.2 MPa. The water temperature at the lake bottom can be assumed to corresponds to the boiling temperature under pressure prior to drainage (~0.3MPa), which is 133.5°C (see section 3.7). The decompression results in the explosive boiling of the water (and so the steam formation), which is driving the explosion and is the same process invoked for the Gengissig case. During experiments the entire pressurization, heating and dwelling process lasted 20-30 minutes, ensuring the samples reached thermal equilibrium (Figure 3.9).

#### *3.6.2.2* Results

The grain-size distribution of the recovered material was analysed and compared to that prior to the experiment. All grain-size distributions of the ejected samples exhibit an increased weight fraction of ash-sized particles (Figure 3.10). This may be an indication of fragmentation as well as other size-reducing processes such as disintegration of aggregates.

A qualitative morphological analysis was performed on the 180 -250 μm fraction of two samples, which contained most of the freshly-fragmented material (Figure 3.10). In this grain-size fraction only minor evidence was found for freshly-formed fractures, possibly due to the lack of fracturing occurring in that grain-size fraction, or due to the lack of fresh material in which fractures could be recognized. Analogous to the analyzed particles from the hydrothermal explosion deposits, most clasts consist of aggregates (Figure 3.10B, D). These are usually composed either by fragments of crystals and glassy parts in a matrix of alteration minerals, or by clusters of alteration minerals only (Figure 3.10A, D). The remaining particles in that size range are mainly glass fragments covered by a blanket of micron or sub-micron sized alteration minerals (Figure 3.10C).

The ejection velocity of the gas-particle mixture was obtained from high-speed video recordings of each experiment. Results showed in Figure 3.11 indicate that the clasts were ejected with velocities of up to 100 m/s. In all the experiments for particles smaller than 1 mm the initial ejection speed is of 60-100 m/s, whereas the first larger particles (>1mm) are ejected later and show a velocity range of 40-50 m/s.

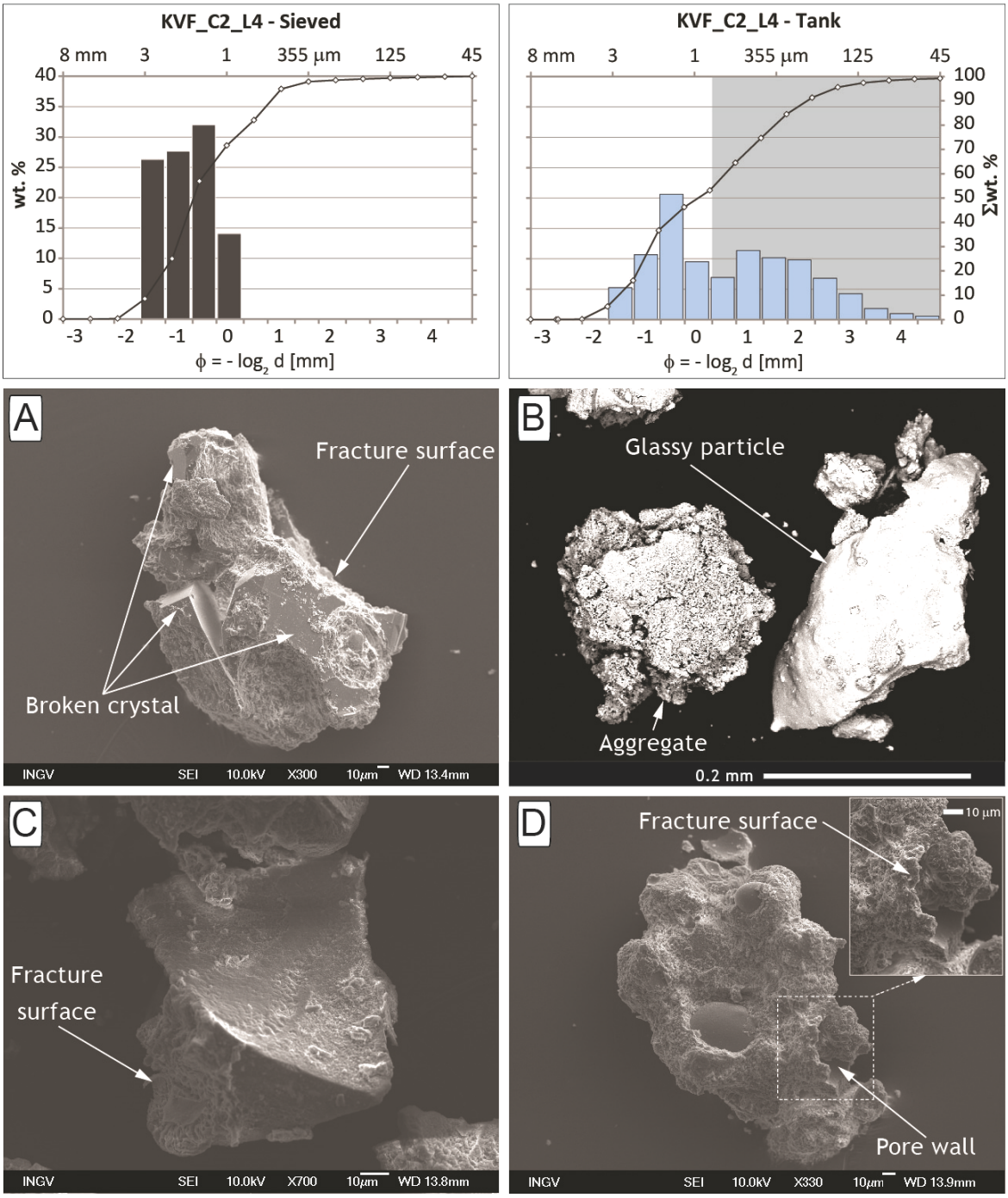


Figure 3.10 Above: grain size distribution of pre-selected loose material, before and after decompression experiments. The shaded area highlights the size distribution of the newly formed particles, which show a peak around 355 µm. Below: field emission scanning electron microscopy (FESEM) images showing: broken crystals in a matrix of alteration minerals showing fresh fractures (A); aggregates and glass particle (B); altered blocky shaped glass fragment showing fresh fractures (C); alteration minerals aggregate with fresh fractures around some of the pore walls (D).

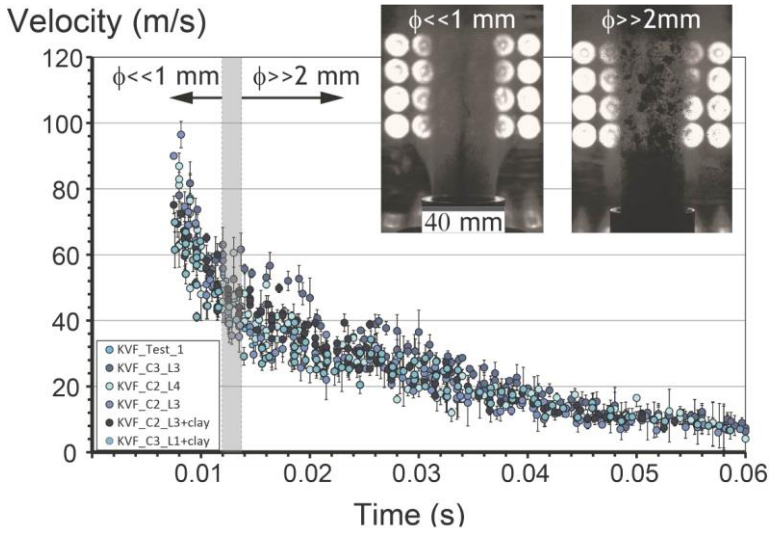


Figure 3.11 Ejection velocities of particles with time, measured using image analysis of high-speed camera footage. Within inlet the difference in the ejected particle size is shown.

## 3.7 Energy considerations

Estimates of the energy associated with these hydrothermal explosions includes the mechanical energy required to produce the observed cratering and ejecta, balanced with the energy available for the explosive processes (Figure 3.12). Here thermal energy is used as equivalent to the available explosive energy ($E_{Expl}$ in Sec.2.4).

The calculation of available energy is based on the thermodynamic change of the geothermal system before and after drainage pressure failure (Muffler et al. 1971; Mastin 1995). The estimated energy is approximate as the rock properties prior to the explosion and the depth of the craters are imperfectly known. Additionally the irregular crater shape, assumed here to be circular/elliptical, and errors in the deposit volume calculations (Table 3.1), add a certain degree of uncertainty to the estimation. For each observed crater a conical vent has been assumed. The diameter and estimated volume was used to calculate the focal depth of the explosion (or the deepest level from which rock material was removed) defined as the tip of the downwards pointing cone. The estimated depths range between 11 and 23 m (Table 3.1).

As described in section 3.4 these explosions were triggered by a decrease in confining pressure as a consequence of Gengissig lake drainage (1637 to 1607 m a.s.l. in ca. 10-15 hours; Figure 3.13A). The pressure failure caused boiling in the surficial geothermal reservoir and thereby explosions (Figure 3.13B-D). The area where the explosions developed was roughly ca.20 m below the lake level. A maximum drainage of 30 m was instead reached in the deepest, southern part of the Gengissig lake (Figure 3.1 and Figure 3.13A).

The drainage of the glacially-dammed lake reduced the effective confining pressure on the sub-lacustrine hot-spring system (corresponding to the craters area as mapped from the field; see section 3.4.1) by the equivalent of a ca.20 m water column (approximately 0.2 MPa), and the controlling boiling point curve became relative to a free-water level at 1617

m a.s.l. Here, the declining water level results in higher steam pressures developing close to the ground surface as boiling conditions descend deeper into the reservoir (Muffler et al. 1971; Browne and Lawless 2001). The temperature of the lake bed at points of thermal up-flow is assumed to be 133.5°C. Similarly, at a depth of 25 m, slightly below the maximum focal depth, it is assumed to be 155.5°C. Parts of the affected system may not have been at maximum permissible temperatures, and so the average initial temperature is conservatively assumed to be 144.5°C (Figure 3.13C). Thus the hydrothermal explosion process assumes water at an initial temperature of 144.5°C and pressure of 0.3 MPa which flashes to steam, cooling to approximately 94.87°C (the boiling point of water at 1617 m a.s.l.). At the same time, additional heat is transferred from rock debris to the water, causing further steam production. Therefore, assuming an isolated system, a reservoir pore volume of 28% (averaged value for sand-gravel mixed deposits), a heat of vaporization for water of $2.26\times10^6$ J/kg, and an isenthalpic and irreversible depressurization, the energy available for craterization and ejection is (Muffler et al. 1971):

$$\Delta E_{Th} = m_r\times c_r\times\Delta t + x\times m_w\times(U^{t1}_{water} - U^{t2}_{steam}) + (1-x)\times m_w\times(U^{t1}_{water} - U^{t2}_{water}) \quad [3.3]$$

$x$ = steam fraction (calculated by using: $\Delta t\times(m_w\times c_w + m_r\times c_r)=x\times m_w\times L$)
$m_r$-$m_w$ = rock-water mass (kg);
$c_r$ = rock specific heat of 900 J/kg×°C (assuming an average lava composition);
$U^{t1-t2}$ = internal energy before and after explosions.

Thus a thermal energy ranging between $7\times10^9$ J and $1\times10^{11}$ J is estimated for the different craters (Figure 3.12A and Table 3.1).

Craterization energy is assessed using the cube-root similarity rule of explosion dimensions (Nordyke 1962; Sato and Taniguchi 1997; Goto et al. 2001). This method, which assumes a scaling relationship between the craters formed by individual explosions and explosive energy and depth, has been proved to be valid on a wide range of scale and holds well for surficial explosions (Lee and Mazzola 1989; Sato and Taniguchi 1997 and reference therein). Valentine et al. (2012) point out that final crater size is not a good indicator of the energy of individual explosions, especially for large scale maar-like events, since the final size is the result of multiple explosions in the subsurface and collapses of the crater rim. However, good agreement is shown between the energy-crater size ratio of the studied hydrothermal explosions, and that of field-based explosion experiments performed in loose material (Goto et al. 2001; Taddeucci et al. 2013; Graettinger et al. 2014). It is here suggested that the similarity rule is applicable to this case because of the loose nature of the material involved and the shallow depths of explosion. Furthermore in-situ observation of the fresh morphology soon after the event suggest that little changes in the crater rim shape occurred.

Therefore, to calculate the energy the similarity rule established by Goto et al. (2001) is used as:

$$\log D = 0.32\times\log E_{Crat} - 2.06 \quad [3.4]$$

The results for the observed crater diameters (D) indicate an energy ($E_{Crat}$) ranging approximately from $2\times10^9$ J and $3\times10^{10}$ J (Table 3.1).

The kinetic energy required to transport ejecta was also assessed. With a well-constrained mass (m) of the ejected material, and neglecting the energy dissipated in the accompanying seismic wave and air blast, the kinetic energy of the ejected projectiles can be calculated using:

$$E_{kin}=1/2\times m\times v^2 \qquad [5]$$

Based on the distribution of the ballistically ejected material (<10 cm in size and deposited within a range of 50 to100 m from the craters), and optimum angles of 70-85°, this yields an initial velocity (v) varying between 40 - 50 m/s assuming zero drag (Fagents and Wilson, 1993). By using the field-measured density (1.1 g/cm$^3$) and the calculated volume at each crater an energy range between $7\times10^8$ and $9\times10^9$ J is estimated (Table 3.1).

Finally, the energy conversion ratio (hereafter ECR: the ratio of the mechanical energy to the thermal energy) is evaluated, representing is an important parameter to define how efficiently the available energy budget is partitioned. Figure 3.12B shows both the ratio of craterization and kinetic energy over thermal energy plotted against ejecta volume. The ECR of thermal to craterization energy ranges from ca.23-30% whereas the kinetic energy associated with the transport of ejected material is on the order of ca.8.5-12%.

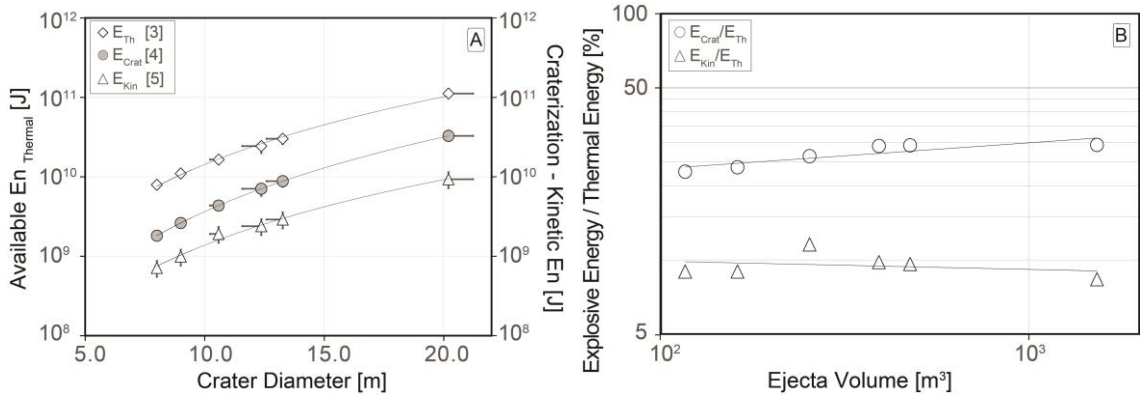


Figure 3.12 semi-log plot showing thermal ($E_{Th}$), craterization ($E_{Crat}$) and kinetic ($E_{Kin}$) energy VS crater size (A). Log-log plot showing the ratio of craterization and kinetic energy to thermal energy (B).

## 3.8 Discussion

### 3.8.1 Explosion mechanism and dynamic

The drainage of Gengissig lake on 15th to 16th of August 2013 caused a decrease in confining pressure beneath the lake bed (4-8 Pa/s), which triggered rapid boiling in the surficial geothermal reservoir (Figure 3.13A-C), and lead to several hydrothermal explosions through coarse unconsolidated sediments interbedded with clay or clay-rich layers (seen in crater successions). As permeability in unconsolidated clastic sediments is known to scale with grain size, it can be assumed that the coarse (sand to gravel) sections

are sufficiently permeable to dissipate the pressure perturbation caused by the lake drainage. In contrast, permeability measurements of the clay-rich layers resulted in low to very low values ($1.2\times10^{-17}$m²), which excludes dissipation of the pressure over the time of lake drainage and suggests that clay-rich layers can have acted as capping layers in the Gengissig hydrothermal explosions. Explosions are triggered if the residual pressure developed below such a layer is sufficient to cause the failure of the capping clay level, and results in a sudden pressure drop below them (Figure 3.13).

However, as the clay layers are only 0.15-0.2 m thick and interbedded in coarse unconsolidated sediments, it can be expected them to behave in a weak manner. When failure occurs, the generated boiling-front penetrates downwards into the geothermal reservoir, followed by the explosion front (McKibbin et al. 2009), where the steam expands, fragmenting and dispersing the surrounding material (Figure 3.13C-D). Explosion continues until the rate of groundwater boiling decreases and steam expansion ceases to provide sufficient energy to eject rocks from the crater (Figure 3.13D). The explosions at Gengissig occurred on the north-western side of the lake, where the presence of fumarole systems and boiling pools indicate a local high heat flow. Besides favoring pressurization, the low-permeable clay level might helped maintaining liquids at boiling conditions during the decompression phase by hindering the migration of cold fluids into the explosion sites.

Based on the debris distribution, and assuming the downward migration of the explosive process, it can be speculated that an initial shallow phase of the explosion produced a funnel-shaped cloud with clasts ejected at a low angle. This may have evolved into a more elongated fan with a higher ejection angle as the focal depth of explosion deepened Figure 3.13C-D). The ejection dynamics inferred here are based on similarities with the jet shape produced during natural eruptions (Yokoo et al. 2002), and on field-based explosion experiments using loose material at varying shallow depths (Goto et al. 2001; Valentine et al. 2012; Taddeucci et al. 2013; Graettinger et al. 2014).

Seismic data indicate that the explosive activity lasted approximately 40-50 s. Assuming that many short-time scale explosions occurred, of which the most intense shaped the final crater size (Goto et al. 2001), a sufficient resolution to constrain the duration of explosions at each crater (at least 9) its lacking. Thus the continuous signals recorded indicate that the explosive events may have occurred sequentially or with a very short interval, possibly of seconds, at the different craters.

Results from decompression experiments indicate the production of “fresh” fine particles. Comparison of the morphology of the newly-formed material with the pristine component would suggest that the majority of the fresh fragments derive from dismembered aggregates. Furthermore, the ejection velocities of the particles obtained experimentally yield good agreement with the velocities estimated from field data. The very fine material is ejected at higher velocities (100 m/s) compared to the lapilli-sized clasts (<2mm). The two velocity regimes fit well with the proposed scenario and can explain the different ejection modes inferred from the deposits. Thus the fine particles are ejected at higher elevation and caught by the wind, whereas the coarse material is emplaced ballistically around the crater area.

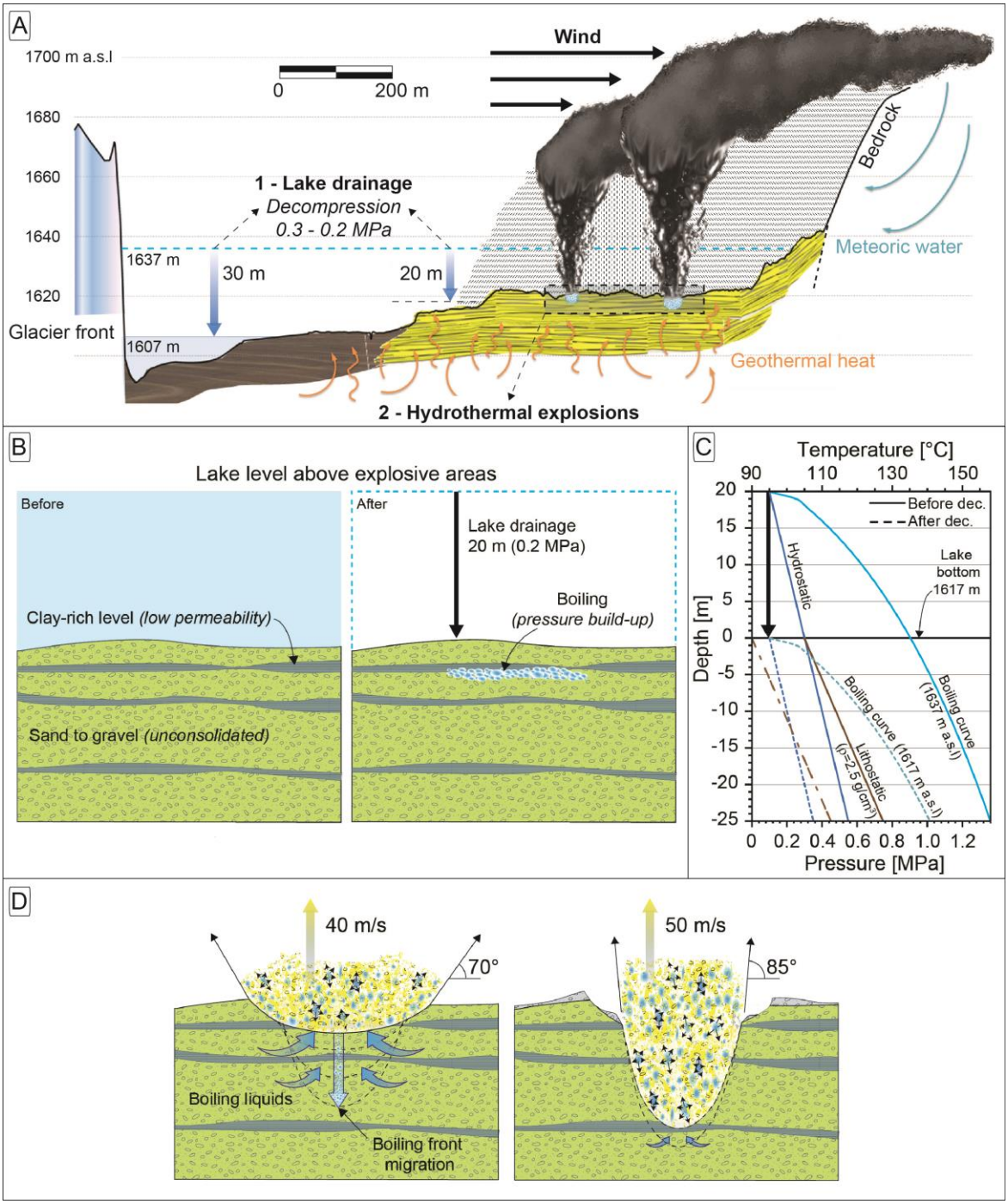


Figure 3.13 Sketch showing the setting before and after the lake drainage. Profile across Gengissig, based on kinematic GPS collected 12 days after the explosions (A). (B-D) Conceptual model of the hydrothermal explosions evolution: lake drainage (pressure failure) and boiling initiation (B); hydrostatic, lithostatic and boiling point temperature before and after lake drainage (C); explosion caused by clay layer failure and subsequent pressure release and progressive downwards propagation of boiling front. See text for more explanation (D).

### 3.8.2 Energy budget and partitioning

The assessed thermal energy available in the hydrothermal system at Gengissig is in the order of $10^{11}$J, consistent with the estimates made for similar-sized (i.e. crater size, deposit area and estimated volumes) events in Yellowstone (Muffler et al. 1971; Morgan et al. 2009). The energy required to excavate the ejected material (approx. $10^4$ $m^3$) at Gengissig has been estimated to be approximately 5.9 J/$cm^3$ (ECR of ca.30%). This value fits well with the range of 3 to 15 J/$cm^3$ estimated from field-based explosion experiments performed in loose material (ECR between 30 and 70%; Valentine et al. 2012; Graettinger et al. 2014), and also with the value of 8.4 J/$cm^3$ (ECR of ca.40%) estimated by Muffler et al. (1971). The ECR from thermal to kinetic energy, assessed for comparable hydrothermal eruptions occurring in cemented, mostly consolidated or highly fractured rocks, ranges between 0.1 and 6% (Browne and Lawless 2001). However, a values of ECR between 8.5 and 12%for the Gengissig hydrothermal explosions can be estimated (Figure 3.12B). This highly efficient conversion can be related to the loose nature of the sedimentary material involved, as the energy partitioning into fragmentation and viscoelastic deformation depends strongly on media properties (Murphey and Vortman 1961; Goto et al. 2001; Ohba et al. 2002; Valentine et al. 2012). Thus, most of the mechanical energy has been used in the erosive process of craterization and ejection of material, with only a minor (not quantifiable) amount consumed in fragmentation, as inferred from the particles morphology. A very small portion (ECR<<0.01%) is converted into seismic energy, while the remaining energy was dissipated as heat, generating steaming over days and weeks following the explosions.

### 3.8.3 Broader implications

The study on the Gengissig explosions has broader implications in terms of hazard management in Iceland and understanding other similar events. In terms of hazard management, the seismic data recorded in this event provide insight into how similar events occurring in other remote, subglacial areas in Iceland might be detected. In cases where a subglacial jökulhlaup path is long, signals of this kind may occur before the onset of water drainage outside the glacier edge. This has practical implications for hazards, since the drainage of subglacial lakes has on several occasions caused damage to roads, bridges and other infrastructure in Iceland.

In terms of understanding other similar events better, it can be noted that in the case of Gengissig the occurrence of explosions during the re-equilibration of the geothermal system to lower pressure, and hence temperature, depended on (1) the timescale of this destabilization process, (2) presence of liquids close to the boiling point at sub-surface, and (3) existence, and variability (thickness and strength), of a near-surface low-permeable layer. These can be generally considered the main factors controlling the response of a reservoir to rapid decompression, which does not always result in an explosion.

## 3.9 Conclusions

The 16th August 2013 hydrothermal explosions at Gengissig lake were caused by a pressure failure that followed lake drainage. The approach used here to investigate hydrothermal explosions allowed us to constrain different aspects of these phenomena combining 1) field analyses, 2) seismic signals and 3) laboratory experiments. The detailed mapping of the deposits soon after their emplacement yields good estimations of the ejected mass and volume, which are also reasonably consistent to theoretical models, making the Gengissig explosions a rare example of small hydrothermal explosions where full characterization of the events is possible.

The comparison of the collected data with analytical modeling yields a robust constraint on the energies released by these small-size explosions. The characterization of the stratigraphic sequence involved in the explosions provided an opportunity to understand the effect of the host rock lithology, which here appear to control the explosion dynamics and energy partitioning.

Furthermore the seismic energy released in this well-constrained event may be used to detect similar hydrothermal explosions occurred in the past jökulhlaups. If validated, use of seismic data might provide a proxy for future events and used in hazard management.

This page was intentionally left blank.

# Chapter 4

# *Experimental estimates of the energy budget of hydrothermal eruptions; application to 2012 Upper Te Maari eruption, New Zealand*

*A brief vision he had of swirling cloud, and in the midst of it towers and battlements, tall as hills, founded upon a mighty mountain-throne above immeasurable pits; great courts and dungeons, eyeless prisons sheer as cliffs, and gaping gates of steel and adamant: and then all passed. Towers fell and mountains slid; walls crumbled and melted, crashing down; vast spires of smoke and spouting steams went billowing up, up, until they toppled like an overwhelming wave, and its wild crest curled and came foaming down upon the land. And then at last over the miles between there came a rumble, rising to a deafening crash and roar; the earth shook, the plain heaved and cracked, and Orodruin reeled. Fire belched from its riven summit. The skies burst into thunder seared with lightning. Down like lashing whips fell a torrent of black rain. And into the heart of the storm, with a cry that pierced all other sounds, tearing the clouds asunder, the Nazgûl came, shooting like flaming bolts, as caught in the fiery ruin of hill and sky they crackled, withered, and went out*

*"The destruction of Barad-dûr" in The Return of the King (1955)*
*Tolkien, J.R.R. (1954-55)*

## 4.1 Introduction

Hydrothermal eruptions are common in volcanic (and other) terrains where high heat-flow, combined with appropriate ground-water conditions, favors rapid generation of steam and fluid-pressure build-up (Browne and Lawless 2001). These events are particularly hazardous because they often occur with little or no warning (Barberi et al. 1992; Hurst et al. 2014). The 2014 eruption at Mt. Ontake in Japan resulted in 57 deaths (Kato et al., 2015; Yamamoto, 2014), while those at Ruapehu and Te Maari (Tongariro), in New Zealand were fatality-free due to their timing alone (Kilgour et al. 2010; Breard et al. 2015). Despite their small volumes, hydrothermal eruptions may be highly energetic and produce extended ash plumes, pyroclastic density currents and widespread ballistic events (Lube et al. 2014).

This study report a primarily experimental study designed to understand the relative importance of fluid factors (pressure-temperature conditions) with rock properties (porosity, and lithology) in controlling the properties of hydrothermal explosive eruptions. Experimental results were integrated with the field example of the August 2012 explosive

hydrothermal blast from the Upper Te Maari crater on the northern side of Mt. Tongariro, New Zealand (Figure 4.1). This event was triggered by a landslide from the western flank of the crater (Procter et al. 2014),and produced west- and eastward directed blasts, with high-energy ballistics and cold (<100 °C) surges (Lube et al. 2014). Breard et al. (2014) recognized that the eruption source area is characterized by beds of poorly sorted clay and ashy matrix diamictons, breccias and agglutinates that vary in porosity, grainsize, sorting, thickness, and degree of hydrothermal alteration. Using the westward directed blast as a comparison, the study aimed to elucidate: i) the effect of energy source and rock heterogeneity on the fragmentation behaviour, ii) the mechanism of ballistic ejection and iii) the partitioning of energy between fragmentation work and kinetic energy of ejecta. These results are important for understanding the explosive power of violent hydrothermal eruptions, and the associated ballistic hazards.

### 4.1.1 The 6th August 2012 Upper Te Maari crater eruption

On the night of 6th August 2012 a partial collapse occurred on the hydrothermally-altered western flank of the Te Maari crater (Tongariro Volcanic Center, New Zealand; Figure 4.1A). The collapse triggered the sudden decompression and fragmentation of the sealed, hot hydrothermal system below the crater (Pardo et al. 2014). A ~20-s-long series of four hydrothermal explosions occurred, producing a 430-m-long, up to 65-m-wide and 30-m-deep eruptive fissure, immediately south of Upper Te Maari crater. An eastward directed plume (at angles >45° to horizontal), followed by a low angle (<<45°) blast to the west were associated to the fissure explosions. A final central eruption from the Upper Te Maari crater produced a vertical ash column (Jolly et al. 2014; Lube et al. 2014). All explosions were accompanied by ballistic ejection, some of which impacted the Tongariro Alpine Crossing walkway (1.2 km from Upper Te Maari at its closest point) and the Ketetahi Hut (1.4 km from source; Breard et al., 2014; Fitzgerald et al., 2014). The absence of vegetation burned by ballistic clasts, and their country-rock origin indicates dominantly sub-incandescent temperatures, but molten sulphur bleeding from many rocks indicates they were <~120$^{o}$ C (Breard et al. 2014).

The total eruption energy was estimated at $2.1\times10^{13}$J by Lube et al. (2014) based on an empirical relationship between the crater size and explosive energy, although only $3\times10^{12}$J was estimated based on acoustic pressure data (Jolly et al., 2014). Four distinct pulses occurred within the initial 20 s of the eruption, each 3–5s-long (Jolly et al., 2014). Pressure difference/time show that pulse 3 was the largest, with ~50% of total energy release, while 1 and 4 each accounted for ~20%, and pulse 2 was only 5%. The third and most energetic pulse was attributed to the western-direct blast (Lube et al., 2014). Factoring the total volume of ballistics ejected, with a mean particle density, a total kinetic energy of $1.7\times10^{10}$J release was estimated by Fitzgerald et al. (2014) assuming initial particle velocities of 200 m/s. This equates to only <0.1% of the bulk explosion energy released during the eruption.

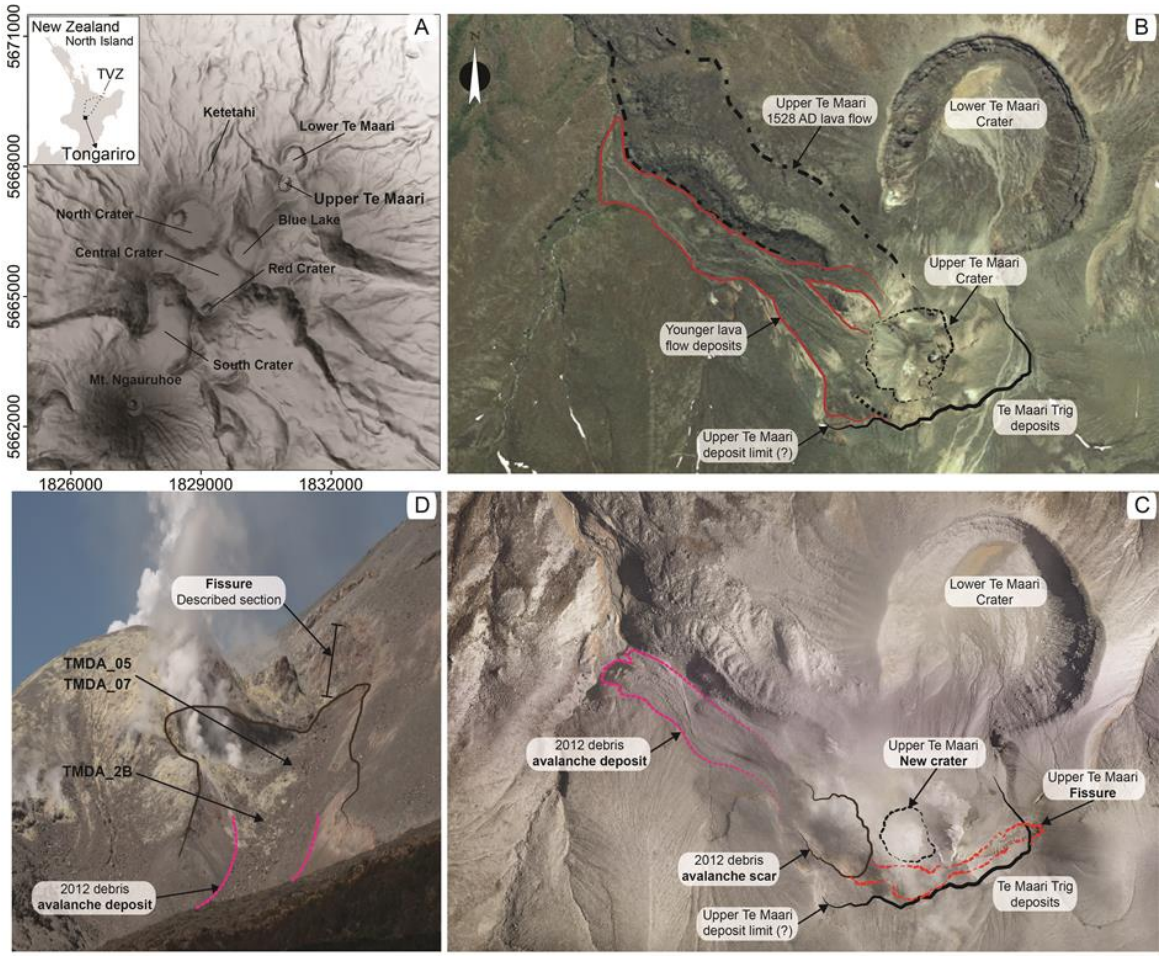


Figure 4.1 Shaded relief of the Tongariro Volcanic Centre (in the inlet TVZ: Taupo Volcanic Zone) with locations of the main eruptive centers, including the Upper Te Maari on the northern slope (A). Orthophoto of the Upper Te Maari cone before the eruption (B). View of the western fissure: delimitation of amphitheatre (dark brown line) created by the landslide (dashed pink line; see Procter et al.,2014), with location of the collected samples and of the fissure section described in the text (C). Post-eruption orthophoto of the Upper Te Maari fissure; new morphological elements as landslide scar (bark brown line) and deposit (dashed pink line) are reported (D).

### 4.1.2 Upper Te Maari hydrothermal system

At Upper Te Maari, magmatic steam mixed with circulating meteoric water at equilibrium temperatures of ~250–300 °C (Hochstein, 1985), are capped by a coherent,100–500m thick, condensate layer containing highly hydrothermally altered rocks with low-resistivity (Walsh et al. 1998). The temperature at the top of this layer is close to boiling. At the nearby Ketetahi, water chemistry indicates a separate, unconnected hydrothermal system, where the pressure (and temperature) increase linearly with depth, reaching >4 MPa at the bottom of the condensate layer (Figure 4.2; Walsh et al., 1998). Kaolin dominate the highly altered zones within the Upper Te Maari hydrothermal system, whereas gypsum and pyrite are more abundant in more coherent materials (Stewart et al., 2015).

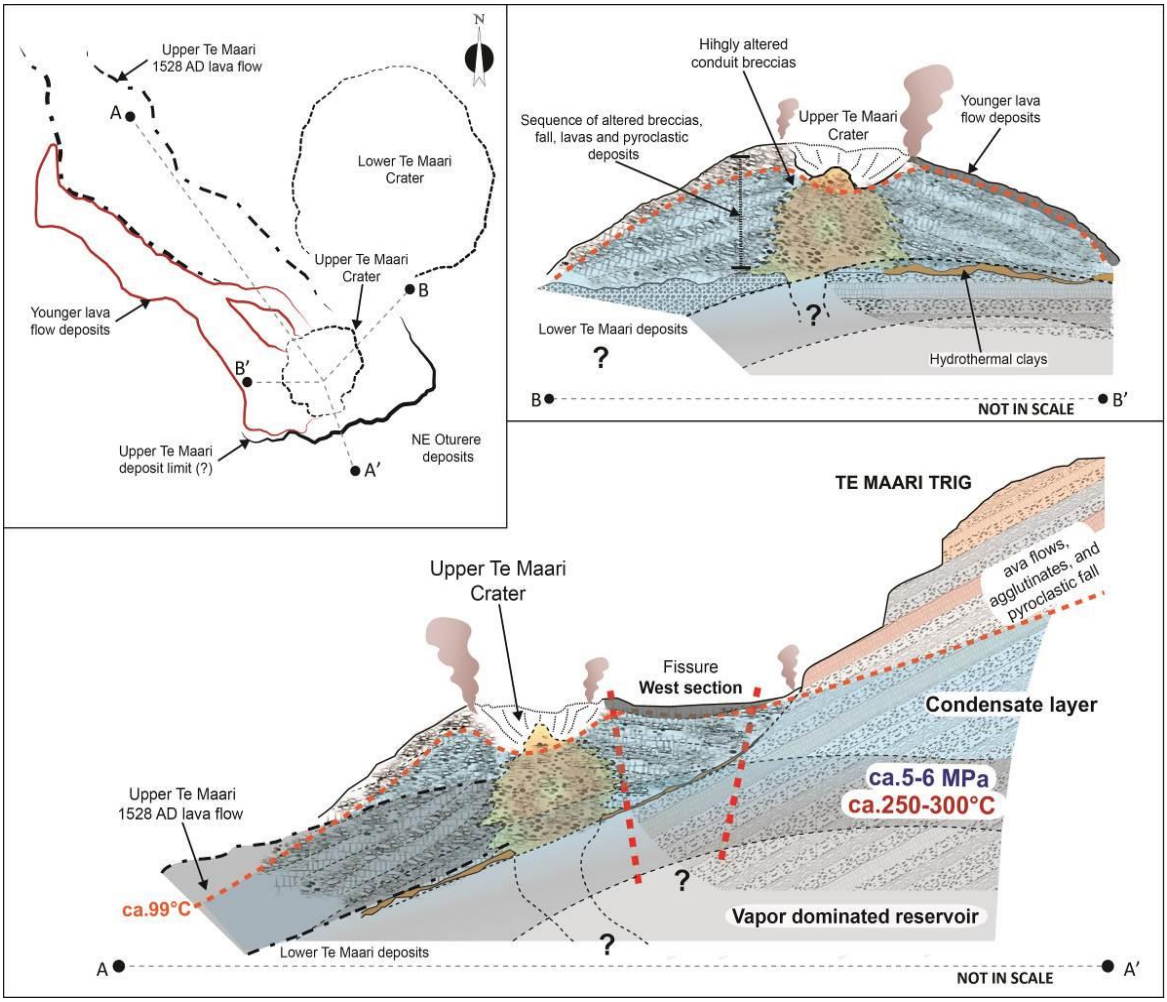


Figure 4.2 Conceptual sketch of the Upper Te Maari crater and its hydrothermal system prior to the eruption. In the top-left inlet a schematic map of the main morphological elements of the Upper Te Maari crater area. Both longitudinal (A-A') and cross (B-B') profiles are shown with the inferred condition for the hydrothermal system, as well as the geology, of the Upper Te Maari crater and the northern slopes of Te Maari Trig. Dashed red line indicate the approximate location of the western part of the eruptive fissure.

## 4.2 Field-based studies

Ballistic craters and ballistics were mapped along a WNW transect across the highest density part of the western ballistic strewn-field (Breard et al., 2014; Fitzgerald et al., 2014). The blocks were classified as: 1) high-density ($\rho_{avg}$=2.4 g/cm$^3$) massive andesitic lava with some partially coated with agglutinate; 2) low-density ($\rho_{avg}$=1.3 g/cm$^3$) andesitic scoria or highly vesicular lava; 3) intermediate-density blocks ($\rho_{avg}$=2.1 g/cm$^3$) of greyish tuff breccia, and reddish-grey agglomerate or agglutinate; 4) intermediate-density blocks ($\rho_{avg}$=2.1 g/cm$^3$) of poorly vesicular columnar-jointed lava (Breard et al. 2014). The type 3 is hetero-lithologic, comprising angular to rounded block or lapilli clasts, incorporated in a firm ash-rich matrix, or within welded agglomerate (Figure 4.3). In the latter case, clasts show variable alteration, with pyrite and chalcopyrite crystals and sulphur filling cracks

(Breard et al., 2014). Blocks of type 1 are the most common and are uniformly dispersed over all the ballistic impact area, whereas type 2 and type 3 clasts occur primarily within the western ballistic field. Type 4 clasts are only found within 1.2 km of the vent. Clasts similar to the Type 3 ballistic block lithology occur frequently within the debris avalanche deposit associated with this eruption, and were also observed in the eruptively excavated western fissure wall (Figure 4.3; Breard et al.,2014).

The exposed lithology on the western wall of the eruption fissure includes several m-thick breccia and diamicton beds (Figure 4.1D, Figure 4.2; Breard et al.,2014). The variably hydrothermally-altered deposits, consist of polylithic proximal breccias, interbedded dense and scoriaceous fallout blocks (up to 1m), along with variably-cemented as well as agglutinated breccias. This is similar to the lithology of the inner Upper Te Maari crater wall (Hobden 1997; Lube et al. 2014).

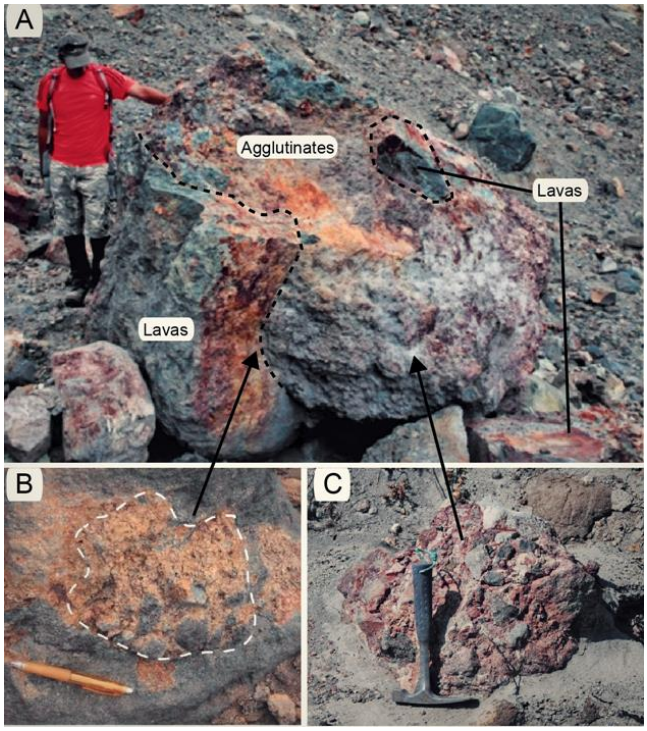


Figure 4.3 In the foreground agglutinates attached to dense lava blocks (delimited by dashed line) and corresponding to the Type 2 block found in the ballistics field (A). Underlying, and in the background, single blocks of lava (block Type 1) are present (B,C).

## 4.3 Laboratory studies

### 4.3.1 Material investigated

Samples were collected from the very proximal debris avalanche deposit (Figure 4.1C,D), as representative of the lithology in the source area (breccias and agglutinates), observed both along the fissure walls (Figure 4.1D), and as Type 3 ballistic blocks (Figure 4.3). The first sample (TMDA_2B) was collected from a welded agglutinate comprising

partially merged, rounded and deformed andesitic lava blocks or lapilli clasts (Figure 4.4). The second sample (TMDA_05) is a breccia of mostly irregular andesitic lava blocks and lapilli incorporated in a firm grey ashy matrix (Figure 4.4). The third sample (TMDA_07) is a similar breccia to TMDA_05, but is characterized by smaller lava clasts showing variable degrees of alteration, and contained within a grey to yellowish fine ash matrix (Figure 4.4). A ballistic block sample from a Type 3 block (TMB), shows similar textures to those of the breccias, and was also used for comparison with the density and porosity properties of the debris avalanche samples (Figure 4.4). Finally a volcaniclastic sandstone from the northern Eldorado Mountains (NEMSS) of southern Nevada, USA (Anderson, 1971) was chosen as control sample. This sandstone´s uniform structure, grainsize, porosity and composition make it a fitting reference material, that has the advantage of constant physical properties across all experiment setups. Cylinders of all investigated blocks were cored to determine dry (oven dried at 70 °C for 24 h) rock bulk density, matrix density and connected porosity (Φ) using a helium pycnometer (Ultrapyc 1200e®, Quantachrome) at the LMU. From these data the open porosity was calculated ($[[V_{calc}-V_{hc}]/V_{calc}]\times 100\%$) (Table1).

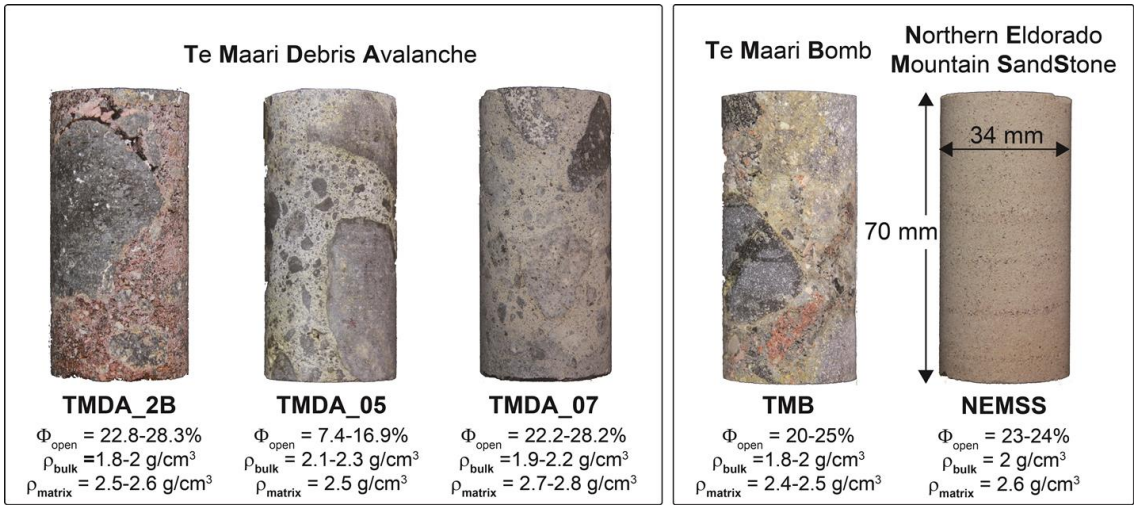


Figure 4.4 Photographs of the three investigated sample series from Te Maari debris avalanches blocks (left). Samples show differences in macroscopic texture, color and particle size in respect to a collected ballistic block of Type 3 (right), and the homogeneous sandstone used as control sample (right).

### 4.3.2 Decompression experiments

#### 4.3.2.1 Methods

A series of rapid decompression experiments have been carried out by using the shock-tube apparatus and the methodology described in sec. 2.5. These experiments were performed to investigate the effect of energy source and rock heterogeneity on the fragmentation and ejection behaviour. In these experiments fragmentation was triggered by decompression of either: i) argon gas, ii) steam, or iii) water flashing to steam within the

connected pore space of the samples. In order to span the range of expected conditions below the Te Maari crater, temperatures ranging from 250°C and 300°C, and pressure between 5 MPa and 6 MPa were chosen for the experiments, (Figure 4.2;Walsh et al., 1998). Control experiments i) were carried out with argon expansion (AE) fragmentation on dry samples at similar temperatures and pressures (300°C and 5 MPa) as for conditions ii). For the latter type of experiments, pre-saturated samples were heated in a vapor-dominated field ii) causing steam expansion (SE). For condition iii) additional argon gas input, allowed maintaining a liquid-dominated field iii) causing steam flashing (SF) (Figure 4.5; Mayer et al., 2015; Rager et al., 2014).

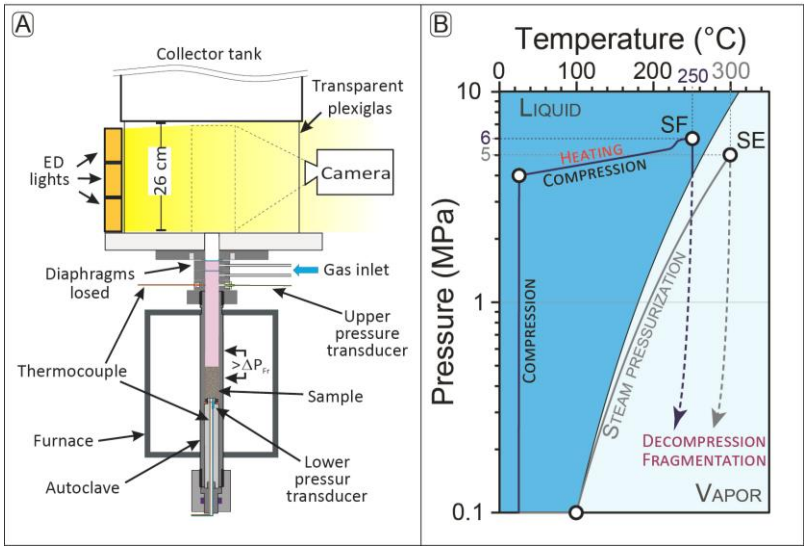


Figure 4.5 Schematic drawing of the experimental setup (A) and temperature and pressure condition during the steam-driven fragmentation experiments (B). More information on the pressurizing, heating and dwelling procedure are reported in in sec. 2.5.

### 4.3.3 Results

#### 4.3.3.1 Grain-size distribution

The results of the grain-size analysis were analysed with respect to their lithology (breccia, agglutinate, and sandstone control sample) and the experimental treatment (AE, SE, SF). Similar grain-size distributions are produced from experiments of each treatment for the different lithologies, confirming experimental reproducibility from the typically heterogeneous material (Figure 4.6, Table4.1).

1) NEMSS: the control sample generally produces fewer coarse clasts than the Te Maari samples. The coarsest grain-size distribution, (Md -1.67ϕ), results from AE, with SE (-0.08 to -0.01ϕ) and SF (0.93 to 1.41ϕ) showing progressively finer grainsize. Fines (>4ϕ) production increased from 0.3% for the AE treatment, to 1.5–2.4% for SE and 4.5% for SF.

2) TMDA_2B samples contain common lava clast enclaves within porous agglutinate. A very coarse grain-size distribution, with a median diameter of -2.9ϕ, resulted from the

AE experiment, but finer overall clast size produced by SE (-0.23 to -0.72ϕ) and SF samples (0.06 to 0.09 ϕ). In the case of fines (>4ϕ), AE produced 0.4 wt%, while SE generated 1.2-1.9 wt% and SF 2.6-3.1wt%. Notably, under the SE condition only ~2/3rd of the sample fragmented, while the higher porosity of the used samples (28.3%) allowed for a total AE fragmentation.

3) TMDA_05 has the largest lava enclaves (up to 6 cm in size) embedded in a fine ash matrix, and show the lowest values in porosity (down to 7.4%). These samples generally produced coarser grain-size distributions amongst the Te Maari samples. Moreover samples only partially fragment (from 2/3 to 1/3 of the whole sample) under both SE and SF conditions, and did not fragment under AE. The mean diameter for the SE case (-2.11 to -1.57ϕ) is slightly lower than that for the steam-flashing samples (-2.64 to -2.18ϕ). Both treatments produced few fines (>4ϕ), with 0.6–1 wt% resulting from the SE and 0.7–1wt% generated by SF.

4) TMDA_07 samples contain few lava enclaves, but the fine matrix has high porosity (up to 28%). A very coarse grain-size distribution (Md -2.71ϕ) is produced by AE, with similar finer clast sizes produced by SE (-0.68 to -0.76ϕ) and SF treatments (0.53 to 0.80ϕ). The amount of fines produced (>4ϕ) increased from 0.8% for AE treatment, to 1.7–2.8 wt% for SE, and 3.7–4.5 wt% for SF.

#### 4.3.3.2 Ejection velocities

Particle ejection velocities (Table4.1) for repeated experiments (to account for sample heterogeneities) were computed from the displacements of individual particles tracked across five successive frames of the high-speed footage. An average speed of those particles at the absolute flow front was calculated using (≥ 5) particle velocities (Mayer et al., 2015). In all experiments was observed that ash particles <2 mm are ejected in the very first phase, generally well-coupled with the gas phase, and were up to 2–3 times faster than >2 mm particles (Table4.1). The >2mm particles were decoupled from the gas phase, with a ballistic-like behavior. For a few SF experiments the initial part of the plume was obscured by large vapor clouds and only the ejection velocities of >2 mm particles were measured (Table4.1).

The ejection velocity of the >2 mm particles in the ejection front varied according to both porosity and experimental treatment (Figure 4.7b,c). Generally the SF treatment produced the fastest ejecta (32 ±2 to 136 ±7 m/s), with SE intermediate (21 ±1 to 85 ±9 m/s) and AE slowest (40 ±2 to 53 ±5 m/s) (Table4.1). Under the SF treatment, fragments produced by the TMDA_07 series were the fastest observed in all experiments, while TMDA_ 05 ejecta were the slowest (46 ±3 m/s). The same pattern was observed in the SE treatment, with TMDA_07 particles as the fastest (71 ±5 m/s), TMDA_2B intermediate (35 ±3 m/s), and TMDA_05 showing one slow example (25 ±1 m/s), and one fast (85 ±5 m/s). The latter was affected by a large cavity later seen in the partially fractured sample and treated here as anomalous. For the AE treatment the ejection velocities were uniform for all lithologies.

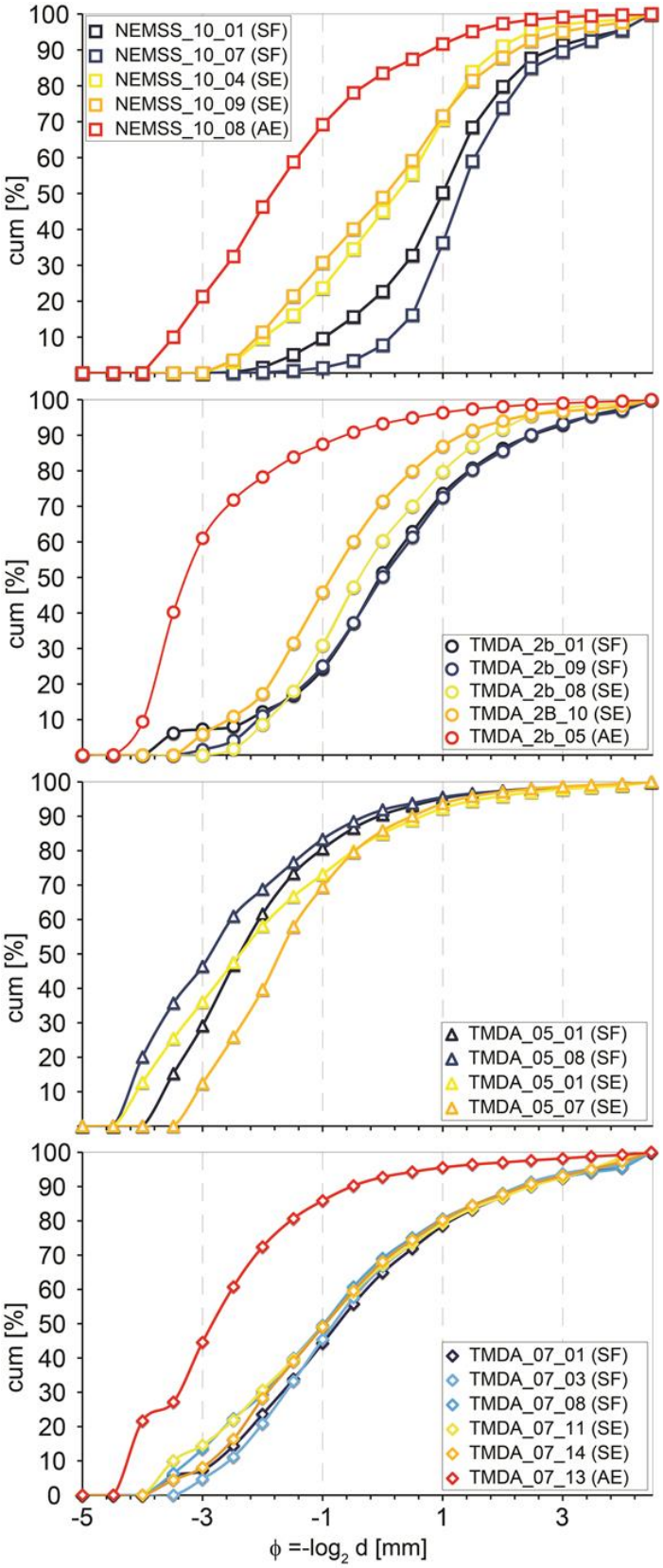


Figure 4.6 Cumulative grain size distribution plots showing the weight fractions of particles after rapid decompression experiments at different experimental condition in half ϕ steps. For each sample series result represent the size distribution produced by steam-flashing (SF), steam expansion (SE) and argon expansion (AE). The particle size is decreasing to the right in all plots.

## 4.4 Energetic considerations

### 4.4.1 Theoretical background

The maximum amount of work that can be extracted from an expansion, an thus the associated explosive energy, depends upon the thermodynamic path (Mastin 1995; Thiéry and Mercury 2009).

For the AE and SE has been assumed that both argon and steam behave as ideal gases and that the expansion is adiabatic and reversible (isentropic). Thus the expansion work must be equal to the variation in internal energy of the fluid $\Delta U$:

$$\Delta U = -P_{atm} \times \Delta V \qquad [4.1]$$

integrating and introducing the relationship $P \times V^{\gamma}$=costant ($\gamma$ being the ratio of specific heats) the energy of expanding gas (argon or steam) can be calculated (Prugh 1991) as:

$$E_{Expl\text{-}R} = [(P \times V)/(\gamma - 1)] \times [1 - (P_{atm}/P)^{((\gamma-1)/\gamma)}] \qquad [4.2]$$

where $E_{Expl\text{-}R}$ is the reversible explosive energy released (J), $P_{atm}$ is the atmospheric pressure (bar), V is the initial volume of argon or steam ($m^3$), and P is the pressure (bar) in the rock pore space just before the explosive failure. The different densities, and therefore masses of argon and steam at different P-T conditions were also accounted for (Table4.1).

For the energy calculations of SF experiments the irreversible approach described in Section 2.4 is used. The explosive energy ($E_{Expl\text{-}I}$) associated to the experimentally produced steam-driven explosions is calculated by means of equations [2.4] and [2.5].

### 4.4.2 Explosive energy during decompression experiments

The estimated explosive energy due to the work of the expanding fluids (argon and steam) was investigated with respect to the experimental treatment. The AE and SE experiments were run at ~300°C and 5 MPa, whereas the SF were carried out at ~250°C and 6 MPa. The explosive energy varied in agreement with both porosity and explosive source (Figure 4.7A; Table4.1). Additionally a direct relationship between explosive energy with the ejection velocity (Sec. 3.3.1), as well as with amount of produced fines (Sec. 3.3.2), can be observed (Figure 4.7B,C; Table4.1).

In general, the SF treatment produced the most energetic explosions (322.6 to 830 J), whereas both SE (35 to 113 J) and AE (87 to 109 J) resulted in less powerful events. Results in terms of energy per unit volume of fluid prior to explosive failure are used to discuss the energies for the different samples (Figure 4.7; Table4.1).

1) The control sandstone NEMSS used for the AE and SE condition experiments have an open porosity range of 23–24.1%, and an energy per unit volume release of 1.4 $MJ/m^3$ was obtained for both conditions. For the SF case, samples retained 14.7–14.9 g of water, and an energy release per unit volume of 12.5–12.9 $MJ/m^3$ was estimated.

2) For TMDA_2B, an open porosity of 22.8–28.3% accounted for an energy per unit volume release of 1.7 MJ/m$^3$ for AE and 1.4 MJ/m$^3$ for SE. Under SF condition, and with 11.7–13.2 g or retained water, an energy per unit volume of 11.3–11.4 MJ/m$^3$is calculated.

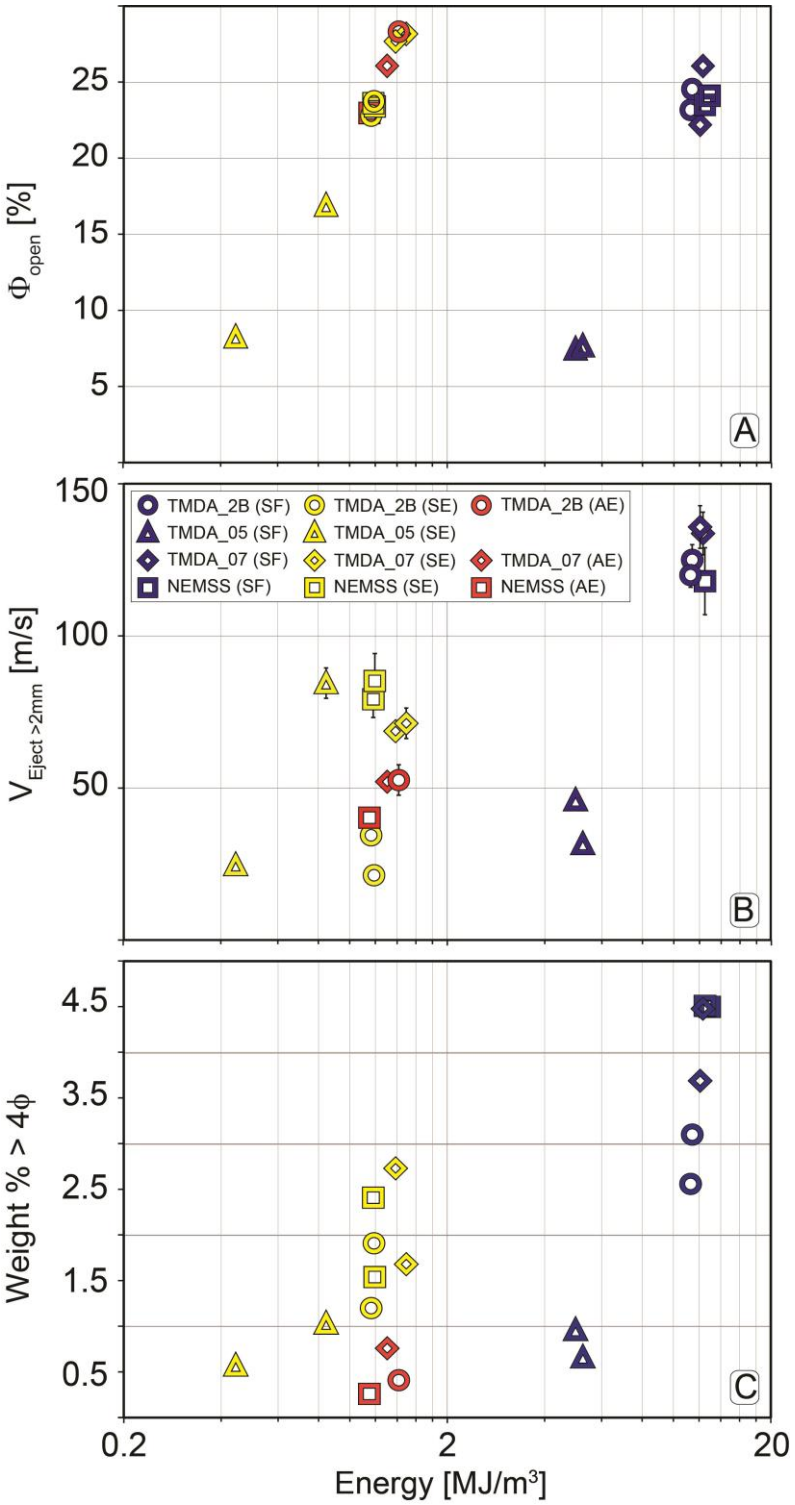


Figure 4.7 Experimental results of (A) sample open porosity, (B) particles ejection velocity, and (C) produced weight % fines (> 4ϕ) as a function of the explosive energy per unit volume in the presence of steam-flashing (SF), steam expansion (SE) and argon expansion (AE). Results are also reported in Table4.1.

**Table 4.1.** Sample properties and experimental results at the different investigated conditions.

| Sample | Rock [g] | $H_2O$/Argon*/Steam* [g] | $V_{calc.}$ [$cm^3$] | $\rho_{calc.}$ [$g/cm^3$] | $V_{meas.}$ [$cm^3$] | $\rho_{meas.}$ [$g/cm^3$] | $\Phi_{Open}$ [%] | T [°C] | P [Mpa] | $E_{expl-R}$ [J] | $E_{expl-I}$ [J] | $E_{Vol}$ [$MJ/m^3$] | $v_{Eject}$ (±Err) [m/s] < 2mm | > 2mm | Wt % > 4 ϕ | Mdϕ |
|---|---|---|---|---|---|---|---|---|---|---|---|---|---|---|---|---|
| *Argon Expansion (AE)* | | | | | | | | | | | | | | | | |
| TMDA_2b_05 | 115.7 | 0.6 | 62.8 | 1.8 | 45 | 2.6 | 28.3 | 300 | 5 | 106 | | 1.7 | 56 (±2) | 53 (±5) | 0.4 | -2.9 |
| TMDA_07_13 | 126.3 | 0.6 | 63.1 | 2 | 46.6 | 2.7 | 26.1 | 300 | 5 | 109 | | 1.6 | 55 (±3) | 52 (±3) | 0.8 | -2.7 |
| NEMSS 10_08 | 127.7 | 0.6 | 63.8 | 2 | 49.1 | 2.6 | 23 | 300 | 5 | 87 | | 1.4 | 70 (±19) | 40 (±2) | 0.3 | -1.7 |
| *Steam Expansion (SE)* | | | | | | | | | | | | | | | | |
| TMDA_2b_08# | 122.8 | 0.2 | 61.8 | 2 | 47.7 | 2.6 | 22.8 | 305 | 5 | 86 | | 1.4 | 92 (±12) | 35 (±3) | 1.2 | -0.2 |
| TMDA_2b_10# | 118.9 | 0.2 | 60.0 | 2 | 45.8 | 2.6 | 23.7 | 298 | 5 | 85 | | 1.4 | 89 (±6) | 21 (±1) | 1.9 | -0.7 |
| TMDA_05_01# | 130.9 | 0.2 | 63.0 | 2.1 | 52.4 | 2.5 | 16.9 | 303 | 5 | 63 | | 1.0 | 121 (±4) | 85 (±5) | 1 | -2.1 |
| TMDA_05_07# | 145.9 | 0.1 | 64.7 | 2.3 | 59.4 | 2.5 | 8.2 | 310 | 5 | 35 | | 0.5 | 79 (±9) | 25 (±1) | 0.6 | -1.6 |
| TMDA_07_11 | 122.9 | 0.3 | 63.2 | 1.9 | 45.4 | 2.7 | 28.2 | 298 | 5 | 113 | | 1.8 | 96 (±7) | 71 (±5) | 1.7 | -0.8 |
| TMDA_07_14 | 124.2 | 0.3 | 62.9 | 2 | 45.5 | 2.7 | 27.7 | 285 | 5 | 104 | | 1.7 | 81 (±7) | 69 (±3) | 2.7 | -0.7 |
| NEMSS 10_04 | 128.7 | 0.4 | 64.5 | 2 | 49.4 | 2.6 | 23.4 | 296 | 5 | 92 | | 1.4 | 127 (±13) | 85 (±9) | 1.5 | 0.1 |
| NEMSS 10_09 | 124.7 | 0.2 | 62.7 | 2 | 47.9 | 2.6 | 23.6 | 300 | 5 | 88 | | 1.4 | 134 (±20) | 79 (±6) | 2.4 | 0.0 |
| *Steam Flashing (SF)* | | | | | | | | | | | | | | | | |
| TMDA_2b_01 | 104.5 | 11.7 | 54.7 | 1.9 | 41.2 | 2.5 | 23.2 | 252 | 6 | | 617.7 | 11.3 | 156 (±11) | 120 (±4) | 2.6 | 0.1 |
| TMDA_2b_09 | 118.8 | 13.2 | 61 | 1.9 | 46 | 2.6 | 24.5 | 250 | 6 | | 696.9 | 11.4 | 157 (±12) | 125 (±5) | 3.1 | 0.1 |
| TMDA_05_06# | 149.1 | 6 | 64.7 | 2.3 | 59.7 | 2.5 | 7.6 | 262 | 6 | | 339.4 | 5.2 | | 32 (±2) | 0.7 | -2.2 |
| TMDA_05_08# | 146.6 | 6.1 | 64.7 | 2.3 | 59.9 | 2.5 | 7.4 | 252 | 6 | | 322.6 | 5 | 77 (±14) | 46 (±3) | 1 | -2.6 |
| TMDA_07_03 | 139.4 | 13.8 | 64.6 | 2.2 | 50.2 | 2.8 | 22.2 | 256 | 6 | | 780.8 | 12.1 | | 136 (±7) | 3.7 | -0.5 |
| TMDA_07_08 | 104.7 | 12.1 | 51.8 | 2 | 37.8 | 2.8 | 26.1 | 254 | 6 | | 638.8 | 12.3 | | 134 (±7) | 4.5 | -0.8 |
| NEMSS 10_01 | 126.9 | 14.7 | 64.1 | 2 | 48.7 | 2.6 | 24.1 | 260 | 6 | | 830 | 12.9 | 177 (±13) | | 4.5 | 0.9 |
| NEMSS 10_07 | 125.3 | 14.9 | 62.8 | 2 | 48.1 | 2.6 | 23.5 | 250 | 6 | | 787 | 12.5 | 200 (±22) | 118 (±11) | 4.5 | 1.4 |

* The argon and steam mass hve been calculated considering their density at the experimental temperature and pressure

# Only partial fragmentation of the sample occurred (from 1/3 for the TMDA_05 to 2/3 for the TMBA_2B)

2) For TMDA_2B, an open porosity of 22.8–28.3% accounted for an energy per unit volume release of 1.7 MJ/m$^3$ for AE and 1.4 MJ/m$^3$ for SE. Under SF condition, and with 11.7–13.2 g or retained water, an energy per unit volume of 11.3–11.4 MJ/m$^3$is calculated.

3) The dense TMDA_05 did not fragment under AE. For SE condition the lower porosity (8.2 and 16.9%) allowed for a volumetric energy release of 0.5 and 1 MJ/m$^3$. Only 6 g of water were retained under SF, resulting in a volumetric energy release of 5 to 5.25 MJ/m$^3$. In both the case the energy was not sufficient to complete a full fragmentation of the sample.

4) The highly porous TMDA_07 samples (26.1 to 28.2%) under AE and SE conditions allowed for an energy per unit volume release from 1.7 to 1.8 MJ/m$^3$. For SF condition samples retained 12.1 and 13.8 g of water which likely released a volumetric energy as 12.1–12.3 MJ/m$^3$.

## 4.5 Discussion

During the landslide from the Te Maari hydrothermal system, pressurized hydrothermal fluids were exposed to rapid decompression. It depends on both the magnitude of pressure drop and the state of the system (pressure, temperature, fluid saturation, and rock strength) as to whether explosive fragmentation occurs. The results from the experiments show how the initial condition of an hydrothermal system, together with the nature of the host rock affects whether an explosion occurs and both the amount of explosive energy, and the grain size and ejection behavior of the resulting fragmented material.

### 4.5.1 Pressure-temperature effect: steam-flashing versus steam expansion

The main finding of the experimental results is that eruptions of the Te Maari rock (and a comparable porosity homogeneous sandstone) are far more energetic when driven by the flashing of high-temperature and high-pressure liquid water into a vapour phase, compared to simply by steam or dry-gas expansion. Therefore the energy is strongly influenced by the pre-existing pressure-temperature conditions of an unroofed hydrothermal system. Pressure and temperature also controls the fluid state, and thus whether flashing, or simple steam expansion, or a combination of both occurs (Mastin 1995; Thiéry and Mercury 2009). A temperature range between 250 and 300°C, with a confining pressure varying from 5 to 6 MPa, was used in this study. Within this range both liquid and vapor water could be filling pores. These conditions agree well with those envisaged below the Te Maari hydrothermal system where a condensate layer existed above a vapor-dominated region (Walsh et al. 1998). This pressure/temperature state, however, was probably pushed to more critical levels by the rise of magmatic gases during magma or fluid rise to shallow levels prior to the Te Maari eruption (Hurst et al., 2014).

### 4.5.2 Porosity and rock texture effects

Heterogeneous tuff breccia with lithics 2–3 m in diameter and agglutinates, showing a large range in porosity (7.6–28.3%), were recognized in large blocks of the debris avalanche deposits, which were also outcropping at the western eruptive fissure. Similar lithologies have been also described outcropping in the inner wall stratigraphy of Upper Te Maari Crater (Hobden 1997; Lube et al. 2014). Porosity of rocks is a key factor in controlling the explosive behaviour of a volcanic system (Spieler et al. 2004b; Scheu et al. 2006; Mueller et al. 2011), particularly in terms of energy storage, which drives the fragmentation behavior (Kueppers et al. 2006). Under all the experimental conditions (AE, SE and SF), explosive energy increases with porosity (Figure 4.7A; Table4.1). Fragmentation behaviour was, however, not only controlled by porosity, but also by the heterogeneity of the rock and the presence of dense lithic enclaves and agglutinate with high rock strength. Compared with the homogeneous control sandstone (NEMSS), the breccias and agglutinates produced sharply distinct polymodal grain-size distributions under all the investigated conditions. The lowest porosity tuff-breccia (~7%), rich in large and dense enclaves embedded in a firm ash matrix, only partially fragmented under SF and SE conditions, and not at all under AE. In between, the agglutinates with similar high porosity (28%), but with a slightly more compacted agglomerate matrix, generate less fine material. In all cases the presence of dense enclaves accounted for the production of coarser clasts (Figure 4.8). By contrast, tuff breccia with higher porosity (up to 28%), and smaller enclaves in a weaker fine ash matrix, produced fine fragments more effectively and produced poorly sorted ejecta in all of the cases (Figure 4.7C, Figure 4.8).

### 4.5.3 Ejection behavior of heterogeneous breccias

The ejection velocity of the gas–particle mixture from the experiments increases with the explosive energy (Figure 4.7B). Steam flashing is additionally responsible for a gas volume increase, that further powers the ejection processes (Mastin 1995; Mayer et al. 2015). This was seen in that the ejection velocities of the particles obtained under the SF conditions yielded the highest velocities (up to 200 m/s), across all sample series (Figure 4.7B, Figure 4.8; Table4.1). The ejection speed of particles in the presence of steam flashing was probably underestimated, because the initial gas expansion obscured the early identification of particles. Velocities reached for the SE and AE cases are half to a third of those produced in the steam flashing case. Additionally, results of the SF treatment show that the very fine material is ejected at higher velocities (50 to 200 m/s) than the lapilli-sized clasts (>2mm). Interestingly, TMDA_2B and 07 series samples were the only ones ejecting particles >2 mm at high velocities (120 to 136 m/s), and only in presence of SF.

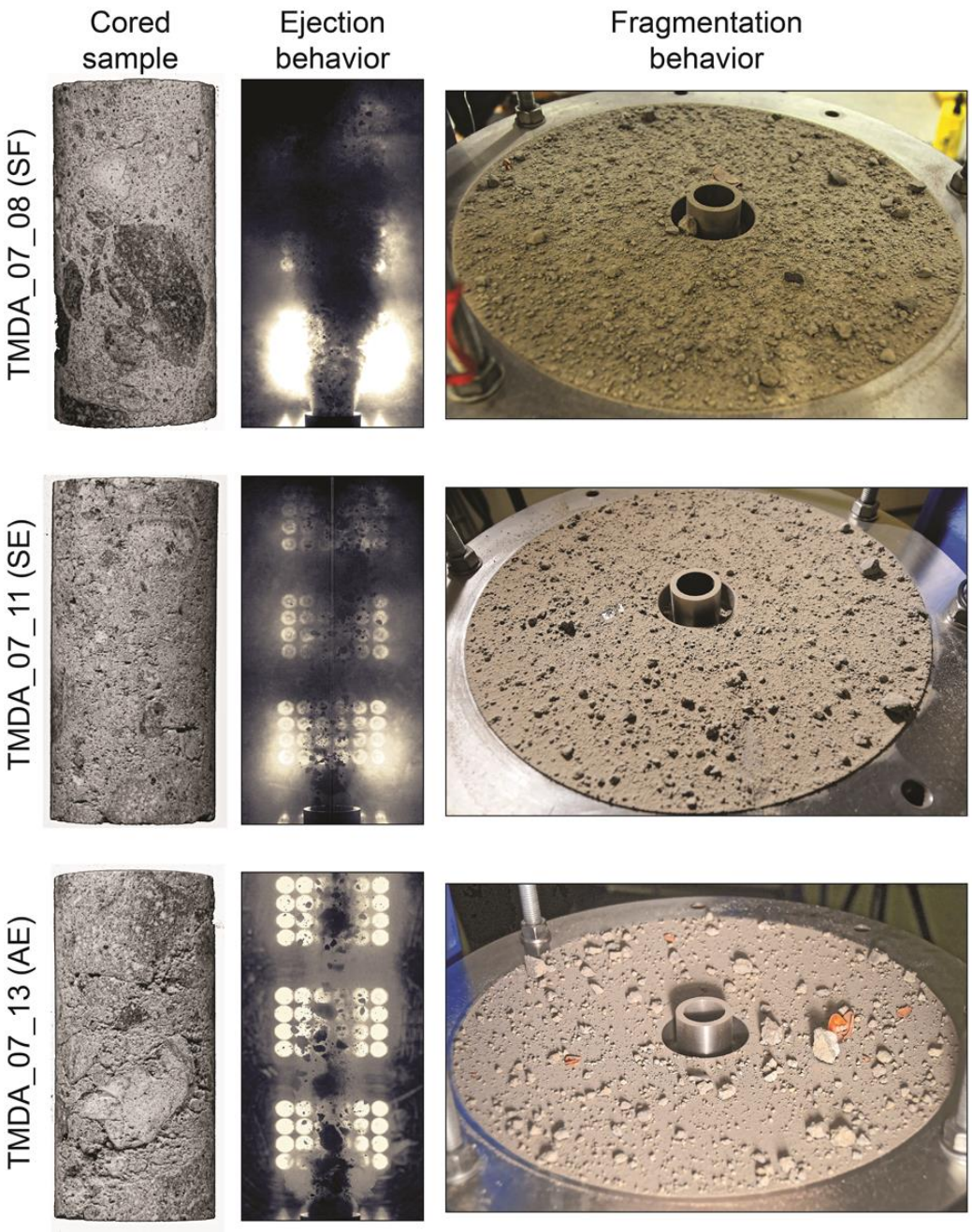


Figure 4.8 From cored to fragmented sample: differences in ejection and fragmentation behavior pro-duced under steam-flashing (SF), steam expansion (SE) and argon expansion (AE) conditions. Example from TMDA_07 series sample. From SF to AE there is a clear increase in the size of ejected material, with a less well-defined plume of fine material formation (frame are taken at the same ejection time). The different rate of coarse and fine material production is also evident in the collector tank base.

### 4.5.4 Energy partitioning

The estimated $E_{Expl}$ (Sec. 4) gives the amount of energy, which can be converted into fragmentation ($\Delta E_f$), gravitational potential ($\Delta E_p$), kinetic ($\Delta E_k$) and all other forms of mechanical energies (noted as $\Delta E_d$) such as elastic deformation, shock waves, etc. Thus, the energetics of fluid flows and eruption phenomena can be assessed by using a modified form of Bernoulli's equation (Mastin 1995; Thiéry and Mercury 2009):

$$E_{Expl}=\Delta E_f+\Delta E_p+\Delta E_k+\Delta E_d+\textit{"frictional-terms"} \qquad [4.3]$$

where the last term accounts for the energy consumption due to rock-fluid internal friction. Expanding gas trapped in pores is the largest energy source that is partially consumed by fragmentation, and partially converted into kinetic energy to expel the fragments (Alidibirov and Dingwell 2000; Alatorre-Ibargüengoitia et al. 2010). A minimum pressure differential, the fragmentation threshold ($P_{fr}$), must be overcome to fully fragment a pressurized porous rock. This threshold is inversely related to the porosity (Spieler et al., 2004). Koyaguchi et al. (2008) proposed a fragmentation threshold criterion based on the Griffith theory for crack propagation through elastic media with a homogeneously distributed porosity. The model of crack propagation from the inner to the outer pore wall, considers the tensile strength of the solid phase and the tangential stress at the outer pore wall, and is defined as:

$$P_{fr}=2\sigma_3\times(1-\Phi)/3\Phi\times(\Phi^{-1/3}-1)^{1/2} \qquad [4.4]$$

where $\Phi$ is the porosity and $\sigma_3$ is the effective tensile strength (Koyaguchi et al. 2008). The estimated values in this study can be considered as a maximum fragmentation threshold for a homogeneous rock. Yet, deviation from this value should be expected when samples are inhomogeneous (Scheu et al. 2006). In the Te Maari case, the explosion host material has an inhomogeneous porosity distribution, a variably-cemented matrix, and localized discontinuities between the matrix and dense enclaves, which may result in a lowering the fragmentation threshold.

The variable open pore spaces of the breccias and agglutinates (~7 to ~28%) used in this study indicate a required gas overpressure $P_{fr}$ of between 5 to 15.4 MPa to fragment them. Using the open pore spaces volume of the experimental samples, and the calculated threshold $P_{fr}$ in equation [4.2], a minimum fragmentation energy $\Delta E_f$ ranging from 89.1 to 110.6 J can be estimated. This fragmentation energy accounts for the primary sequence of fracturing (Fowler et al. 2010; McGuinness et al. 2012), whereas secondary fragmentation consumes lesser amount of energy, and is considered to be negligible here. The estimated energy threshold is exceeded by one order of magnitude in case of SF as an energy source. By contrast very similar values were estimated for SE and AE treatments, resulting in incomplete, or failed fragmentation for the least porous samples of the TMDA_05 and 2B series.

The minimum kinetic energy $\Delta E_k$ associated with the ejected fine material and the lapilli-sized clasts has been assessed. For the calculations the ejection velocities (v) produced under the SF treatment were used, since these are most likely to represent the

process generating the ballistic field of Te Maari (Breard et al., 2014; Fitzgerald et al., 2014). Two size thresholds were chosen for the calculations: the 1 mm as upper limit of the faster particles, and 2 mm as lower limit for the slower particles. It has further assumed that particles have spherical shape and density equal to the measured one for the sample (Table4.1). Then by neglecting the energy dissipated in the accompanying seismic wave and air blast, mass (m) and kinetic energy of the ejected projectiles can be calculated using:

$$\Delta E_k = 1/2 \times m \times v^2 \qquad [4.5]$$

yielding a kinetic energy range between 0.03 to 0.13 J for particles of 1 mm size, and between 0.1 to 0.9 J for the 2 mm size.

Finally for the energetics estimate under SF treatment, the energy conversion ratio of the fragmentation and kinetic energy over the (maximum) explosive energy was evaluated. This ratio defines how efficiently the available energy budget is converted in other forms. The ratio of fragmentation to explosive energy ranges from 9.5 to 15.2%, whereas the conversion ratio to kinetic energy is on the order of 0.02% for the 1 mm size, and up to 0.1% for the 2 mm particles. Note that the latter value yields a good agreement with the ratio estimated for ballistic blocks from numerical modelling based on field data (Fitzgerald et al, 2014).

### 4.5.5 Eruption dynamics of the westward directed plume

The 6th August 2013 eruption of Upper Te Maari was a violent hydrothermal explosive event despite its low erupted volume ($<0.5\times10^6$ m$^3$; Lube et al., 2014). The onset of the landslide and eventual unloading of approximately 0.6 MPa (Procter et al. 2014) destabilised the hydrothermal system and led to its sudden decompression. Weaknesses represented by 1) a paleo-morphology, 2) with sub-horizontal bedding of the variably cemented and agglutinated breccias ponded against the slope of Te Maari Trig to the south (Figure 4.2), and 3) the debris avalanche failure geometry, led to strong lateral jetting. The most energetic westward-directed blasts produced wide-spread pyroclastic surges, and the highest density ballistic strewn-field (Breard et al., 2014). These west-directed ballistics are the only ones that include blocks with a distinctive tuff breccia and agglutinate lithology (TMBA_2B and 7), matching the location of shallow inclined beds of cemented tuff breccia and agglutinate. An exposed ridge separated blast fissures to the east and west. This was composed of hard, low porosity lavas and possibly also strongly cemented rock similar to the TMDA_05 breccia (Figure 4.9).

Based on the experimental conditions of steam-flashing fragmentation, at Te Maari a flashing of pressurized liquid water into a vapor phase would have generated a boiling-front that penetrated downwards into the geothermal reservoir, followed by an explosion front (McKibbin et al., 2009). A minimum explosive energy was obtained for the western blast to be of $7\times10^{10}$ to $2\times10^{12}$ J. The estimation is based on the following assumptions: 1) an excavation depth between 20 and 50 m over ~11000 m$^2$ (Procter et al., 2014); 2) a source rock composed by tuff breccias and agglutinates with a porosity range between 7.5 and 26% (Table4.1); and 3) an experimentally-estimated energy release per unit volume of

5.24 to 12.3 MJ/$m^3$. The upper value (~$10^{12}$J) is of the same order of magnitude estimated by Jolly et al. (2014). This calculation shows that the energy released solely by the process of flashing of liquid water could explain the eruption and no further gas-pressure (e.g. from magmatic gases) for magmatic eruption is needed.

Based on the ballistic lithology and distribution (Breard et al., 2014), and by assuming the downward migration of the explosive process, it has been speculated that an initial shallow-seated locus of steam expansion fragmented part of lava flows (Type 4 block) and layers of tuff breccia, ejecting ballistic blocks at a very low-launching angle (~1°; Breard et al., 2014) over a wide area (Figure 4.9A). Following this, the fragmentation front may have migrated eastward and deeper into more porous breccias and agglutinates (as represented by TMDA_2B and 07). The fragmentation experiments show how efficiently these rock types disintegrated into fine ash, which likely generated surges. Weakly embedded dense enclaves from the matrix of these materials were then easily launched as ballistics. During this phase a more elongated eruptive zone developed with the ejection angle increasing (up to 10–20°) as the focal depth of explosion deepened, leading to blocks showering over a narrower area (Figure 4.9B,C). The ejection dynamic phases inferred here are similar to the eyewitness observations, and the jet shapes produced during natural eruptions (Yokoo et al. 2002), and on field-based explosion experiments at varying shallow depths (Ohba et al. 2002; Taddeucci et al. 2013; Valentine et al. 2015). Moreover this inferred scenario yields good agreement with the one inferred from the ballistic strewn-field (Breard et al., 2014).

Experimental results suggest that only SF would be energetic enough to launch fragmented particles at speeds (120–136 m/s) estimated from both field data and numerical modelling (Breard et al., 2014; Fitzgerlad et al., 2014). Additionally, experiments on TMDA_07 and 2B samples showed how the SF mechanism accelerated abundant fine material out to front velocities of ~160 m/s. Ejection of this fine material, well coupled with gas expansion, likely drove the surges associated with the Te Maari blasts. The experimental fines ejection value is a good indicator of initial surge velocity, which commensurate with estimates (>100 m/s) of Lube et al. (2014) based upon field data.

An eruption driven in this way by SF terminates once the rate of groundwater boiling slows, with SF giving way to SE that eventually ceases to provide sufficient energy to eject rocks (McKibbin et al., 2009). Deepening and eastward opening of the fragmentation front, where rocks similar to the TMDA_05 breccias or solid lavas would reduce explosive energy also through their naturally lower porosity.

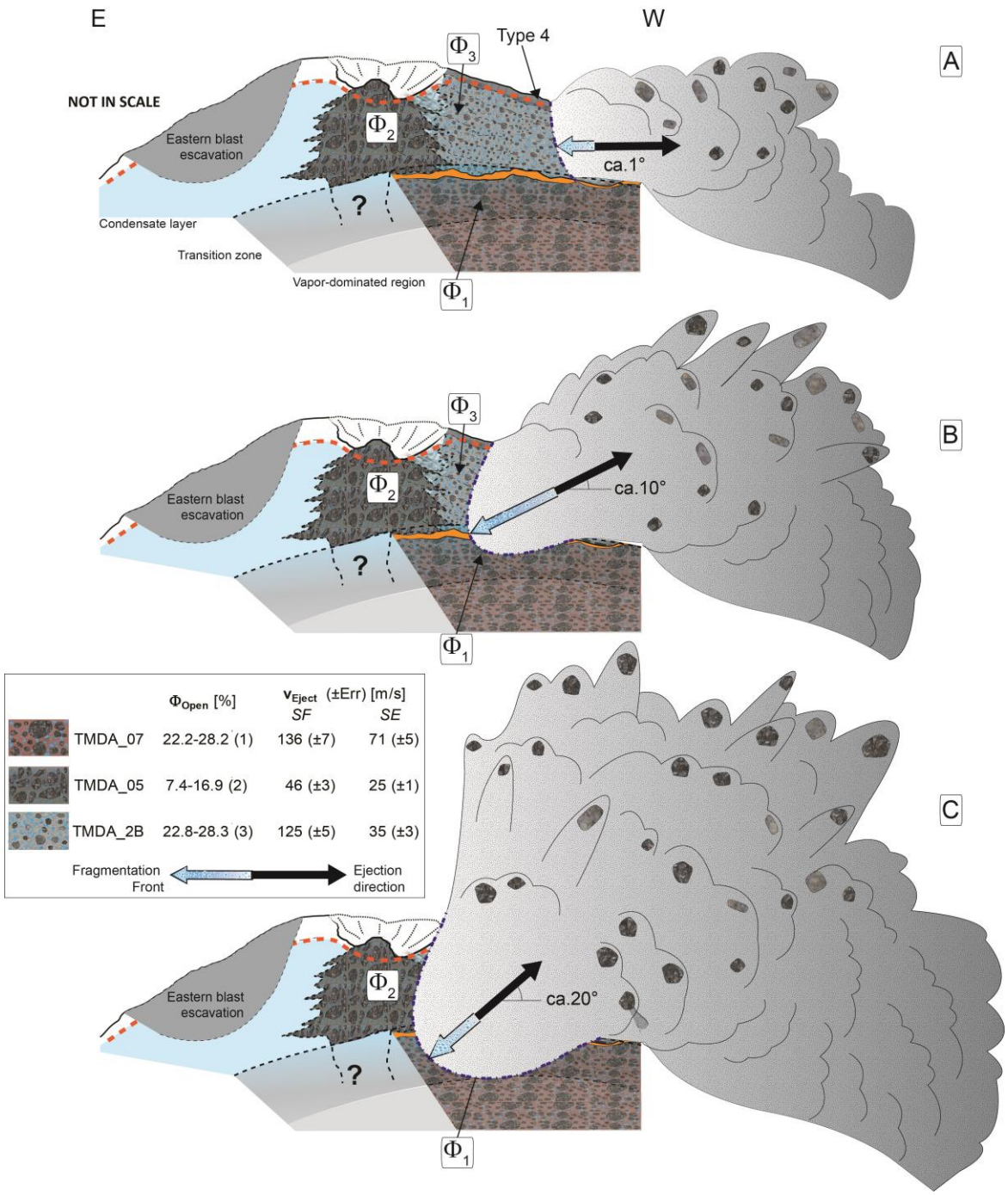


**Figure 4.9** Phase 2 of the Te Maari hydrothermal eruption: conceptual model of the fragmentation and ejection process during the westward directed blast evolution. In the legend the ejection velocity are referred to particles larger than 2 mm. In this simplified model the lithology is assumed to correspond to the tuff breccia and agglutinated (having a different porosity and lithologic texture) used as sample material for the decompression experiment, being representative of the source rock. Type 4 refers to a block type described in Breard et al., 2014, and originated from the fragmentation of the 1528 lava flow (an part of smaller recent lavas). The length of the "Fragmentation Front arrow give an idea of the fragmentation speed in the different lithology. More explanation on the evolution from A to C in the text.

## 4.6 Conclusions

The 6th August 2012 hydrothermal eruption at Upper Te Maari crater was triggered by a landslide on the western flank, unroofing the hydrothermal system. The experiments reported in this study add to field- and modelling findings and additionally demonstrate the mechanism for destabilisation of the system.

The rapid decompression experiment setup on natural hydrothermally altered samples (tuff breccias and agglutinates) and the conditions (260 °C-6 MPa and 300°C-5 MPa) are representative of the shallow condensed layer and the vapor-dominated region envisaged below the Te Maari eruption source area. The triggered decompression mimics the hydrothermal eruption mechanism well, allowing exploration of the effect of different P-T conditions (determining the fluid state), amount of stored energy and impacts of rock strength and porosity. Findings included:

1) under the envisaged pressure-temperature condition of the hydrothermal system, both water vapour or liquid-to-vapor (flashing) expansion could occur, but the latter is significantly more energetic and far more likely to explain explosions like the Te Maari one;
2) the rock porosity controls the amount of stored energy, with higher porosities accounting for higher energies;
3) an increasing porosity also leads to the production of greater amounts of fine material because more energy (SF or SE) is available. Furthermore, at a constant porosity, weaker porous tuff breccias and agglutinates produce more fines than the firmly cemented enclave-rich breccia. Additionally the very dense lava enclaves embedded in the matrix of the breccias and agglutinate often remain unfragmented;
4) for higher porosities, higher acceleration and ejection velocities of particles ahead of the fragmentation front occurs. In particular smaller particles (<2 mm) are better coupled with the gas and are ejected more rapidly than the larger “ballistic” clasts which are rapidly decoupled from the gas expansion;
5) greater fines production and propelling of fines forward with SF experiments provides a mechanism to generate pyroclastic surges, with initial velocities exceeding 160 km/hr;
6) for the investigated Te Maari case the comparison of the field data with the experimental results, together with analytical modelling yields robust estimates for the energy partitioning in this violent hydrothermal eruption. Host rock lithology, appears to control the explosion dynamics (geometry) and energy partitioning. The strong westward blast generated during the Te Maari eruption, released half of the total energy of the whole eruption, and was sustained by the process of liquid water flashing to steam.

Phase changes during decompression together with the rock type, porosity and rock strength are important fragmentation variables that should be considered for hazard assessment and modelling of eruptions in hydrothermally active environments. Overall, the highest hazard will be associated with destabilisation of a hydrothermal system that is under conditions promoting higher pressures and larger fractions of water, that is >250$^{o}$ C temperatures, >20% porosity and water in a liquid state.

This page was intentionally left blank.

This page was intentionally left blank.

# Chapter 5

# *Experimental investigation of the explosivity of steam-driven eruptions: case study from Solfatara volcano, Campi Flegrei*

*You see all these volumes of steam, Axel: well,*
*they demonstrate that we have nothing to fear*
*from the fury of a volcanic eruption.*

*"Otto Liedenbrock" in Journey to the Center of the Earth (1966)*
*Jules Verne*

## 5.1 Introduction

The violence (or explosive power) of steam driven eruptions depends largely on the different explosivity of fluids (liquid or gas) driving them, as well as on the rate of mechanical energy release. Both these factors are in turn controlled by 1) the liquid fraction and the physical condition, in terms of pressure and temperature (P-T) of a system before the explosive event (Mastin 1995; Thiéry and Mercury 2009; Thiéry et al. 2010), and 2) the petrophysical properties (mainly porosity, permeability and strength) of the host rock (Thiéry and Mercury, 2008; Thiéry et al., 2010; Haug et al., 2013; Galland et al., 2014). More specifically the pressure-temperature conditions together with the porosity control the phase of the fluid and the stored explosive energy, respectively. Instead the energy partitioning in terms of fragmentation energy and kinetic energy mostly depends on the rock porosity, permeability, and strength (Montanaro et al., 2016; Thiéry and Mercury, 2009). A wide range of initial temperature, pressure and liquid fraction, as well as a variety of rock types characterizes the volcanic environments affected by steam-driven eruptions (Browne and Lawless 2001). Consequently this eruption type is very versatile, exhibiting a wide spectrum of eruptive styles.

To estimate the effect of these parameters on the explosion energy and on its release, a scenario likely for steam-driven eruptions at the Solfatara and Pisciarelli fumaroles was investigated (Figure 5.1). These two sites represent the main surface manifestations of the vigorous hydrothermal system within the Campi Flegrei (hereafter CF) caldera, which is thought to consist of a gas plume fed by fluids of deeper magmatic and meteoric origin (Figure 5.1B; Caliro et al., 2007). Consistent with the volcanic history of the area (Orsi et al. 2004; Isaia et al. 2015), Solfatara and Pisciarelli bear the highest probability for the opening of new vents, and in particular for possible explosive eruptions. A complex fault

system, related to the maar-diatreme origin of the Solfatara crater, is driving the outgassing which in turn leads to a strong alteration of the volcanic products in both areas (Isaia et al. 2015; Piochi et al. 2015). Additionally, recent physical simulations suggest an increased fluid flux within the last two decades, which is deriving from depth and feeding the hydrothermal system (Todesco 2009). This may have intensified the condensation of water within and at the border of the gas plume, and in turn, the heating of the rock by the latent heat release during condensation (Chiodini et al., 2015 and reference therein). The presence of a condensed steam, migrating along the fractured zone, is considered as the possible source of explosivity involved during a possible destabilization of the hydrothermal system. Different types of tuffs which are inferred to reflect the deposits below Solfatara (Di Vito et al. 1999), have been used for the experiments.

This study aims to investigate the role of the liquid fraction (from dry to partially and fully saturated) and the rock properties (porosity, permeability and strength) on the explosive power by the use of experimental modelling, together with thermodynamic estimates. A series of rapid decompression experiments were performed with different rock types and different degrees of sample saturation (with water), at initial elevated temperatures and pressures (Rager et al., 2014; Mayer et al., 2015). Petrophysical properties of the used rocks were determined prior to the decompression experiments, while calculations based on an irreversible thermodynamic approach are explored to estimate the explosive energy (Prugh 1991; Planas-Cuchi et al. 2004; Thiéry and Mercury 2009).

## 5.2 Explosivity of water in hydrothermal system

In the *chapter 2 and 4* of this thesis the explosive energy associated to steam-flashing and argon gas expansion are introduced, and the equation to calculate the energy described.

For this part of the study the equation [4.2] is used to calculate the explosive energy ($E_{Expl\text{-}R}$) associated to the argon expansion.

For the energy calculations of SF experiments the irreversible approach described in Section 2.4 is used. The explosive energy ($E_{Expl\text{-}I}$) associated to the experimentally produced steam-driven explosions is calculated by means of equations [2.4] and [2.5]. Results are reported in Section 5.5.2.

## 5.3 Geological setting of the case study: Solfatara and Pisciarelli

Solfatara and Pisciarelli are fumarolic areas located within the densely populated CF caldera (Figure 5.1A). The CF area has been blanketed by two large caldera eruptions occurred ~40 and ~15ka, resulting in the Campanian Ignimbrite and the Neapolitan Yellow Tuff, respectively (Orsi et al., 2004; Vitale and Isaia, 2014 and reference therein; Figure 5.1). Within the last 14.9 ka at least 73 phreatomagmatic eruptions, mostly clustered in three main epochs of activity and separated by intervals of at least ~1,000 years, affected the caldera (Di Vito et al., 1999; Isaia et al., 2009 and references therein). During the last epoch most of the active vents were located in the central-eastern sector of the caldera (Vilardo et al. 2010). Here a series of 15 explosive and effusive eruptions occurred over a

period of 500–600 yr, with an interval of about 100-200 years of repose after the Agnano-Monte Spina plinian eruption (Smith et al. 2011). One of the vents generated within this epoch of volcanism was the Solfatara volcano.

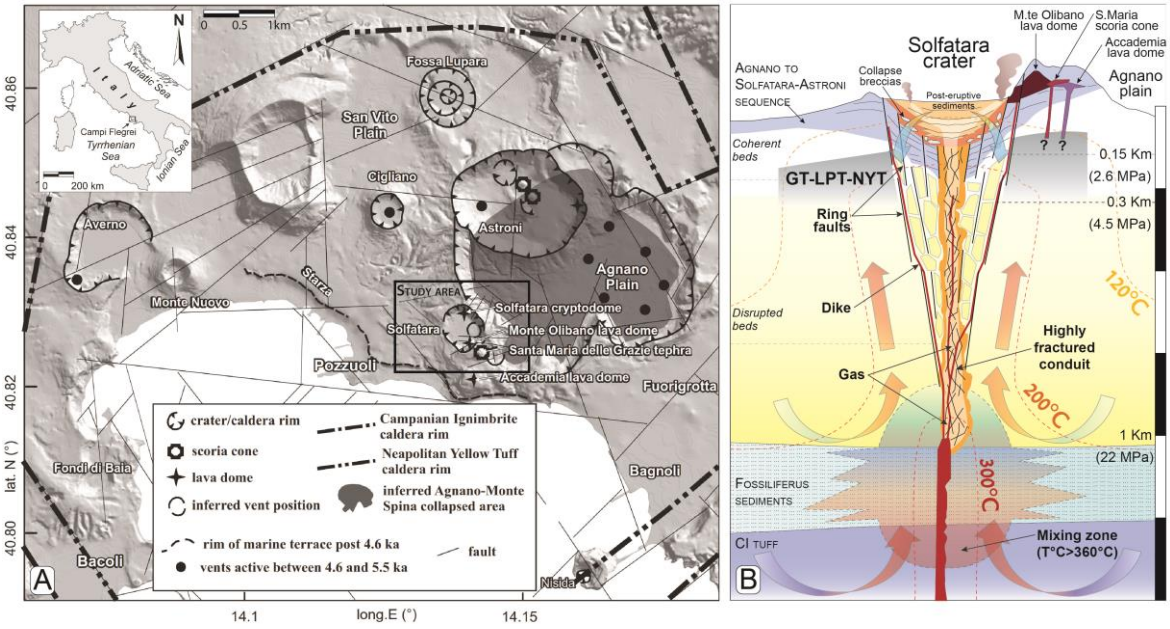


Figure 5.1 Map of the central sector of Campi Flegrei (A). Conceptual model of Solfatara crater showing the maar-diatreme structure, containing the tuff samples used as representatives for individual areas below Solfatara. The scale bar unit on the right of the figure is 250 m. Modified from Caliro et al. (2007) and Isaia et al. (2015) (B).

In more recent times both the inside of the Solfatara crater as well as the eastern flanks towards Pisciarelli have undergone a vigorous hydrothermal and fumarolic activity (Caliro et al. 2007; Scandone et al. 2010). During the period 1970–1972 and 1982–1984 the crater area has been affected by the deformation accompanying the unrest in the Campi Flegrei caldera (Barberi et al., 1984; Dvorak and Gasparini, 1991). An intense seismic activity was localized in correspondence with the Solfatara crater (Orsi et al., 1999a and references therein), and new fractures were generated (Vitale and Isaia, 2014; Isaia et al., 2015). Since then Solfatara volcano and the surrounding area have been intensely monitored, and detailed geochemical and geophysical investigations have been carried out (Chiodini et al. 2001; Bruno et al. 2007; Caliro et al. 2007; Petrosino et al. 2012; Moretti et al. 2013; Caliro et al. 2014; Chiodini et al. 2015). Results of the geochemical analysis from fumarolic gases (Caliro et al., 2007, 2014) outline a complex hydrothermal system localized below Solfatara crater, including an upwelling of deep magmatic, CO-rich fluids, mixed with hydrothermal liquids of meteoric origin and forming a hydrothermal plume that feeds the fumaroles at the surface. The mixing of these fluids occurs at high temperature (>350 °C) at the base of the hydrothermal system (1–1.5 km), whereas a shallow vapor-liquid zone is imaged to be located at depth between 150 and 300 m (2.6-4.5 MPa) where temperatures range between 190 to 250°C. (Figure 5.1B; Caliro et al., 2007, 2014; Piochi et al., 2014, 2015). Recent episodes of mud emissions and the formation of boiling pools of

condensates at Pisciarelli (Chiodini et al. 2011), together with the presence of resistive gas bodies below the fumaroles in Solfatara, overlain by conductive descending bodies of liquid condensates (Bruno et al. 2007; Byrdina et al. 2014), support the occurrence of deep processes of condensation within the buried Solfatara gas plume (Chiodini et al. 2015). Gas and fluid flows are driven by both the rock permeability and the fracture systems. The latter is the result of the explosive activity and collapse faulting in the area caused during the maar-diatreme evolution (Isaia et al., 2015). The eruptive sequence associated to this maar-formation event was characterized by an opening phreatic phase, followed by phreatomagmatic activity. The phreatic deposits contained shallow and deep-seated lithic fragments, including a peculiar green tuff which was also recognized in the Pozzuoli coast (La Pietra tuffs; Di Vito et al., 1999) and found in drill cores from the Agnano Plain (Piochi et al., 2014).This indicates multiple volcanic explosions at various depths (Valentine et al. 2012; Graettinger et al. 2014). The presence of the tuff-lithic component further confirms the previous knowledge of the stratigraphy in the shallow part of the caldera and below the Solfatara area, where borehole stratigraphy indicates a widespread sequence of yellow and green tuffs (Rosi et al. 1983; Orsi et al. 1996; Orsi et al. 2004; Piochi et al. 2014).

### 5.3.1 Material investigated

In order to investigate the influence of rock properties on the explosivity of steam-driven eruptions, tuff rocks expected to be located below the Solfatara area were chosen (Figure 5.1B), and which are characterized by different physical and mechanical properties. In particular, rock samples from the Neapolitan Yellow Tuff (NYT), together with the La Pietra (LPT) and Gauro (GT) Tuff, have been collected as sample material for this study (Figure 5.2). The NYT is considered to be one of the most abundant and widespread volcanic deposit in the CF volcanic district (Orsi et al. 2004). The GT deposit is also one of most voluminous tuffs emplaced during the last epoch of activity (III epoch) in the CF, and preceded the Solfatara formation (Di Vito et al. 1999). The LPT, also older than the Solfatara deposits (Di Vito et al. 1999), is outcropping in a nearby area towards the southern part of the crater. The LPT deposit is characterized by an alternate layering of pumice-enriched (LPT-1) and ash-rich (LPT-2) levels; therefore both rock types were sampled and individually investigated. It has been assumed that the uppermost part of the shallow hydrothermal reservoir below Solfatara consists of similar rocks as those collected to represent the stratigraphy below the crater area (Piochi et al., 2014 and literature within). A further assumption include that the properties of tuffs collected at the surface are representative of those at depth of 300 m (within the shallow hydrothermal zone). This assumption is supported by the fact that mechanical properties of tuffs from drill cores at a depth of 500 m are similar in terms of porosity, permeability, density and texture (Carlino et al., in review)

In order to investigate the influence of rock properties on the explosivity of steam-driven eruptions, tuffs expected to be located below the Solfatara area were chosen (Figure 5.1B), and which are characterized by different physical and mechanical properties. In particular,

rock samples from the Neapolitan Yellow Tuff (NYT), together with the La Pietra (LPT) and Gauro (GT) Tuff, have been collected as sample material for this study (Figure 5.2).

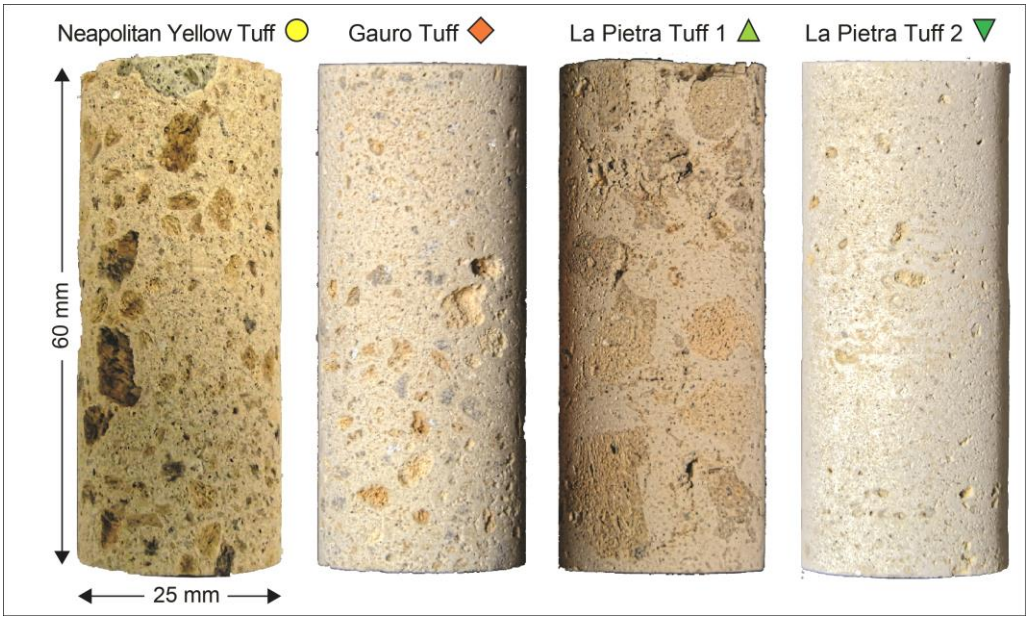


Figure 5.2 Photograph of cylindrical sample of each tuff as used in the experiments. Samples show differences in macroscopic texture, color and particle size. The Neapolitan Yellow Tuff (NYT) and La Pietra Tuff 1 (LPT-1) contain abundant and large pumices and lithics within a fine matrix, whereas the Gauro Tuff (GT) and the La Pietra Tuff 2 (LPT-2) show a more ash-dominant component

## 5.4 Experimental studies

### 5.4.1 Methods

#### 5.4.1.1 Petrophysical characterization

Petrophysical properties were determined on cylindrical samples (60 mm length, 25 mm diameter; Figure 5.2) of all investigated tuffs; samples were cored perpendicular to the layering if existing. Bulk density, matrix density, and connected porosity of dry (oven dried at 65 °C for 24 h), cored cylinders were measured using a helium pycnometer (Ultrapyc 1200e®, Quantachrome). The connected porosity of the sample is calculated using the matrix volume ($Vol_{matrix}$) derived by Helium pycnometry and its geometric (bulk) volume ($Vol_{geo}$).

$$\text{Connected porosity} = [(Vol_{geo} - Vol_{matrix}) / (Vol_{geo})] \times 100 \qquad [5.1]$$

Gas permeability measurements of selected cylindrical samples were conducted under a confining pressure of 1 MPa by using a GasPerm (GPE-100, Vinci Technologies). The device allows for determination of permeability to gas at steady state (constant pressure and flow through the sample). A mass flow meter (range 5-500 cc/min) together with a

relative pressure transmitter (up to 0.69 MPa) were used to sense gas flow and pressure drop across the sample. Permeability was derived from the flux measurements by using Darcy's law (Klikenberg 1941). Ultrasonic wave velocities were measured in a benchtop apparatus where the sample is placed between two vertical endcaps equipped with piezoelectric transducers (with a resonant frequency of <1 MHz) connected to a pulse generator (Agilent Technologies 33210A, 10 MHz function/waveform generator) and an oscilloscope (Agilent Technologies DSO5012A). The onset of P-wave arrival at the receiver was individually picked as the first deviation from the baseline signal. Uniaxial compressive strength (UCS) tests were carried out at the Technische Universität München. Samples were pressed under a constant strain rate of $3.3\times10^{-4}$ $s^{-1}$ and a constant deformation rate of 0.03 kN/s, respectively. Axial strain and stress were continuously monitored during deformation, by displacement transducers and by a load cell, until failure. Samples for UCS tests were shaped with their end-faces ground flat and parallel, and with a length-diameter-ratio of 2:1. Both UCS and P-wave velocity were measured under dry and 100% water saturation conditions. Fragmentation threshold, which represent a dynamic response to a normal tensile stress (Spieler et al. 2004b), was also determined by using a fragmentation bomb as described in the following section.

#### 5.4.1.2 Decompression experiments

A series of rapid decompression experiments have been carried out by using the shock-tube apparatus and the methodology described in sec.2.5. These experiments were performed to investigate the effect liquid fraction within connected pore and rock petrophysical properties on the fragmentation and ejection behaviour. In these experiments fragmentation was triggered by decompression of either: i) argon gas (AE), ii) steam flashing (SF), or iii) combination of the two within the connected pore space of the samples.

The experiments were designed to mimic a decompression involving the upper part of the hydrothermal plume imaged below Solfatara and Pisciarelli area (Figure 5.1). Assumption for the hydrothermal reservoir include 1) a temperature of approximately 250°C and a pressure of 4.5 MPa (Figure 5.3), 2) a zonation within the plume with gas-rich and condensed steam areas, and 3) a host rock with petrophysical properties similar to the different tuffs investigated in this study (Figure 5.1B; Caliro et al., 2007; Chiodini et al., 2015; Piochi et al., 2014). Therefore AE and SF are the possible sources driving the fragmentation and the ejection of particles (Rager et al. 2014; Mayer et al. 2015). The properties of Argon gas are very similar to those of $CO_2$, which is the second largest contributor to the fumarolic gases in Solfatara and Pisciarelli (Caliro et al. 2007). In order to evaluate the different behavior initiated by SF at different liquid fraction samples with 0% (dry), 50% and 100% water saturation were used. Thereby either a combination of AE and SF, or pure SF, is leading to fragmentation and ejection of the sample. The NYT, GT and LPT (1-2) were used for these experiments in order to evaluate the effects of mechanical properties on the fragmentation and ejection behavior.

Differently from the method for fully-saturated sample (sec. 2.5), the correct amount of water required for saturating 50% of the known porosity of the sample was placed in a container together with the sample and then kept under moderate vacuum. The high imbibition capacity of the different investigated tuffs (Colella et al. 2009; Morra et al. 2010) and the continuous turning of the sample during the saturation, assured a quite homogeneous distribution of water within the whole sample.

The fragmentation threshold, i.e. the initial pressure required to fragment the whole rock sample (Koyaguchi et al., 2008; Scheu et al., 2006; Spieler et al., 2004b), was first determined for all the tuffs at room temperature (dry condition). Next the different tuffs in dry, partially (50%) and fully water-saturated conditions were tested. For the experiments performed on both dry and saturated samples the system was initially pressurized to ~3 MPa. Target temperature of 250 °C was reached after a heating time of 25 minutes. For the saturated samples the initial pressurization ensured the water to remain in the liquid state throughout the heating phase. During the last stage of the heating the remaining pressurization, required to reach a pressure of 4.5 MPa, was applied. Holding these final conditions for a dwell time of at least 10 minutes ensured temperature and pressure equilibration over the entire sample, before triggering the fragmentation. During the decompression of the system, the phase transition from liquid water to water vapor is crossed (Figure 5.3B).

Finally for each sample the fragmentation speed is calculated by using the time delay $\Delta t$ of the pressure drop over the entire sample, as recorded by the transducers above and below the sample, and the sample length Scheu et al. (2006).

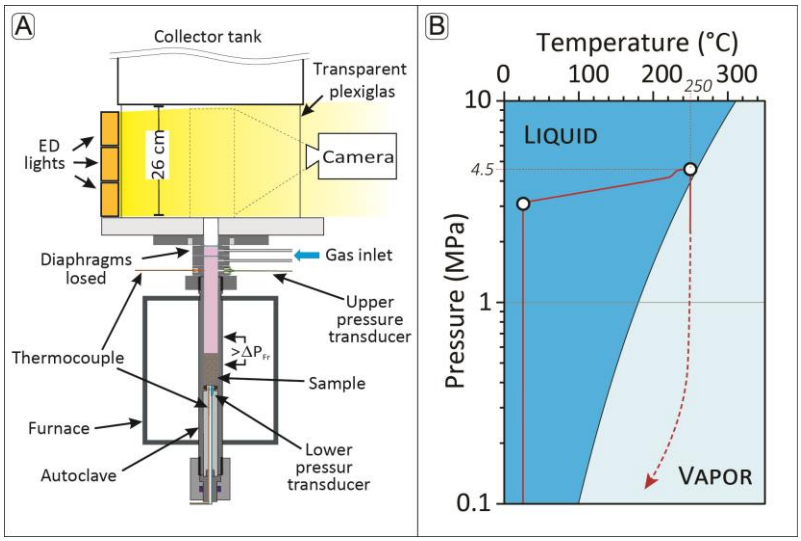


Figure 5.3 Schematic drawing of the experimental setup (A) and temperature and pressure condition during the steam-driven fragmentation experiments (B). More information on the pressurizing, heating and dwelling procedure are reported in in sec. 2.5

## 5.5 Results

### 5.5.1 Petrophysical properties

Table 5.1 summarizes the main rock petrophysical properties of NYT, GT and LPT1-2, which are also shown in Figure 5.4. All tuffs shows high values of connected porosity ranging between 41.3 and 50.3%. All samples contain abundant pumices and lithics within a fine matrix of zeolites (phillipsite and chabazite) forming the microporous texture of the samples (De' Gennaro et al. 1999). Hg-porosimetry of the NYT performed by Colella et al. (2009), indicate a bimodal pore size distribution characterized by subordinated macro pores and primarily meso- and micropores (0.01-1μm). The permeability of the samples ranges between $1.4\times10^{-13}$ to $2\times10^{-15}$ $m^2$, with the more permeable samples being the pumice-rich NYT and LPT-1 (ca.$10^{-13}$ $m^2$). The standard deviation for permeability values are in the range between $1.1\times10^{-13}$ to $1.9\times10^{-17}$ $m^2$, and are reported in Table 2. The relation of rock permeability in respect to the porosity allows to identify three main groups: 1) a highly permeable and very porous group which include NYT and LPT-1 samples, 2) an intermediate permeability and low porosity group formed by GT, and 3) a very low permeability and intermediate porosity group of LPT-2 (Figure 5.4A). Despite the high textural heterogeneities of the tuff series (Figure 5.2), they showed a narrow range concerning the bulk and apparent density varying between 1070-1330 kg/$m^3$ and 2220-2380 kg/$m^3$, respectively.

Table 5.1 Main petrophysical features of the investigated tuffs

| | **Neapolitan Yellow Tuff (NYT)** | **Gauro Tuff (GT)** | **La Pietra Tuff 1 (LPT-1)** | **La Pietra Tuff 2 (LPT-2)** |
|---|---|---|---|---|
| Connected porosity [%] | 47.8-50.3 | 41.3-46.6 | 48.3-49.2 | 46.4-48.5 |
| Permeability [$m^2$] | $4.3\times10^{-13}$<br>$1.4\times10^{-13}$ | $1.6\times10^{-14}$<br>$3.3\times10^{-14}$ | $5.6\times10^{-14}$<br>$2.8\times10^{-13}$ | $3.7\times10^{-15}$<br>$2\times10^{-15}$ |
| Dry bulk sample density [kg/$m^3$] | 1070-1200 | 1250-1330 | 1180-1240 | 1210-1240 |
| Dry apparent sample density [kg/$m^3$] | 2220-2320 | 2130-2340 | 2330-2380 | 2220-2320 |
| Dry P wave velocity [km/s] | 0.9-1.3 | 1.4-1.6 | 0.7-1.2 | 1.1-1.5 |
| Wet P wave velocity [km/s] | 1.9-2.2 | 2.1-2.2 | 1.6-1.8 | 2.1-2.7 |
| Dry UCS strength [MPa] | 6.1-7.3 | 10.8-13 | 4.2-5.5 | 8.9-10.5 |
| Wet UCSstrength [MPa] | 1.2-2.3 | 4.3-5.1 | 1.3-3.1 | 3-5 |
| Fragmentation threshold [MPa] | 1.5-1.7 | 3.5-4.5 | 2.5-3.1 | 3.3-3.6 |

Figure 5.4B shows the relation between rock P-wave velocities respect to UCS. For dry samples the P-wave velocities of the more porous NYT and LPT-1 (0.7 to 1.3 km/s) are lower than those for the less porous and denser LPT-2 and GT (1.1 to 1.6 km/s). UCS values also show a lower values for the NYT and LPT-1 (4.2 to 7.3 MPa) than for the GT and LPT-2 (8.9 and 13 MPa). For the 100% water saturated samples both P-wave and UCS are reduced in respect to the dry conditions. Wet P-wave velocities of NYT and LPT-1 (1.6 to 2.2 km/s) are lower than for the GT and LPT-2 (2.1 to 2.7 km/s). Wet UCS of NYT and LPT-1 (1.2 to 3.1 MPa) are as well lower that for GT and LPT-2 (3 to 5.1 MPa).

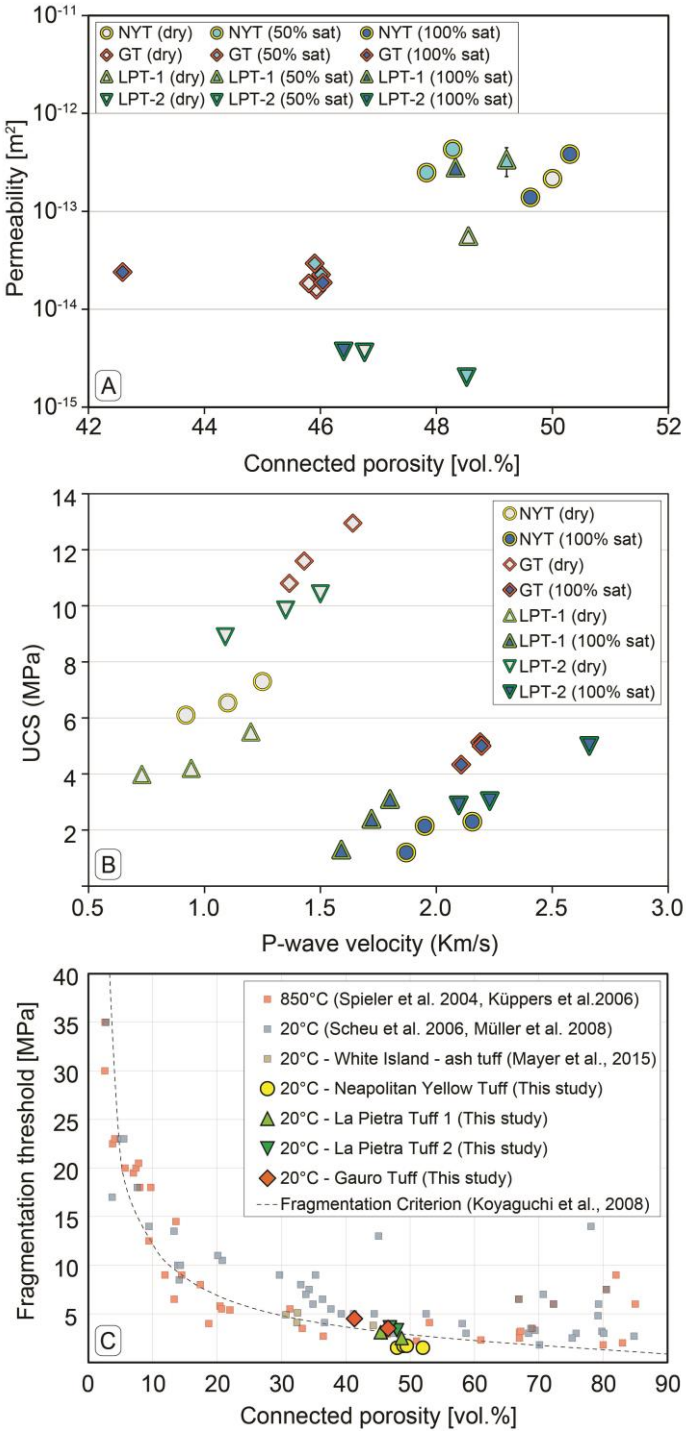


Figure 5.4 Plot of permeability against porosity of the investigated tuffs. Permeability data from this study plot well within three fields defined by i) the highly permeable and porous NYT and LPT-1 samples, ii) the intermediate permeability and low porosity GT samples, and iii) the very low permeability and intermediate porosity LPT-2 samples (A). Plot of uniaxial compressive strength (UCS) against ultrasonic P-wave velocity showing all of the experimental data. Grey-filled shapes indicate dry samples; blue-filled shapes fully-saturated samples (B). Fragmentation threshold of investigated samples at 20 °C during rapid decompression experiments. Fragmentation threshold for several rocks obtained in other studies are also compiled. The dashed line corresponds to the fragmentation criterion proposed by Koyaguchi et al. (2008). Samples with a higher porosity and lower strenght fragment at a lower initial pore pressure (C).

### 5.5.2 Fragmentation threshold

Experiments determining the fragmentation threshold were repeated at least two times to account for sample heterogeneities. Results are reported in Table 5.1 and Figure 5.4. The more porous NYT and LPT-1 (~48 to 51%) required a lower initial pressures (1.5 to 3.1 MPa) for the full sample fragmentation. By contrast the low and intermediate porous GT and LPT-2 (~41 % to 48%) fragmented at higher initial pressures (3.3 to 4.5 MPa). The results are in agreement with the fragmentation threshold defined in previous studies (Spieler et al., 2004b) with NYT and LPT-1 plotting slightly below the fragmentation criterion (Koyaguchi et al. 2008).

### 5.5.3 Explosive energy at experimental conditions

In general the dry conditions resulted to be less powerful (54 to 64.4 J). In the case of partially saturated conditions the energy source is a combination of AE and SF; a lower energetic contribution is estimated for the AE (27.2 to 31.5 J) then for the SF component (319.6 to 370.3 J). The fully saturated conditions instead produced the most energetic explosions (581.8 to 698.3 J).

In the following, the estimated energy are expressed per unit volume of fluid prior to explosive failure, and are used to discuss the energies for the different samples (Table 5.2):

1) The NYT with an open porosity of 50%, accounted for an energy release of 2.3 $MJ/m^3$ for the dry case. Under partially saturated condition, and for samples with an effective porosity of 23.9-24.1% that retained 6 to 6.4 g of water, an energy release of 12.9 to 13.9 $MJ/m^3$is calculated. The 11.5-12.6 g of water retained under fully saturated conditions, equates to an energy release of 23.7 to 24.8 $MJ/m^3$.

2) The GT with an open porosity range of ~45. 9%, allowed for an energy release of 2.1 $MJ/m^3$ under dry conditions. For the partially saturated case an effective porosity of 23%, with samples retaining 6.1 to 6.3 g of water, an energy release 12.5-13.6 $MJ/m^3$ is estimated. Under fully saturated conditions the 11-11.9 g of trapped water permitted an energy release of 20.4 to 23.2 $MJ/m^3$.

3) The LPT-1 with its 48.3% connected pore volume, allowed an energy release of 2.2 $MJ/m^3$ in the dry case. Under a partial saturation condition, the 24.6% effective porosity together with the 6.9 g of retained water allowed an energy release of 14 $MJ/m^3$. In case of fully saturated samples, 13.6 g of pore water accounted for an energy release of 26.3 $MJ/m^3$.

4) The LPT-2 with its 46.8% connected pore volume, accounted for a volumetric energy release of 2.1 $MJ/m^3$ in the dry case. For partial saturation condition, an effective porosity of 24.3% and 7 g of retained water equates to an energy release of 14 $MJ/m^3$. Under fully saturated conditions, 13.2 g of pore water permitted for an energy release of 23.9 $MJ/m^3$.

Figure 5.5 shows the relationship between the estimated energy per unit volume in function of porosity which characterizes the different investigated tuffs. Although all three data sets exhibit some scattering due to the natural variability of the tuff core sample a positive correlation between explosive energy (and therefore on the initial degree of

saturation) with sample porosity can be observed. Thus the surplus of available energy in presence of SF allows for 1) a shift of grain towards finer size, with the production of larger amounts of very fine material (Sec.5.5.4) 2) a faster fragmentation (Sec.5.5.5), and 3) a higher ejection speed (Sec.5.5.6).

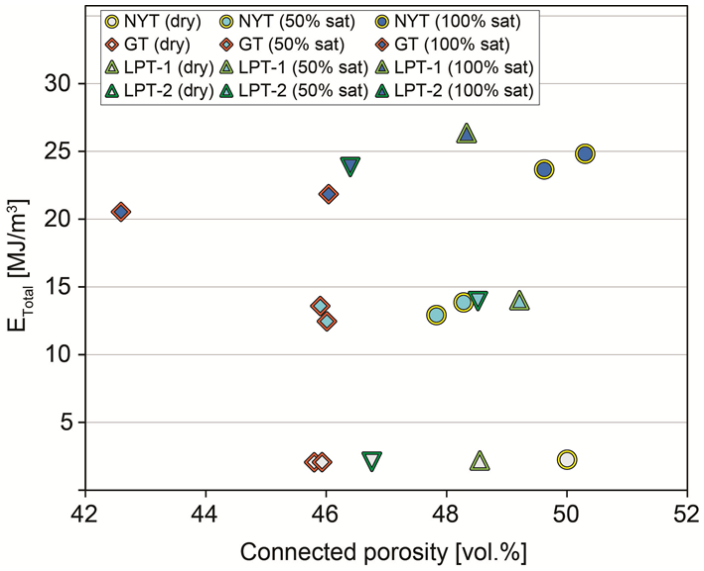


Figure 5.5 Explosive energy per unit volume as function of samples porosity estimated for the different experimental conditions (dry, 50% and 100% saturation). Generally the energy increases with both porosity, and increased amount of liquid water within pore space.

### 5.5.4 Grain size distribution

All experiments were performed at initial pressure of 4.5 MPa, which is well above the fragmentation threshold for samples. The total frequency distributions for the different tuffs, obtained by summing the weight for each experiment in dry, partially and fully-saturated condition, are shown in Figure 5.6. Table 5.2 displays the graphic median diameter (Md$\phi$), sorting ($\sigma$), and the weight percent of fines (>4$\phi$) for each experiment (also shown in Figure 5.7). Generally for volcanic rocks the grain size distribution is shifted towards fines with increased energy for fragmentation (Spieler et al. 2003; Kueppers et al. 2006). The following characteristics of the four sets have been observed:

1) NYT: for these highly porous samples (up to 50.3%) the coarsest grain size distribution (Md -0.9$\phi$) results from dry conditions, with partial (-0.4$\phi$) and fully water saturated conditions (0.6 to 0.9$\phi$) showing progressively finer overall grainsize. A poorly to very poorly sorted distribution (1.7 to 2$\sigma$) characterize the produced fragments at all conditions. Fines (>4$\phi$) production increased from 2.9% for the dry case, to 7.8-9.6% for the partial and 5.6-9.9% for fully water saturated ones.

2) GT: for these low porous samples (Table 5.2) the AE causes a very coarse grain size distribution (Md -1.4 to -0.9$\phi$), whereas partial (0.2 to 0.3$\phi$) and fully water saturated conditions (0.6$\phi$) generate smaller particles. A poorly sorted distribution (1.5 to 1.6$\sigma$) of the fragmented material results from all the experiments. All conditions produced few fines

(>4ϕ), with 2.5 wt% resulting from the dry case, 5.4-6.6wt% from partial and 3.9-4.9wt% from fully water saturated case.

3) LPT-1: as for the NYT, samples from this series are quite porous (up to 49.2%). A coarse grain size distribution, with a median diameter of -1.5ϕ, resulted from the dry experiment, but finer overall clast size are produced under partial and fully water saturated conditions (Md 0.9ϕ). A poorly sorted distribution (1.3 to 1.6σ) of the fragmented material results from all the conditions. In the case of fines (>4ϕ), dry conditions produced 2.9 wt%, while partially generated 10 wt% and fully water saturated conditions 5.6wt%.

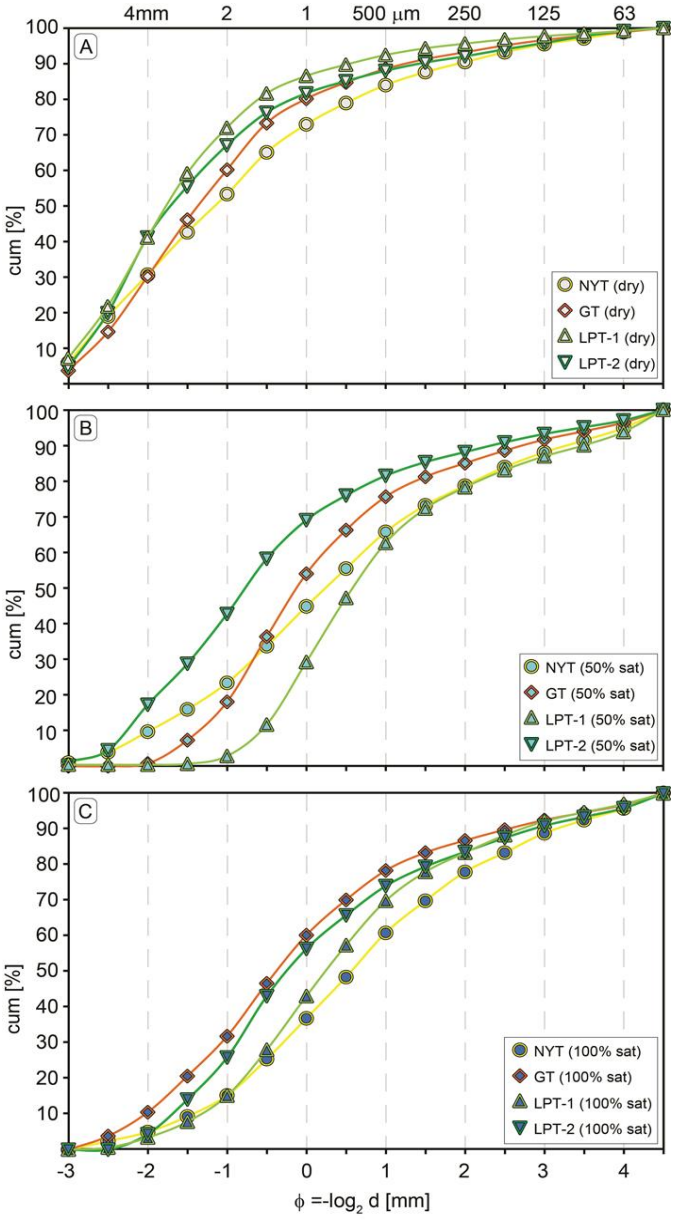


Figure 5.6 Cumulative grain size distribution (GSD) plots showing the weight fractions of particles after rapid decompression experiments at 250 °C and 4.5 MPa in phi steps (phi=−log2d, with d=particle diameter in mm), and in mm scale. From dry (A), to 50% (B), and 100% saturation (C) conditions, the average particle size is decreasing in all plots (more information in the text).

4) LPT-2: these samples also produced a very coarse grain size distribution under dry conditions (Md -1.3ϕ), which progressively decreases for the partially (-0.5ϕ) and fully water saturated (0ϕ) cases. A poorly sorted distribution (1 to 1.6σ) characterize the produced fragments at all conditions. LPT-2 produced a minor amount of fine material (>4ϕ) compared to the LPT-1, with a weight percent of 2.3% generated by the AE, and 4.9 % resulting from both partially and fully-saturated conditions.

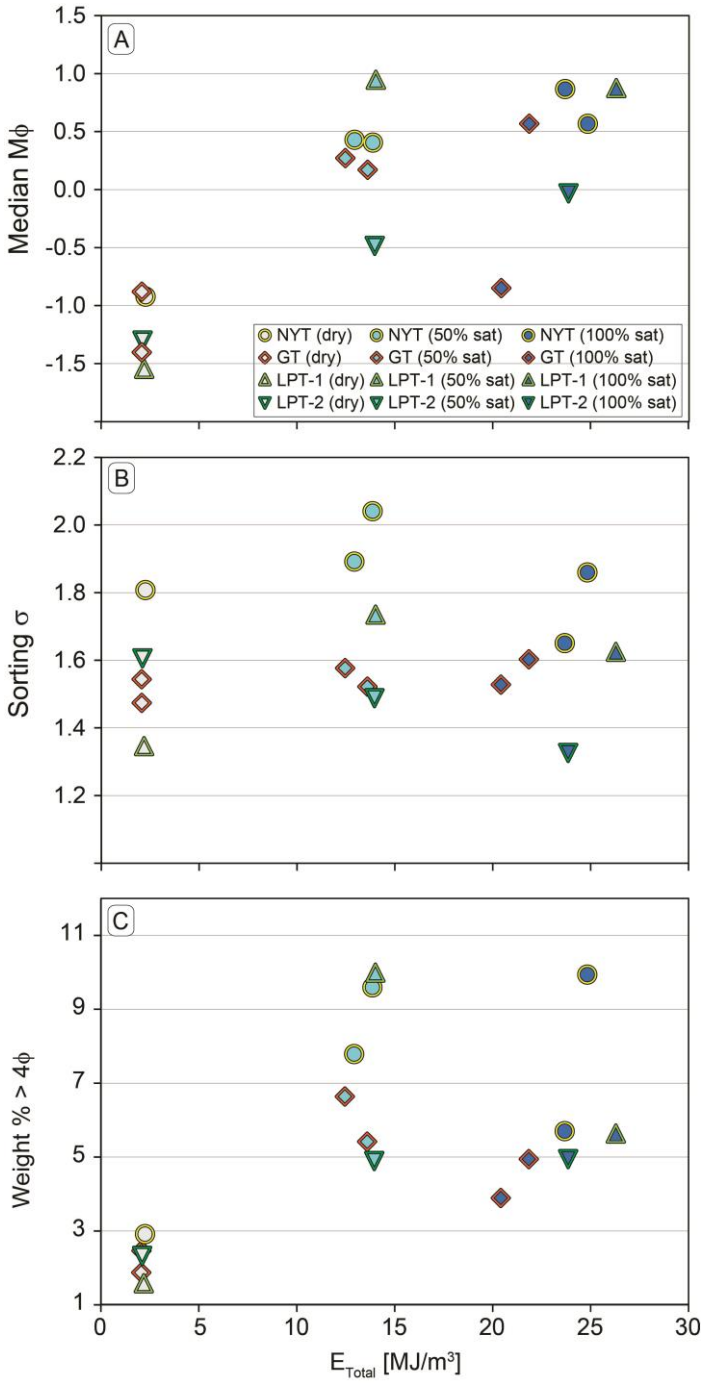


Figure 5.7 Median Mdϕ (A), particles sorting (B), and weight % of fines (C) as function of the volumetric energy for the different experimental conditions (dry, 50% and 100% saturation). Highest values of Mdϕ, σ and weight of fine (>4ϕ) are reached already for the partial saturation condition, and no further increase is observed for the full saturated samples.

### 5.5.5 Fragmentation speed

The fragmentation speed was measured for all samples and under all conditions. Mean values are reported in Table 5.2 and plotted as function of the explosive energy in Figure 5.8A. Fragmentation speeds resulting from SF experiments show a broad range of values depending on the initial degree of sample saturation as well as sample type. The following observations could be made for the three groups of condition:

1) dry conditions: fragmentation is driven purely by AE. The obtained speed values in this case are generally low. The NYT (9 m/s) and LPT-1 (8 m/s) show the fastest fragmentation speed with respect to GT (4 to 6 m/s) and LPT-2 (6 m/s).

2) Partial water saturation (50%): fragmentation is driven by AE mixed with SF. In this case slightly faster fragmentation speed values, with respect to dry conditions, are obtained for NYT (12 to 14 m/s), LPT-1 (13 m/s), LPT-2 (10 m/s), and GT (7 m/s).

3) Full water saturation (100%): fragmentation is driven by solely SF. In this case the fragmentation speed is significantly higher than for partially water saturated and dry experiments. The NYT (55 to 56 m/s) and LPT-1 (54 m/s) show the higher fragmentation speeds in comparison to the GT (23 to 33 m/s) and LPT-2 (39 m/s). The quite low fragmentation for one of GT sample can be explained by its low porosity (42.6%).

The scattering of the obtained velocities is mainly due to the natural variability of the sample's petrophysical properties. The errors for the fragmentation speed values are in the range between -2.4 to +9.8 m/s, and are reported in Table 5.2.

### 5.5.6 Ejection velocities

Particle ejection velocities were computed from the displacements of individual particles tracked across five successive frames of the high-speed footage. The errors for the ejection velocities are in the range of ±22 m/s, and also reported in Table 5.2. An average speed of those particles at the absolute flow front was calculated using (≥ 5) particle velocities (Mayer et al., 2015). The velocities thus obtained are an approximation of the true maximum velocity, since the images are 2-D renderings, perpendicular to the line of sight. Generally the ejection velocities show dependencies on the energy source, and therefore on the initial degree of saturation (Figure 5.8B).

In particular, the more porous NYT particles show the highest speed under dry (148 m/s), partially (208 to 222 m/s), full water saturation conditions (243 to 291 m/s). For the GT ejection velocities increased from dry (114 to 141 m/s), to partially (176 to 177 m/s), and full water saturated samples (194 m/s). A very low ejection velocity of 137 m/s was measured for one very low porosity sample at fully saturated conditions. Despite the relatively high explosive energy estimated for LPT-1, quite low ejection velocities have been measured for dry (134 m/s), partially (170 m/s), and fully water saturated conditions (175 m/s). For the LPT-2 instead, velocities increase from dry (145 m/s) to partial (198 m/s) and fully water saturated conditions (197 m/s).

**Table 2.** Sample properties and experimental results for dry, partially and fully saturated conditions. All experiments were run at 250°C and 4.5 Mpa.

| Sample | Mass [g] | $H_2O$ added [g] | $V_{calc.}$ [$cm^3$] | $\rho_{calc.}$ [$g/cm^3$] | $V_{meas.}$ [$cm^3$] | $\rho_{meas.}$ [$g/cm^3$] | Conn. porosity [%] Total | Effective | Permeability ($S_{dev}$) [$m^2$] | | $E_{expl-R}$ [J] | $E_{expl-I}$ [J] | $E_{unit\ Vol}$ [$MJ/m^3$] | $v_{Frag}$ [m/s] | (±Err) | $v_{Eject}$ [m/s] | (±Err) | Wt % > 4 ϕ | Mdϕ | Sorting σ |
|---|---|---|---|---|---|---|---|---|---|---|---|---|---|---|---|---|---|---|---|---|
| *Argon expansion* | | | | | | | | | | | | | | | | | | | | |
| NYT | 33.4 | | 28.6 | 1.2 | 14.3 | 2.3 | 50 | | 2.2E-13 | (3.5E-14) | 64.4 | | 2.3 | 9 | (+1.5) | 148 | (±5) | 2.9 | -0.9 | 1.8 |
| GT | 35.5 | | 27.9 | 1.3 | 15.1 | 2.3 | 45.8 | | 1.8E-14 | (3.2E-16) | 57.4 | | 2.1 | 6 | (-1.8) | 114 | (±2.6) | 1.9 | -1.4 | 1.5 |
| GT | 34.8 | | 27.1 | 1.3 | 14.6 | 2.3 | 45.9 | | 1.6E-14 | (3.5E-16) | 55.9 | | 2.1 | 4 | (-0.4) | 141 | (±6.1) | 2.5 | -0.9 | 1.5 |
| LPT-1 | 29.7 | | 24.7 | 1.2 | 12.7 | 2.3 | 48.6 | | 5.6E-14 | (4.5E-15) | 54 | | 2.2 | 8 | (+1.3) | 134 | (±3.8) | 1.6 | -1.5 | 1.3 |
| LPT-2 | 35.2 | | 28.4 | 1.2 | 15.1 | 2.3 | 46.8 | | 3.6E-15 | (1.2E-16) | 59.8 | | 2.1 | 6 | (+1.3) | 154 | (±2.5) | 2.3 | -1.3 | 1.6 |
| *Steam flashing (50% sat.)* | | | | | | | | | | | | | | | | | | | | |
| NYT | 33.3 | 6.4 | 28.4 | 1.2 | 14.8 | 2.2 | 47.8 | 23.9 | 2.5E-13 | (3.1E-14) | 30.6 | 336.5 | 12.9 | 12 | (+3) | 208 | (±21.1) | 7.8 | 0.4 | 1.9 |
| NYT | 28.5 | 6 | 25 | 1.1 | 12.9 | 2.2 | 48.3 | 24.1 | 4.3E-13 | (4.7E-14) | 27.2 | 319.6 | 13.9 | 14 | (-2.8) | 222 | (±6.8) | 9.6 | 0.4 | 2.0 |
| GT | 35.8 | 6.1 | 28.1 | 1.3 | 15.1 | 2.3 | 46 | 23 | 2.3E-14 | (7.0E-16) | 29 | 320.3 | 12.5 | 7 | (+1) | 176 | (±8.4) | 6.6 | 0.3 | 1.6 |
| GT | 33.8 | 6.3 | 26.7 | 1.3 | 14.4 | 2.3 | 45.9 | 23 | 2.9E-14 | (8.7E-16) | 27.6 | 335.2 | 13.6 | 7 | (-1.4) | 177 | (±8) | 5.4 | 0.2 | 1.5 |
| LPT-1 | 33.6 | 6.9 | 28.4 | 1.2 | 14.4 | 2.3 | 49.2 | 24.6 | 3.4E-13 | (1.1E-13) | 31.5 | 366.7 | 14 | 13 | (-2.2) | 170 | (±13.7) | 10 | 0.9 | 1.7 |
| LPT-2 | 34.8 | 7 | 28.8 | 1.2 | 14.8 | 2.3 | 48.5 | 24.3 | 2.0E-15 | (4.3E-17) | 31.4 | 370.3 | 14 | 10 | (-1.6) | 198 | (±22.7) | 4.9 | -0.5 | 1.5 |
| *Steam flashing (100% sat.)* | | | | | | | | | | | | | | | | | | | | |
| NYT | 32.9 | 12.6 | 28.3 | 1.2 | 14.3 | 2.3 | 49.6 | 0 | 1.4E-13 | (6.5E-15) | | 669.4 | 23.7 | 55 | (+1.2) | 243 | (±6.1) | 5.7 | 0.9 | 1.7 |
| NYT | 26.7 | 11.5 | 24.6 | 1.1 | 12.2 | 2.2 | 50.3 | 0 | 3.9E-13 | (4.1E-14) | | 611.3 | 24.8 | 56 | (+9.8) | 291 | (±8.4) | 9.9 | 0.6 | 1.9 |
| GT | 33.2 | 11 | 28.5 | 1.3 | 14.8 | 2.2 | 42.6 | 0 | 2.4E-14 | (1.9E-15) | | 581.8 | 20.4 | 23 | (-2.4) | 137 | (±12.9) | 3.9 | -0.8 | 1.5 |
| GT | 34.7 | 11.9 | 27.2 | 1.3 | 14.7 | 2.1 | 46 | 0 | 1.9E-14 | (8.0E-16) | | 631.7 | 23.2 | 33 | (-0.4) | 194 | (±10.6) | 4.9 | 0.6 | 1.6 |
| LPT-1 | 34.1 | 13.6 | 27.5 | 1.2 | 14.2 | 2.4 | 48.3 | 0 | 2.8E-13 | (3.4E-14) | | 722.6 | 26.3 | 54 | (+5.7) | 175 | (±8.2) | 5.6 | 0.9 | 1.6 |
| LPT-2 | 35.7 | 13.2 | 29.3 | 1.2 | 15.7 | 2.2 | 46.4 | 0 | 3.7E-15 | (1.9E-17) | | 698.3 | 23.9 | 39 | (-2.3) | 196 | (±11.4) | 4.9 | 0 | 1 |

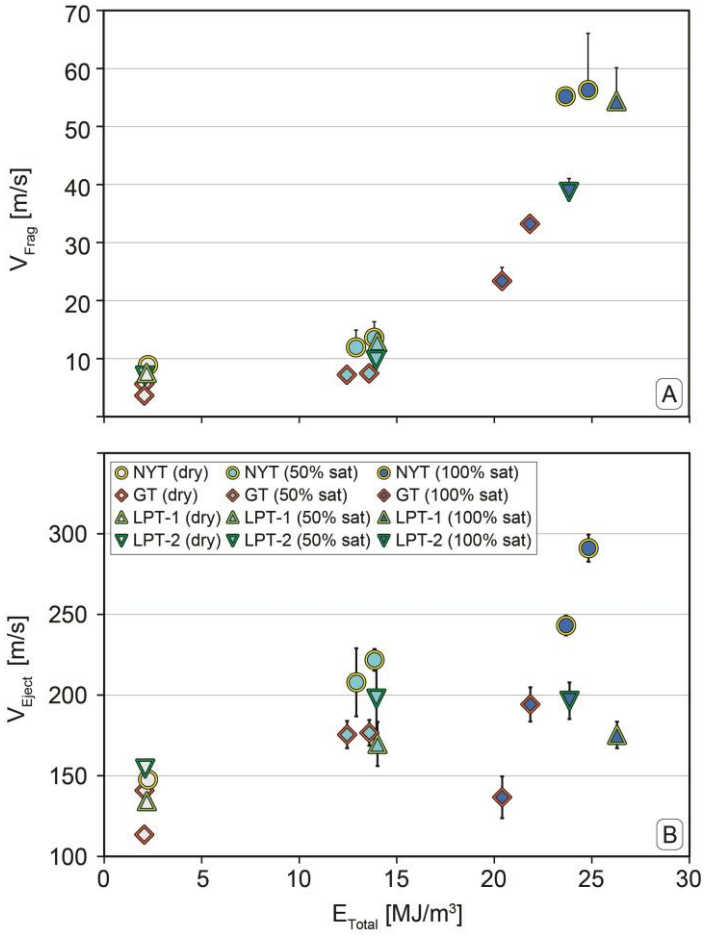


Figure 5.8 Evaluation of fragmentation speed (A), and ejection velocity (B) as function of the volumetric energy for the different experimental conditions (dry, 50% and 100% saturation). An increase in fragmentation speed and ejection velocities of particles occurs from dry to fully water saturated conditions.

## 5.6 Discussion

If a magmatic or hydrothermal system is affected by steam-driven eruptions, their explosivity depends on pressure, temperature and fluid saturation of the host rock, as well as on rock properties. In this study it has been attempted to quantify the role of the liquid fraction as well as rock porosity, permeability and strength, on the explosive power by applying a combination of experimental volcanology and simple thermodynamic modelling. A scenario likely for steam-driven eruptions at the Solfatara and Pisciarelli (Campi Flegrei) has been investigated, by simulating a decompression event initiating within the shallow part of the underlain hydrothermal system. Results show that the initial liquid fraction, together with the host rock porosity and permeability affects 1) the amount of explosive energy, 2) the size distribution and 3) the fragmentation and ejection behavior of the investigated tuffs. The rock strength instead has a secondary effect on the fragmentation and ejection behavior.

### 5.6.1 Effect of liquid fraction

Steam-driven eruptions are common in many volcanic terrains as well as other areas of high heat flow, where depressurization may involve high-temperature and liquid-dominated hydrothermal reservoirs. For the known cases a maximal focal depth of the explosion have been estimated up to 450 meters, where incipient boiling occur at 260 °C and 4.5 MPa (Browne and Lawless 2001). Many hydrothermal eruptions, on a wide range of size, are thought to initiate very close to the ground surface, where a flashing front generates due to local perturbations (seismic activity, pressure reduction by landslide, lake drainage, etc.), and migrates downwards into the reservoir (Browne and Lawless 2001; Montanaro et al. 2016). The presence of dissolved gas in the liquid mainly controls the boiling temperature and thus the depth of initial flashing (McKibbin 1996), not affecting the front-migration mechanism. However dissolved gas may add to the energy available in a geothermal fluid (Nelson and Giles 1985). An experimental temperature of 250°C and a pressure of 4.5 MPa have been used in this study. For this condition water remains in the liquid state, yet very close to the boiling-point. The Argon gas used to pressurized the system (see Sec. 5.4.1.2), is not expected to significantly dissolve in the liquid water. Notably for the experimental conditions the liquid-vapour phase boundary is crossed very quickly if a sudden decompression of the system occurs (Figure 5.3). Consequently, only a limited expansion of the gas within the (effective) pore space may contribute to a fragmentation process dominated by SF over the AE.

According to the results, eruptions accompanied by an increasing amount of water flashing to steam are significantly more violent that those driven purely by gas expansion. From dry to partial and fully saturated conditions, an increase in explosive energy per unit volume from ~2 to ~14 and ~26 MJ/m$^3$, respectively, has been estimated. Thus compared to AE, the amount of available energy associated to SF is of one order of magnitude higher.

### 5.6.2 Effect of rock porosity and permeability

The heterogeneous tuff samples used in this study show a range of porosity from 42.6 and 50.3%, and a range of permeability from $2\times10^{-15}$ to $4.3\times10^{-13}$ m$^2$. The host-rock reservoir of the hydrothermal system below Solfatara crater is thought to be built of similar tuff deposits (Sec.5.3.1). The same lithologies have also been described as lithic components within the deposits of the phreatic phase accompanying the formation of Solfatara crater itself (Isaia et al. 2015).

A decompression event (e.g., fracturing, variance in the groundwater level) may trigger explosive vaporization of water, or disrupt the stress equilibrium between the pressurized gas phase and its surrounding rocks. In such a case, porosity and permeability of rocks are key factors in controlling the explosive behavior of a hydrothermal system (Mueller et al. 2011). The former controls the amount of fluid stored and therefore the energy available for release during fragmentation for a given decompression step (Alatorre-Ibargüengoitia et al. 2010). The latter determines if the expanding fluid may either fragment the

surrounding rocks or escape from it via effective outgassing along an existing network of cracks and interconnected pores (Scheu et al. 2006; Mueller et al. 2008; Richard et al. 2013). Both properties are in turn affecting the fragmentation behavior (Mueller et al. 2008).

Under the experimental conditions, explosive energy increases with water content and porosity (Table 5.2 and Figure 5.5). All investigated tuffs show a permeability below the cut-off value of $10^{-12}$ $m^2$ described by Mueller et al.(2008). Accordingly the fragmentation process should not be affected by pressure loss through fast outgassing during the decompression.

### 5.6.3 Fragmentation behavior

The energy surplus due to an increasing amount of water has the ability to decrease the average grain size, and enhance the production of very fine particles (Figure 5.7; Rager et al., 2014). A clear shift towards finer grain size is represented by the variation of the median diameter (Md$\phi$ in Figure 5.7A). The produced material is generally poorly to very poorly sorted (1 to 2$\sigma$), with the NYT showing a very broad distribution across all experimental conditions (Figure 5.7B). A significant increase in the amount of the very fine fraction (>4$\phi$) is observed for samples fragmenting under partial and full water saturated conditions, in particular for the highly porous NYT and LPT-1 samples (Figure 5.7C).

In general the highest values of median diameter, weight of fine (>4$\phi$), and (subordinately) sorting, are reached for the partial saturated conditions, whereas no further increase is observed for fully saturated samples. It is noteworthy that the median diameter and the amount of very fine (>4$\phi$) are not further increased under the full water saturation condition. This result may depend from both the experimental conditions (see Sec. 5.6.1) and sample properties. Despite the increase in liquid fraction, the released energy may not be enough to increase the amount of fine production (Kueppers et al. 2006).

### 5.6.4 Fragmentation speed and ejection behavior

Both the fragmentation speed and ejection velocity are controlled by the initial overpressure within the pores, the connected porosity, the permeability, and the strength of the sample (Scheu et al. 2006; Richard et al. 2013). In this study it has been demonstrated that the decompression of liquid water plays a further key role (Rager et al. 2014; Mayer et al. 2015). The produced experimental decompression, from 4.5 MPa to ambient pressure, results in the flashing and expansion of superheated water (250°C). This causes an about 40-fold larger volume increase with respect to pure AE under same conditions. Thus the presence of SF is additionally enhancing the gas expansion which powers the fragmentation processes (Mastin 1995; Mayer et al. 2015),accounting for an increase in energy and in turn for a faster ejection of particles (Figure 5.8; Alatorre-Ibargüengoitia et al., 2011).

In particular, and in agreement with results from previous investigations (Mayer et al. 2015), a drastic increase in fragmentation speed (up to 56 m/s) occurs from dry to fully water saturated samples. Whereas from dry (9 m/s) to partial water saturation instead (14 m/s) only a slight increase in speed is observed. The ejection velocities of the particles increases as well from dry (max 154.5 m/s) to partially (max 222 m/s) and fully saturated conditions (max 291 m/s).

For all experimental conditions the NYT samples yielded the highest fragmentation speeds and particles ejection velocities, most possibly due to their high porosity (up to 50.3%). Their low sample strength further contributes to a lower fragmentation threshold (1.5-1.7 MPa), which implies that less energy is consumed by fragmentation, thus more energy remains to expel the fragments (Alatorre-Ibargüengoitia et al. 2010).

## 5.7 Conclusions

Rapid decompression experiments were conducted on heterogeneous tuffs from the Campi Flegrei caldera, characterized by a range of petrophysical properties. The experiments were designed to mimic a steam-driven explosive event by rapid depressurization of fluids within the rock pore space. The influence of the liquid fraction, as well as of the rock properties, on the explosive power and in turn on the fragmentation and ejection behavior was explored. The comparison of the experimental results with thermodynamic modelling based on an irreversible approach allowed to estimate the explosive energy released. At initial conditions of 250 °C and 4.5 MPa, rapid decompression to atmospheric pressure triggered fluid (AE and/or SF) expansion, rock fragmentation and ejection of particles. The findings indicate that:

1) the increasing liquid fraction within the pore space increases the explosive energy; for the fully saturated condition the energy released by SF can be estimated to be one order of magnitude higher than for the solely AE;
2) the released energy increases with sample porosity, and is not dissipated through (rapid) outgassing during the fragmentation as all tuffs are low permeable;
3) the energy surplus in the presence of SF leads to an increased fragmentation speed and a higher ejection velocity of the fragmented particles;
4) the vaporization occurring under 50% water saturation conditions has the ability to increase the degree of fragmentation and to decrease the average ejecta size;
5) the material strength showed a secondary, but observable effect on the fragmentation behavior for the investigated tuffs.

An increased liquid fraction during decompression together with the rock porosity are important fragmentation variables that should be considered for modelling of steam-driven eruptions in hydrothermally active environments. On the other hand strength and rock texture may affect the rate of energy release and need further investigations. Overall, a potential hazard may be associated to destabilisation of a hydrothermal systems under conditions including temperatures >250$^{o}$ C, rock porosity >40% and small fraction of water in a liquid state, yet close to the boiling point.

This page was intentionally left blank.

# *Chapter 6*

## *Conclusions and outlook*

*"I wish it need not have happened in my time," said Frodo.*

*"So do I," said Gandalf, "and so do all who live to see such times.*
*But that is not for them to decide. All we have to*
*decide is what to do with the time that is given us."*

*The Fellowship of the Ring (1954)*
*J.R.R. Tolkien*

I INVESTIGATED THE EXPLOSIVITY OF STEAM-DRIVEN ERUPTIONS IN VOLCANIC SYSTEMS by using a multidisciplinary approach, which involved field-based studies, together with laboratory and theoretical studies.

Steam-driven eruptions are a very complex type of explosive event, and despite their frequent occurrence many questions remain still open, particularly concerning the parameters controlling their violence (or explosive power). The violence depends largely on the different explosivity of fluids (liquid or gaseous) driving them, as well as on the rate of mechanical energy release. Both factors are in turn controlled by 1) the pore liquid fraction and its physical condition (pressure-temperature) before an explosive event, and 2) the lithology and the petrophysical properties (mainly porosity, permeability and strength) of the host medium. A wide range of initial temperature, pressure and liquid fraction, as well as a variety of lithotypes characterize the volcanic environments affected by steam-driven eruptions, and consequently they show a wide range of eruptive styles.

A multidisciplinary approach as a tool to characterize the explosivity of steam-driven eruptions may provide many estimates on the controlling parameters. Field data (e.g. deposit volume, thickness, area, etc.) are a solid base which allow to define the boundary conditions for the application of both experimental and theoretical methods. Natural samples to be used for decompression experiments under controlled conditions (pressure, temperature, liquid fraction, etc.), permit to further estimate the energetic parameters of steam-flashing processes. Finally the energy associated to the steam flashing can be assessed via thermodynamic modelling based on an isenthalpic (irreversible) approach. This method results in a more realistic estimation of explosive energy. A comparison of these estimated energies with those obtained from other independent methods (craterization energy, seismic energy, etc.) could be of further help to define the energy portioning.

To unravel the parameter controlling the energetics of the steam-driven eruptions a multidisciplinary approach has been used to investigate two recent hydrothermal explosive events. These represented two end-member case for steam-driven eruptions, and their characteristics as well as findings from their study are the following:

***i) Small hydrothermal explosions:*** consist in jetting of hydrothermal fluids (steam, water) and substantial amounts of solid material (mud and rock fragments). Such events can last few seconds to minutes, and produce craters spanning from a few meters up to hundreds of meters in diameter. The crater depths range from few meters to several hundred meters and strongly dependent on host rock composition. Ejected debris may reach velocities of few tens of m/s, and usually produce low volume deposits. These are generally very-poorly sorted, and matrix-supported. For example the Gengissig hydrothermal explosions, triggered by a lake drainage, occurred within loose material and produced limited deposits (~0.3 $km^2$) around craters having tens of meter in size. Field mapping of the ejected debris allowed to estimate mass and volume of the deposit, providing a robust estimate on the energies released during such small-sized explosions. Loose sediments saturated with water close to the boiling point (~125°C), experienced a relatively small pressure drop of 0.2 MPa, which resulted in the explosive boiling of water. In this specific case the presence of loose altered material, interbedded with very low permeable clay-rich levels appears to control the explosion dynamics and energy partitioning. While the low permeability layers account for the over-pressurization and failure of the system, the loose material played a key role permitting an efficient conversion of the available thermal energy into craterization (30%) and kinetic energy (12%).

***ii) Large hydrothermal eruptions:*** similar to those at Mt. Ontake in Japan (Yamamoto, 2014), and Ruapehu, in New Zealand (Kilgour et al., 2010) involve different mechanisms (magma fluid injection, hydrothermal sealing, etc.) and also larger volumes (~$10^5$ $m^3$), durations, products and types of confining rock. Another example of large hydrothermal eruptions is the Upper Te Maari eruption, representing the more violent end-member case studied in this work. Triggered by a landslide, this eruption excavated a 430-m-long fissure within heterolithic rocks, and produced a pyroclastic density current as well as an ash plume and the launch of ballistics. The latter covered a large area (~5.1 $km^2$) around the vents. Field mapping and laboratory studies allowed to characterize the lithology and porosity of the source rock of this ballistics. Both a liquid- and vapor-dominated hydrothermal reservoir were thought to be seated below the crater area providing the energy source for the eruption. Decompression experiments were performed on samples from the source rock to explore the influence of initial pressure and temperature, as well as the effect of their very heterogeneous nature, on the explosive energy. Experimental outcomes contribute to field- and modelling findings and demonstrate the highly energetic steam flashing of liquid water is more likely to explain the observed eruption. Rocks with relatively high porosity appear to have enhanced the explosive energy and have favoured the fragmentation processes by sustaining the eruption. By contrast the involvement of very low porous and denser rocks, or a more steam-dominated region, would have led to a rapid waning or caused the eruption to cease.

Additionally to these case studies, I conducted an experimentally-based investigation of the influence of liquid fraction and rock petrophysical properties on the steam-driven explosive energy. For this study, a series of fine-grained heterogeneous tuffs from the Campi Flegrei caldera were investigated for their petrophysical properties. Decompression experiments simulate a scenario likely for a steam-driven eruption involving the shallow part of the hydrothermal system. The rapid depressurization of various amount of liquid water within the rock pore space produced a different fragmentation and ejection behavior for the investigated tuffs. Porosity and permeability of the tuffs have strongly affect the amount of available energy, whereas the rock strength has only shown a secondary effect on the fragmentation behavior.

***Main findings***

The pore liquid fraction and its physical conditions (pressure-temperature) investigated in this study, cover a broad range of known steam-driven explosive events. Results from this work indicate that an increasing liquid fraction within the pore space increases the explosive energy. Particularly for the fully water saturated conditions the energy released by steam-flashing can be estimated to be one order of magnitude higher than for the solely (Argon) gas or steam expansion. At constant temperature, an increase in initial pressure (above the boiling point) is not producing a significant increase in explosive energy released by steam-flashing under the investigated conditions. Decompression of a liquid at an initial pressure and temperature close to the boiling-point may result in a higher production of fine material already under partial (e.g. 50%) saturation conditions.

Lithology investigated in this work varies from loose sediments, to very heterogeneous tuff breccias and agglutinates, to fine-grained tuffs, and cover a large spectra of porosity, permeability and rock strength. These parameters control the energy storage, as well as its partitioning in form of fragmentation and particle ejection. In particular the rock's connected porosity relates to the amount of stored energy, with higher porosities accounting for higher energies. This energy surplus, in the presence of steam-flashing, finally leads to an increased fragmentation speed and a higher ejection velocity of the fragmented particles. The maximum result in terms of produced fine is obtained if samples are low permeable ($<10^{-12}$ $m^2$) since in this case the energy is not dissipated through (rapid) outgassing during the fragmentation. In case of loose material, only a minor amount of the explosive energy is consumed by fragmentation, and may be efficiently converted in other forms, such as craterization and kinetic energy. In case of consolidated rocks a secondary, but significant effect of the material strength on the fragmentation behavior has been observed for the investigated samples. Experimental results show that at constant porosity, weaker rocks produce more fine particles than firmly cemented rocks.

## Outlook

The studies discussed in this thesis helped to shed light on some aspects of the complex processes and interplay of various parameters during steam-driven eruptions, in particular concerning their effect on the explosive energy and its partitioning. Though, a number of new questions have arisen concerning i) how to link investigated parameter, and the obtained results, with numerical modeling, ii) what need to be further investigated in terms of host rock properties effect on the fragmentation processes, and iii) what information can be extracted from the steam-driven produced particle in terms of shape and size-distribution.

### *i) Numerical modeling of steam-driven eruptions based on field-lab results.*

*Hydrothermal explosions within loose material*:

Over-pressurization and failure of the system, together with debris ejection may be investigated through modelling by having robust estimation on 1) initial temperature and decompression rate, 2) permeability and thickness of clay-rich levels, 3) volume of ejected debris, particle size distribution and ejection velocity. Yet more constraints would be needed on the reservoir porosity and thus liquid volume. A real-case application, for e.g. to the Gengissig hydrothermal explosions, is already planned in collaboration with Karen Strehlow (Bristol university) and Hannah I. Reynolds (University of Iceland).

*Gas-particle decoupling and ballistic ejection dynamics*:

Based on the experimentally-obtained ejection velocity and particle size distribution a modelling of the flow conditions for particle-gas decoupling depending on size can be attempted. A real-case application, for e.g. the Te Maari eruption, is already planned in collaboration with Mattia De'Michieli Vitturi (INGV Pisa).

### *ii) Host rock properties effect on fragmentation processes.*

*Effects of the initial rock grain and pore size distribution*.

Grain-size distribution of the rock sample prior to experimentation obtained by analyzing thin sections (or high resolution 3-D tomography for fine-grained material) could help to estimate the effect of the pristine structure on the produced grain size. Repeated experiments on identical water-saturated sample series, at increased pressure and temperature (below critical conditions) could be used to explore experimentally the theoretical concept of spinoidal decomposition (Thiéry and Mercury 2009). The use of sample characterized by microporous network, could give insight into the postulated concept of an increased spinoidal instability field with decreasing pore size (Thiéry et al. 2010).

*Effect of gas expansion on the fragmentation process for partially water saturated conditions.*

The study of the fine-grained tuffs showed that partial (50%) water saturation conditions have the ability to increase the degree of fragmentation and to decrease the average ejecta

size, similar to the fully saturated case. For this study the initial pressure was very close to the fragmentation threshold of the sample. Additionally the initial pressure-temperature conditions were close to the boiling-point. Thus for partially saturated samples a limited expansion of the gas within the (effective) pore space may contribute to a fragmentation process dominated by steam-flashing over the argon expansion. Experiments with different degree of water saturation (25-50-75%) at both room temperature (only gas as fragmenting source) and high temperature (gas expansion plus steam-flashing) could help to evaluate and quantify the effect of gas expansion on the fragmentation process. Together with the different degree of saturation, a wide range of porosity would also help to define thresholds to the gas-driven fragmentation process.

*Fragmentation energy in the presence of steam-flashing.*

The fragmentation threshold of rock samples can be used to assess the minimum amount of energy needed to fully fragment the sample by gas expansion during decompression. This energy can be used to roughly estimate the amount of initial explosive energy consumed by the fragmentation process. Yet a higher initial pressure, or the presence of steam flashing, will increase drastically the amount of available energy, thus more energy can be consumed by fragmentation to create new fracture surfaces. Kueppers et al. (2006) estimate the amount of energy consumed by fragmentation of volcanic rocks based on the analyses of the surface area of experimentally-produced fragments. A similar approach could be used as well to assess the fragmentation energy in the presence of steam flashing.

***iii) Effect of steam-driven fragmentation on the particle shape and size-distribution.***

*Definition of shape parameters for steam-driven generated particles.*

In analogy with technique used for pumice produced by magmatic or phreatomagmatic fragmentation, a particle shape analysis may be used to 1) distinguish between different 'components' (i.e. between glassy grains and aggregates), to estimate their relative proportions in the deposit, and 2) explore the relationship between particle morphology and the substrate material, for different steam-driven eruption deposits. Use of cross-sectional images may give more information about how the fracturing behaviour relates to the internal particle structure. This method also allows for quick analyses of large numbers of grains to quantitatively determine the proportions of different components (for e.g. the proportion of glassy to aggregated grains in the samples). If parameters can be defined, experimental study could further help to understand which mechanism amongst gas or steam expansion, as well as steam flashing, may produce such a shape.

This page was intentionally left blank.

# *References*


Alatorre-Ibargüengoitia M a., Scheu B, Dingwell DB, et al (2010) Energy consumption by magmatic fragmentation and pyroclast ejection during Vulcanian eruptions. Earth Planet Sci Lett 291:60–69. doi: 10.1016/j.epsl.2009.12.051

Alatorre-Ibargüengoitia M a., Scheu B, Dingwell DB (2011) Influence of the fragmentation process on the dynamics of Vulcanian eruptions: An experimental approach. Earth Planet Sci Lett 302:51–59. doi: 10.1016/j.epsl.2010.11.045

Alidibirov M, Dingwell DB (1996) An experimental facility for the investigation of magma fragmentation by rapid decompression. Bull Volcanol 58:411–416.

Alidibirov M, Dingwell DB (2000) Three fragmentation mechanisms for highly viscous magma under rapid decompression. J Volcanol Geotherm Res 100:413–421. doi: 10.1016/S0377-0273(00)00149-9

Barberi F, Bertagnini a., Landi P, Principe C (1992) A review on phreatic eruptions and their precursors. J Volcanol Geotherm Res 52:231–246. doi: 10.1016/0377-0273(92)90046-G

Barberi F, Corrado G, Innocenti F, Luongo G (1984) Phlegraean Fields 1982-1984: Brief chronicle of a volcano emergency in a densely populated area. Bull Volcanol 47:175–185. doi: 10.1007/BF01961547

Breard ECP, Lube G, Cronin SJ, et al (2014) Using the spatial distribution and lithology of ballistic blocks to interpret eruption sequence and dynamics: August 6 2012 Upper Te Maari eruption, New Zealand. J Volcanol Geotherm Res. doi: 10.1016/j.jvolgeores.2014.03.006

Breard ECP, Lube G, Cronin SJ, Valentine GA (2015) Transport and deposition processes of the hydrothermal blast of the 6 August 2012 Te Maari eruption, Mt. Tongariro. Bull Volcanol 77:100. doi: 10.1007/s00445-015-0980-5

Browne PRL, Lawless J V. (2001) Characteristics of hydrothermal eruptions, with examples from New Zealand and elsewhere. Earth Sci Rev 52:299–331. doi: 10.1016/S0012-8252(00)00030-1

Bruno PPG, Ricciardi GP, Petrillo Z, et al (2007) Geophysical and hydrogeological experiments from a shallow hydrothermal system at Solfatara Volcano, Campi Flegrei, Italy: Response to caldera unrest. J Geophys Res Solid Earth 112:1–17. doi: 10.1029/2006JB004383

Büttner R, Dellino P, Zimanowski B (1999) Identifying magma–water interaction from the surface features of ash particles. Nature 401:688–690. doi: 10.1038/44364

Byrdina S, Vandemeulebrouck J, Cardellini C, et al (2014) Relations between electrical resistivity, carbon dioxide flux, and self-potential in the shallow hydrothermal system of Solfatara (Phlegrean Fields, Italy). J Volcanol Geotherm Res 283:172–182. doi: 10.1016/j.jvolgeores.2014.07.010

Caliro S, Chiodini G, Moretti R, et al (2007) The origin of the fumaroles of La Solfatara (Campi Flegrei, South Italy). Geochim Cosmochim Acta 71:3040–3055. doi: 10.1016/j.gca.2007.04.007

Caliro S, Chiodini G, Paonita a. (2014) Geochemical evidences of magma dynamics at Campi Flegrei (Italy). Geochim Cosmochim Acta 132:1–15. doi: 10.1016/j.gca.2014.01.021

Carlino S, Piochi M, Troise C, et al (2016) Small -to- large scale permeability and continuous gradient temperature monitoring of subsurface rocks in volcanic areas: new insights from bore-hole and laboratory analysis at the Campi Flegrei caldera (Southern Italy). In review.

Carrivick JL, Russell AJ, Tweed FS (2004) Geomorphological evidence for jökulhlaups from Kverkfjöll volcano, Iceland. Geomorphology 63:81–102. doi: 10.1016/j.geomorph.2004.03.006

Chiodini G, Avino R, Caliro S, Minopoli C (2011) Temperature and pressure gas geoindicators at the Solfatara fumaroles ( Campi Flegrei ). Ann Geophys 54:151–160. doi: 10.4401/ag-5002

Chiodini G, Frondini F, Cardellini C, et al (2001) CO2 degassing and energy release at Solfatara volcano, Campi Flegrei, Italy. J Geophys Res 106:213–216.

Chiodini G, Vandemeulebrouck J, Caliro S, et al (2015) Evidence of thermal-driven processes triggering the 2005–2014 unrest at Campi Flegrei caldera. Earth Planet Sci Lett 414:58–67. doi: 10.1016/j.epsl.2015.01.012

Choy GL, Boatwright JL (1995) Global patterns of radiated seismic energy and apparent stress. J Geophys Res 100:18205. doi: 10.1029/95JB01969

Choy GL, McGarr A, Kirby SH, Boatwright J (2006) An Overview of the Global Variability in Radiated Energy and Apparent Stress. Earthquakes Radiated Energy Phys Faulting 170:43–57. doi: 10.1029/170GM06

Colella A, Calcaterra D, Cappelletti P, et al (2009) I tufi zeolitizzati nell'architettura della campania. In: La diagnostica per il restauro del patrimonio culturale, Napoli, Cuzzolin,. pp 327–341

Cousins CR, Crawford I a., Carrivick JL, et al (2013) Glaciovolcanic hydrothermal environments in Iceland and implications for their detection on Mars. J Volcanol Geotherm Res 256:61–77. doi: 10.1016/j.jvolgeores.2013.02.009

de Marsily G (1986) Quantitative Hydrogeology. Groundwater Hydrology for Engineers. Academic Press, London.

De' Gennaro M, Incoronato a., Mastrolorenzo G, et al (1999) Depositional mechanisms and alteration processes in different types of pyroclastic deposits from Campi Flegrei volcanic field (Southern Italy). J Volcanol Geotherm Res 91:303–320. doi: 10.1016/S0377-0273(99)00040-2

Di Vito M a., Isaia R, Orsi G, et al (1999) Volcanism and deformation since 12,000 years at the Campi Flegrei caldera (Italy). J Volcanol Geotherm Res 91:221–246. doi: 10.1016/S0377-0273(99)00037-2

Dvorak JJ, Gasparini P (1991) History of earthquakes and vertical ground movement in Campi Flegrei caldera, Southern Italy: comparison of precursory events to the A.D. 1538 eruption of Monte Nuovo and of activity since 1968. J Volcanol Geotherm Res 48:77–92. doi: 10.1016/0377-0273(91)90034-W

Fitzgerald RH, Tsunematsu K, Kennedy BM, et al (2014) The application of a calibrated 3D ballistic trajectory model to ballistic hazard assessments at Upper Te Maari, Tongariro. J Volcanol Geotherm Res. doi: 10.1016/j.jvolgeores.2014.04.006

Foote L, Scheu B, Kennedy B, et al (2011) Experemental calibration of hydrothermal explosions: A case study on Lake Okaro, New Zealand. Geosci Soc New Zeal 38–39.

Fowler a. C, Scheu B, Lee WT, McGuinness MJ (2010) A theoretical model of the explosive fragmentation of vesicular magma. Proc R Soc A Math Phys Eng Sci 466:731–752. doi: 10.1098/rspa.2009.0382

Fullard L a., Lynch T a. (2012a) On the Initiation of a Hydrothermal Eruption Using the Shock-Tube Model. Transp Porous Media 94:19–46. doi: 10.1007/s11242-012-9986-z

Fullard L a., Lynch T a. (2012b) The Effect of Cracks and a Steam Cap on Hydrothermal Eruptions. Transp Porous Media 92:15–28. doi: 10.1007/s11242-011-9888-5

Galland O, Gisler GR, Haug OT (2014) Morphology and dynamics of explosive vents through cohesive rock formations. J Geophys Res Solid Earth 119:4708–4728. doi: 10.1002/2014JB011050

Gilbert JS, Sparks RSJ (1998) The Physics of Explosive Volcanic Eruptions.

Goto A, Taniguchi H, Yoshida M, et al (2001) Effects of explosion energy and depth to the formation of blast wave and crater: Field explosion experiment for the understanding of volcanic explosion. Geophys Res Lett 28:4287–4290. doi: 10.1029/2001GL013213

Graettinger a. H, Valentine G a., Sonder I, et al (2014) Maar-diatreme geometry and deposits: Subsurface blast experiments with variable explosion depth. AGU Publ 740–764. doi: 10.1002/2013GC005198.

Gudmundsson MT, Einarsson B (2013) Hlaup og gufusprengingar í Kverkfjöllum í ágúst 2013. Jökull 149–151.

Gudmundsson MT, Högnadóttir Þ (2009) Jökullón í Vestari Kverkfjöllum , þróun og jökulhlaupahætta.

Haug ØT, Galland O, Gisler GR (2013) Experimental modelling of fragmentation applied to volcanic explosions. Earth Planet Sci Lett 384:188–197. doi: 10.1016/j.epsl.2013.10.004

Hobden BJ (1997) Modelling magmatic trends in time and space: Eruptive and magmatic history of Tongariro Volcanic Complex, New Zealand. University of Canterbury

Holsapple KA, Schmidt RM (1980) On the Scaling of Crater Dimensions 1. Explosive Processe. J Geophys Res 85:7247–7256.

Hurst T, Jolly AD, Sherburn S (2014) Precursory characteristics of the seismicity before the 6 August 2012 eruption of Tongariro volcano, North Island, New Zealand. J Volcanol Geotherm Res. doi: 10.1016/j.jvolgeores.2014.03.004

Isaia R, Marianelli P, Sbrana A (2009) Caldera unrest prior to intense volcanism in Campi Flegrei (Italy) at 4.0 ka B.P.: Implications for caldera dynamics and future eruptive scenarios. Geophys Res Lett 36:1–6. doi: 10.1029/2009GL040513

Isaia R, Vitale S, Di Giuseppe MG, et al (2015) Stratigraphy, structure, and volcano-tectonic evolution of Solfatara maar-diatreme (Campi Flegrei, Italy). Geol Soc Am Bull 1–20. doi: 10.1130/B31183.1

Jóhannsson M (1959) Haustferð á Vatnajökul. Jökull 9:41.42.

Jolly AD, Jousset P, Lyons JJ, et al (2014) Seismo-acoustic evidence for an avalanche driven phreatic eruption through a beheaded hydrothermal system: An example from the 2012 Tongariro eruption. J Volcanol Geotherm Res 286:317–330. doi: 10.1016/j.jvolgeores.2014.04.007

Kato A, Terakawa T, Yamanaka Y, et al (2015) Preparatory and precursory processes leading up to the 2014 phreatic eruption of Mount Ontake, Japan. Earth, Planets Sp 67:111. doi: 10.1186/s40623-015-0288-x

Kilgour G, V. Manville, Pasqua F Della, et al (2010) The 25 September 2007 eruption of Mount Ruapehu, New Zealand: Directed ballistics, surtseyan jets, and ice-slurry lahars. J Volcanol Geotherm Res 191:1–14. doi: 10.1016/j.jvolgeores.2009.10.015

Klikenberg LJ (1941) The permeability of porous media to liquid and gases. American Petroleum Institute

Koyaguchi T, Scheu B, Mitani NK, Melnik O (2008) A fragmentation criterion for highly viscous bubbly magmas estimated from shock tube experiments. J Volcanol Geotherm Res 178:58–71. doi: 10.1016/j.jvolgeores.2008.02.008

Kueppers U, Scheu B, Spieler O, Dingwell DB (2006) Fragmentation efficiency of explosive volcanic eruptions: A study of experimentally generated pyroclasts. J Volcanol Geotherm Res 153:125–135. doi: 10.1016/j.jvolgeores.2005.08.006

Lee CKB, Mazzola T a. (1989) Ejecta scaling laws for craters in dry alluvial sites. J Geophys Res 94:17595. doi: 10.1029/JB094iB12p17595

Lube G, Breard ECP, Cronin SJ, et al (2014) Dynamics of surges generated by hydrothermal blasts during the 6 August 2012 Te Maari eruption, Mt. Tongariro, New Zealand. J Volcanol Geotherm Res. doi: 10.1016/j.jvolgeores.2014.05.010

Manville V, Rouwet D, Morrissey MM (2015) Mechanisms of Crater Lake Breaching Eruptions. In: Volcanic Lakes. pp 73–91

Mastin LG (1995) Thermodynamics of gas and steam-blast eruptions. Bull Volcanol 57:85–98. doi: 10.1007/BF00301399

Mayer K, Scheu B, Gilg HA, et al (2015) Experimental constraints on phreatic eruption processes at Whakaari (White Island volcano). J Volcanol Geotherm Res 302:150–162. doi: 10.1016/j.jvolgeores.2015.06.014

McGuinness MJ, Scheu B, Fowler a. C (2012) Explosive fragmentation criteria and velocities for vesicular magma. J Volcanol Geotherm Res 237-238:81–96. doi: 10.1016/j.jvolgeores.2012.05.019

McKibbin R (1989) An attempt at modelling hydrothermal eruptions. In: New Zealand Geothermal, Workshop. p 9

McKibbin R (1996) Could non-condensible gases affect hydrothermal eruptions. In: Proc. 18th N. Z. Geotherm. Workshop. pp 323–330

McKibbin R, Smith T a., Fullard L (2009) Components and Phases: Modelling Progressive Hydrothermal Eruptions. ANZIAM J 50:365. doi: 10.1017/S144618110900011X

Montanaro C, Scheu B, Gudmundsson MT, et al (2016) Multidisciplinary constraints of hydrothermal explosions based on the 2013 Gengissig lake events, Kverkfjöll volcano, Iceland. Earth Planet Sci Lett 434:308–319. doi: 10.1016/j.epsl.2015.11.043

Moretti R, Arienzo I, Civetta L, et al (2013) Multiple magma degassing sources at an explosive volcano. Earth Planet Sci Lett 367:95–104. doi: 10.1016/j.epsl.2013.02.013

Morgan LA, Shanks WCP, Pierce KL (2009) Hydrothermal processes above the Yellowstone magma chamber: Large hydrothermal systems and large hydrothermal explosions.

Morra V, Calcaterra D, Cappelletti P, et al (2010) Urban geology: Relationships between geological setting and architectural heritage of the Neapolitan area. J Virtual Explor. doi: 10.3809/jvirtex.2010.00261

Mueller S, Scheu B, Kueppers U, et al (2011) The porosity of pyroclasts as an indicator of volcanic explosivity. J Volcanol Geotherm Res 203:168–174. doi: 10.1016/j.jvolgeores.2011.04.006

Mueller S, Scheu B, Spieler O, Dingwell DB (2008) Permeability control on magma fragmentation. Geology 36:399–402. doi: 10.1130/G24605A.1

Muffler LJP, White DE, Truesdell a. H (1971) Hydrothermal explosion craters in Yellowstone National Park. Bull Geol Soc Am 82:723–740. doi: 10.1130/0016-7606(1971)82[723:HECIYN]2.0.CO;2

Murphey BF, Vortman LJ (1961) High-explosive craters in desert alluvium, tuff, and basalt. J Geophys Res 66:3389. doi: 10.1029/JZ066i010p03389

Nelson CE, Giles DL (1985) Hydrothermal Eruption Mechanisms and Hot Springs Gold Deposits. Econ Geol 80:1633–1639.

Nordyke MD (1962) An analysis of cratering data from desert alluvium. J Geophys Res 67:1965–1974. doi: 10.1029/JZ067i005p01965

Norton DL, Dutrow B (2001) Complex behavior of magma - hydrothermal processes : Role of supercritical fluid. 65:4009–4017.

Ohba T, Taniguchi H, Oshima H, et al (2002) Effect of explosion energy and depth on the nature of explosion cloud a field experimental study. J Volcanol Geotherm Res 115:33–42. doi: 10.1016/S0377-0273(01)00307-9

Óladóttir BA, Larsen G, Sigmarsson O (2011) Holocene volcanic activity at Grímsvötn, Bárdarbunga and Kverkfjöll subglacial centres beneath Vatnajökull, Iceland. Bull Volcanol 73:1187–1208. doi: 10.1007/s00445-011-0461-4

Olafsson M, Torfason H, Gronvold K (2000) Surface exploration and monitoring of geothermal activity in the kverkfjöll geothermal area, central iceland. World Geotherm Congr 2000 1539–1545.

Orsi G, Civetta L, Del Gaudio C, et al (1999) Short-term ground deformations and seismicity in the resurgent Campi Flegrei caldera (Italy): An example of active block-resurgence in a densely populated area. J Volcanol Geotherm Res 91:415–451. doi: 10.1016/S0377-0273(99)00050-5

Orsi G, De Vita S, Di Vito M (1996) The restless, resurgent Campi Flegrei nested caldera (Italy): constraints on its evolution and configuration. J Volcanol Geotherm Res 74:179–214.

Orsi G, Di Vito MA, Isaia R (2004) Volcanic hazard assessment at the restless Campi Flegrei caldera. Bull Volcanol 66:514–530. doi: 10.1007/s00445-003-0336-4

Pardo N, Cronin SJ, Németh K, et al (2014) Perils in distinguishing phreatic fromphreatomagmatic ash; insights into the eruption mechanisms of the 6 August 2012 Mt. Tongariro eruption, New Zealand Natalia. J Volcanol Geotherm Res 286:397–414.

Petrosino S, Damiano N, Cusano P, et al (2012) Subsurface structure of the Solfatara volcano (Campi Flegrei caldera, Italy) as deduced from joint seismic-noise array, volcanological and morphostructural analysis. Geochemistry, Geophys Geosystems 13:1–25. doi: 10.1029/2011GC004030

Pétursson GG, Vogfjor KS (2009) Attenuation relations for near- and far- field peak ground motion ( PGV , PGA ) and new magnitude estimates for large earthquakes in SW-Iceland. Meteorological Report, no. VÍ 2009-012.

Piochi M, Kilburn CRJ, Di Vito M a., et al (2014) The volcanic and geothermally active Campi Flegrei caldera: An integrated multidisciplinary image of its buried structure. Int J Earth Sci 103:401–421. doi: 10.1007/s00531-013-0972-7

Piochi M, Mormone A, Balassone G, et al (2015) Native sulfur, sulfates and sulfides from the active Campi Flegrei volcano (southern Italy): Genetic environments and degassing dynamics revealed by mineralogy

and isotope geochemistry. J Volcanol Geotherm Res 304:180–193. doi: 10.1016/j.jvolgeores.2015.08.017

Planas-Cuchi E, Salla JM, Casal J (2004) Calculating overpressure from BLEVE explosions. J Loss Prev Process Ind 17:431–436. doi: 10.1016/j.jlp.2004.08.002

Procter JN, Cronin SJ, Zernack a. V., et al (2014) Debris flow evolution and the activation of an explosive hydrothermal system; Te Maari, Tongariro, New Zealand. J Volcanol Geotherm Res 286:303–316. doi: 10.1016/j.jvolgeores.2014.07.006

Prugh RW (1991) Quantitative Evaluation of "Bleve" Hazards. J Fire Prot Eng 3:9–24. doi: 10.1177/104239159100300102

Pyle DM (1989) The thickness, volume and grainsize of tephra fall deposits. Bull Volcanol 51:1–15. doi: 10.1007/BF01086757

Rager AH, Smith EI, Scheu B, Dingwell DB (2014) The effects of water vaporization on rock fragmentation during rapid decompression: Implications for the formation of fluidized ejecta on Mars. Earth Planet Sci Lett 385:68–78. doi: 10.1016/j.epsl.2013.10.029

Richard D, Scheu B, Mueller SP, et al (2013) Outgassing: Influence on speed of magma fragmentation. J Geophys Res Solid Earth 118:862–877. doi: 10.1002/jgrb.50080

Rosi M, Sbrana a., Principe C (1983) The phlegraean fields: Structural evolution, volcanic history and eruptive mechanisms. J Volcanol Geotherm Res 17:273–288. doi: 10.1016/0377-0273(83)90072-0

Sato H, Taniguchi H (1997) Relationship between crater size and ejecta volume of recent magmatic and phreato-magmatic eruptions: Implications for energy partitioning. Geophys Res Lett 24:205. doi: 10.1029/96GL04004

Scandone R, D'Amato J, Giacomelli L (2010) The relevance of the 1198 eruption of Solfatara in the Phlegraean Fields (Campi Flegrei) as revealed by medieval manuscripts and historical sources. J Volcanol Geotherm Res 189:202–206. doi: 10.1016/j.jvolgeores.2009.09.012

Scheu B, Spieler O, Dingwell DB (2006) Dynamics of explosive volcanism at Unzen volcano: An experimental contribution. Bull Volcanol 69:175–187. doi: 10.1007/s00445-006-0066-5

Seki K, Kanda W, Ogawa Y, et al (2015) Imaging the hydrothermal system beneath the Jigokudani valley , Tateyama volcano , Japan : implications for structures controlling repeated phreatic eruptions from an audio-frequency magnetotelluric survey. 0–8. doi: 10.1186/s40623-014-0169-8

Sherwood a. E (1967) Effect of air drag on particles ejected during explosive cratering. J Geophys Res 72:1783. doi: 10.1029/JZ072i006p01783

Smith VC, Isaia R, Pearce NJG (2011) Tephrostratigraphy and glass compositions of post-15kyr Campi Flegrei eruptions: Implications for eruption history and chronostratigraphic markers. Quat Sci Rev 30:3638–3660. doi: 10.1016/j.quascirev.2011.07.012

Spieler O, Alidibirov M, Dingwell DB (2003) Grain-size characteristics of experimental pyroclasts of 1980 Mount St. Helens cryptodome dacite xx. Bull Volcanol 65:90–104.

Spieler O, Dingwell DB, Alidibirov M (2004a) Magma fragmentation speed: An experimental determination. J Volcanol Geotherm Res 129:109–123. doi: 10.1016/S0377-0273(03)00235-X

Spieler O, Kennedy B, Kueppers U, et al (2004b) The fragmentation threshold of pyroclastic rocks. Earth Planet Sci Lett 226:139–148. doi: 10.1016/j.epsl.2004.07.016

Stearns HA, McDonald GA (1949) Geology and groundwater resources of the island of Hawaii. Hawaii Div Hydrogr Bull 9:1–363.

Steinberg GS (1976) On the determination of the energy and depth of volcanic explosions (paper dedicated to G. S. Gorshkov). Bull Volcanol 40:116–120. doi: 10.1007/BF02599856

Taddeucci J, Valentine G a., Sonder I, et al (2013) The effect of pre-existing craters on the initial development of explosive volcanic eruptions: An experimental investigation. Geophys Res Lett 40:507–510. doi: 10.1002/grl.50176

Thiéry R, Loock S, Mercury L (2010) Explosive properties of superheated aqueous solutions in volcanic and hydrothermal systems. In: Metastable Systems under Pressure. pp 293–310

Thiéry R, Mercury L (2008) Explosive properties of water in volcanic and hydrothermal systems. In: ICPWS XV. p 7

Thiéry R, Mercury L (2009) Explosive properties of water in volcanic and hydrothermal systems. J Geophys Res Solid Earth 114:1–19. doi: 10.1029/2008JB005742

Thorarinsson S (1953) The Grímsvötn Expedition June-July 1953 (Vatnajökulsferð 1953). Jökull 3:6–22.

Todesco M (2009) Signals from the Campi Flegrei hydrothermal system: Role of a “magmatic” source of fluids. J Geophys Res Solid Earth 114:1–14. doi: 10.1029/2008JB006134

Valentine G a., Graettinger AH, Macorps É, et al (2015) Experiments with vertically and laterally migrating subsurface explosions with applications to the geology of phreatomagmatic and hydrothermal explosion craters and diatremes. Bull Volcanol. doi: 10.1007/s00445-015-0901-7

Valentine G a., White JDL, Ross PS, et al (2012) Experimental craters formed by single and multiple buried explosions and implications for volcanic craters with emphasis on maars. Geophys Res Lett. doi: 10.1029/2012GL053716

Vilardo G, Isaia R, Ventura G, et al (2010) InSAR Permanent Scatterer analysis reveals fault re-activation during inflation and deflation episodes at Campi Flegrei caldera. Remote Sens Environ 114:2373–2383. doi: 10.1016/j.rse.2010.05.014

Vitale S, Isaia R (2014) Fractures and faults in volcanic rocks (Campi Flegrei, southern Italy): Insight into volcano-tectonic processes. Int J Earth Sci 103:801–819. doi: 10.1007/s00531-013-0979-0

Vogfjörd, K.C., Bean M, Roberts B, et al (2013) Extending Icelandic volcanological network operations into the ice caps. In: European Geophysical Union.

Walsh FD, Hochstein MP, Bromley CJ (1998) The Tongariro geothermal system (NZ): Review of geophysical data. Proc 20th NZ Geotherm Work 317–324.

White DE (1955) Violent Mud-Volcano Eruption of Lake City Hot Springs, Northeastern California. Geol Soc Am Bull 66:1109–1130. doi: 10.1130/0016-7606(1955)66[1109:VMEOLC]2.0.CO;2

Wilson L (1972) Explosive Volcanic Eruptions - I1: The Atmospheric Trajectories of Pyroclasts. Geophys J Int 30:381–392.

Wohletz KH (1986) Explosive magma water interactions Thermodynamics, explosion mechanisms, and field studies. Bull Volcanol 48:245–264.

Yamamoto T (2014) The pyroclastic density currents generated by the September 27, 2014 phreatic eruption of Ontake Volcano, Japan. Bull Geol Surv Japan Vol.65 (9/:117–127.

Yokoo A, Goto A, Taniguchi H, Oshima H (2002) Energy and depth of Usu 2000 phreatic explosions. Geophys Res Lett 29:48–51. doi: 10.1029/2002GL015928.

Zhang Y (2000) Energetics of gas-driven limnic and volcanic eruptions. J Volcanol Geotherm Res 97:215–231. doi: 10.1016/S0377-0273(99)00164-X.